

Louisiana State University

LSU Scholarly Repository

LSU Historical Dissertations and Theses

Graduate School

2000

Study of the Energy Spectrum of Solar Neutrinos Above 5.5 MeV.

Erik Karl Blaufuss

Louisiana State University and Agricultural & Mechanical College

Follow this and additional works at: https://repository.lsu.edu/gradschool_disstheses

Recommended Citation

Blaufuss, Erik Karl, "Study of the Energy Spectrum of Solar Neutrinos Above 5.5 MeV." (2000). *LSU Historical Dissertations and Theses*. 7339.

https://repository.lsu.edu/gradschool_disstheses/7339

This Dissertation is brought to you for free and open access by the Graduate School at LSU Scholarly Repository. It has been accepted for inclusion in LSU Historical Dissertations and Theses by an authorized administrator of LSU Scholarly Repository. For more information, please contact gradetd@lsu.edu.

INFORMATION TO USERS

This manuscript has been reproduced from the microfilm master. UMI films the text directly from the original or copy submitted. Thus, some thesis and dissertation copies are in typewriter face, while others may be from any type of computer printer.

The quality of this reproduction is dependent upon the quality of the copy submitted. Broken or indistinct print, colored or poor quality illustrations and photographs, print bleedthrough, substandard margins, and improper alignment can adversely affect reproduction.

In the unlikely event that the author did not send UMI a complete manuscript and there are missing pages, these will be noted. Also, if unauthorized copyright material had to be removed, a note will indicate the deletion.

Oversize materials (e.g., maps, drawings, charts) are reproduced by sectioning the original, beginning at the upper left-hand corner and continuing from left to right in equal sections with small overlaps.

Photographs included in the original manuscript have been reproduced xerographically in this copy. Higher quality 6" x 9" black and white photographic prints are available for any photographs or illustrations appearing in this copy for an additional charge. Contact UMI directly to order.

Bell & Howell Information and Learning
300 North Zeeb Road, Ann Arbor, MI 48106-1346 USA
800-521-0600

UMI[®]

STUDY OF THE ENERGY SPECTRUM OF
SOLAR NEUTRINOS ABOVE 5.5 MEV

A Dissertation

Submitted to the Graduate Faculty of the
Louisiana State University and
Agricultural and Mechanical College
in partial fulfillment of the
requirements for the degree of
Doctor of Philosophy

in

The Department of Physics and Astronomy

by

Erik Blaufuss

B.S., University of California, Irvine, 1995

December 2000

UMI Number: 9998658

UMI[®]

UMI Microform 9998658

Copyright 2001 by Bell & Howell Information and Learning Company.

All rights reserved. This microform edition is protected against
unauthorized copying under Title 17, United States Code.

Bell & Howell Information and Learning Company
300 North Zeeb Road
P.O. Box 1346
Ann Arbor, MI 48106-1346

ACKNOWLEDGMENTS

My time in graduate school has been an exciting part of my life, but I could not have done it without the support of many people. First, I must thank my advisor Robert Svoboda for the guidance, support, advice, knowledge, and opportunities he has given me. Bob never failed to find time in his busy schedule to spend some teaching me how to be a good physicist, most of which is not found in any book.

Getting this far in school has been a difficult and long road, and I would have never been able to do it without the support of my family. My lovely wife Karine gets all of the credit here. Her infinite patience and support when I was working in Japan for long periods of time, or stuck in my office for long nights has been greatly appreciated. Her love has pulled me through many of the most difficult times. I also wish to thank my mother and father for the opportunities they gave me in life, and my father for the interest in science that he gave me at a young age.

The construction, operation, and maintenance of an experiment the size of Super-Kamiokande would not have been possible without the help of the entire Super-Kamiokande collaboration. Under the guidance of Y. Totsuka, H. Sobel, and J. Stone, many great discoveries have been made. I would like to specially thank R. Sanford, M. Vagins, M. Nakahata, Y. Suzuki, W. Kropp, K. Martens, and all other members of the solar neutrino analysis group for their help, guidance and insights in our work together.

In the course of completing this work, I've spent a good part of my time living and working at the experimental site near Toyama, Japan. This was a unique experience that was made infinitely better by the presence of other students and post-docs on site with me. The presence of C. Mauger, M. Earl, B. Viren, T. Barszczak, J. Hill, A. Habig, M. Messier, K. Scholberg, G. Guillian, M. Smy, D. Takemori, and M. Malek made life there a little more interesting and for this, I am grateful. I am especially thankful to Y. Koshizawa who has been a great friend to all of us and helped us with so many of the little "inconveniences" of daily living in Japan.

While working here at LSU, many people have been helpful, supportive and deserving of thanks. In the physics department, the help of C. Champion, O. Dudley, R. Gould, A. Jackson, B. Rodriguez, Y. Thomas, and H. Valdes is greatly appreciated. The friendship P. Altice, E. Barnes, V. Gueorguiev, R. Madjoe, R. Meyhandan, and K. Misselt is also greatly appreciated, whether in class, on the raquetball court, or over a beer. The advice and support of M. Cherry, G. Clayton, C. Johnson, J. Matthews, and R. Kalia is also greatly appreciated.

I gratefully acknowledge the cooperation of the Kamioka Mining and Smelting Company for hosting the Super-Kamiokande detector. This work was partly supported by the Japanese Ministry of Education, Science and Culture, the U.S. Department of Energy and the U.S. National Science Foundation. I am also grateful for the support of the LSU Board of Regents in the form of a four year fellowship.

TABLE OF CONTENTS

ACKNOWLEDGMENTS	ii
LIST OF TABLES	vii
LIST OF FIGURES	ix
ABSTRACT	xv
CHAPTER 1. INTRODUCTION	1
1.1 Solar Models and Neutrino Fluxes	2
1.2 Previous Solar Neutrino Observations	9
1.2.1 Homestake Chlorine Detector	9
1.2.2 Kamiokande Water Cherenkov Detector	11
1.2.3 The Gallium Detectors	12
1.3 Solutions to the Solar Neutrino Problem	14
1.3.1 Modification of Solar Models	14
1.3.2 Neutrino Oscillations	16
CHAPTER 2. DETECTOR DESCRIPTION	26
2.1 Neutrino Detection Principles	26
2.2 Detector Overview	27
2.3 Water Purification System	31
2.4 Radon Free Air System	33
2.5 Photomultiplier Tubes	34
2.5.1 Inner Detector 50cm PMTs	34
2.5.2 Outer Detector 20cm PMTs	37
2.6 Data Acquisition Electronics	37
2.6.1 Inner Detector DAQ	38
2.6.2 Outer Detector DAQ	40
2.6.3 Triggers	42
2.7 SLE Online Reduction	42
2.7.1 System Overview	46
2.7.2 First Fit	47
2.7.3 Second Fit	50
CHAPTER 3. DETECTOR CALIBRATION	52
3.1 PMT Calibrations	52
3.2 Water Transparency Measurement	54
3.2.1 Laser Measurement	55
3.2.2 Decay Muon Measurement	55
3.3 LINAC Energy Scale Calibration	59
3.3.1 LINAC Hardware	61
3.3.2 Results from the LINAC Calibration	65
3.4 Nickel-Californium Calibration Source	69

3.5	The DTG Calibration	71
3.5.1	DTG Equipment	72
3.5.2	Results from the DTG Calibration	77
3.6	Trigger Efficiency	88
CHAPTER 4.	EVENT RECONSTRUCTION	90
4.1	Vertex Reconstruction	90
4.2	Direction Reconstruction	92
4.3	N_{eff} and Energy Reconstruction	94
4.4	Muon Reconstruction	97
4.4.1	Muboy-Stopped Muons for the ^{16}N Analysis	100
4.5	Other Reconstruction Tools	100
4.5.1	New Goodness Cut	101
4.5.2	Clusfit	102
CHAPTER 5.	NEUTRINO SIMULATIONS	107
5.1	Neutrino Interaction Simulation	107
5.1.1	Neutrino-Electron Cross Section	108
5.1.2	Creating ^8B Scattered Electrons	110
5.2	Detector Simulation	115
5.2.1	Simulation Input	118
5.2.2	Simulation Output	118
CHAPTER 6.	DATA REDUCTION	122
6.1	Reduction Steps	123
6.1.1	First Reduction	124
6.1.2	Spallation Cut	127
6.1.3	Second Reduction	129
6.2	Natural ^{16}N Analysis	135
6.2.1	Muon Capture on ^{16}O	135
CHAPTER 7.	SOLAR NEUTRINO SIGNAL EXTRACTION	140
7.1	Signal Extraction Method	140
7.1.1	First Order Extraction	141
7.1.2	Non-Flat Background Corrections	143
7.1.3	Corrections for Angular Cut Efficiency	148
7.1.4	Measurement of the Energy Spectrum	150
7.1.5	Measurement of Day/Night and Seasonal Fluxes	152
7.2	Error Analysis	159
7.2.1	Statistical Errors	159
7.2.2	Systematic Errors for Flux and Energy Spectrum	160
7.2.3	Day/Night and Seasonal Systematic Errors	173
CHAPTER 8.	RESULTS AND ANALYSIS	183
8.1	Measurement Results	183
8.1.1	Measured Solar Neutrino Flux	183
8.1.2	Recoil Electron Spectrum	184
8.1.3	Day/Night Flux Measurement	185

	8.1.4	Seasonal Flux Measurement	192
8.2		Discussion	192
	8.2.1	Day/Night Flux Variations	195
	8.2.2	Seasonal Flux Variations	196
	8.2.3	Recoil Energy Spectrum Distortions	197
8.3		Neutrino Oscillation Analysis	200
	8.3.1	Neutrino Flux Calculation	201
	8.3.2	Simulated Detector Response	205
	8.3.3	Excluded Regions	208
8.4		Summary	216
REFERENCES			217
VITA			220

LIST OF TABLES

1.1	Observed solar parameters	4
1.2	Total solar neutrino fluxes from the BP98 solar model	6
2.1	Summary of characteristics for the 50 cm PMTs used in the ID of SK	36
2.2	Summary of trigger thresholds for the self-generating trigger types	43
2.3	Summary of bits that compose the trigger word	43
3.1	Summary of LINAC measured detector resolutions	69
3.2	Position weights used in the position-weighted average for DTG data	83
3.3	Summary of systematic errors from the DTG calibration	88
6.1	Reduction summary	133
6.2	Partial capture rates for μ^- capture from the ^{16}O ground state to the beta decay capable states of ^{16}N	138
7.1	Summary of spectrum bins	155
7.2	Definition of day/night subsets	157
7.3	Definition of seasonal subsets	159
7.4	Absolute energy scale flux errors for the measurement of the spectrum in 5, 2.0MeV wide bins	162
7.5	Summary of systematic errors from solar neutrino flux mea- surement	172
7.6	Summary of non-energy dependent systematic errors from so- lar neutrino spectrum measurement	173
7.7	Summary of energy dependent systematic errors from solar neutrino spectrum measurement	174
7.8	Measured spallation sample energy distribution means for each subset of data used in the day/night and seasonal flux subsets.	178

7.9	Summary of day/night systematic errors	182
7.10	Summary of seasonal systematic errors	182
8.1	Measured fluxes in events/day for the data and the BP98 MC samples (^8B and ^7Be separately) for each energy bin	186
8.2	Day and night measured fluxes in events/day for the data and the BP98 MC samples	191
8.3	Seasonal subset measured fluxes in events/day for the data and the BP98 MC samples	194

LIST OF FIGURES

1.1	Schematic overview of pp chain fusion reactions that turn 4 protons into a helium nucleus (α)	5
1.2	The predicted solar neutrino spectra for each type of neutrino produced in the pp chain	7
1.3	Density profile of the Sun as a function of solar radius from the BP98 solar model	7
1.4	Neutrino production in the Sun as a function of solar radius for the 4 types of neutrinos produced by the pp chain	8
1.5	The constraints on the ${}^7\text{Be}$ and ${}^8\text{B}$ fluxes	15
1.6	Level crossing of matter neutrino states	22
1.7	95% allowed parameter space for neutrino oscillations in the Δm^2 region where MSW oscillations are expected to dominate.	24
1.8	95% allowed parameter space for neutrino oscillations in the Δm^2 region where vacuum oscillations are expected to dominate	25
2.1	An artist's representation of the SK detector	28
2.2	Schematic view of the PMT support frame used in SK	29
2.3	Local coordinate system used in the SK detector	30
2.4	Schematic view of the water purification system used in SK	33
2.5	Schematic view of the radon-free air system used in SK	34
2.6	An ADC histogram demonstrating the single photo-electron peak for the 50 cm PMTs used in the ID of SK	35
2.7	Schematic view of the 50 cm (20 inch) PMT used in SK	36
2.8	Quantum efficiency of the 50 cm PMTs used in the ID of SK as a function of photon wavelength	37
2.9	A schematic overview of the ID DAQ used at SK	41
2.10	The reconstructed vertex distributions for $R^2 (x^2 + y^2)$ and z for SLE triggered events	45

2.11	Distance and time differences between pairs of hit tubes for sample low energy events	48
3.1	Schematic diagram for the system used to make laser measurements of the wavelength dependence of the water transparency.	56
3.2	Water transparency measurement at 400 nm showing the normalized CCD signal as a function of diffuser ball depth in the detector	56
3.3	Schematic of the hit selection criteria used in the relative water transparency measurement from decay electrons	58
3.4	Distribution of $\log(q(r))$ versus r for a single days worth of decay electron events	59
3.5	Relative water transparency as measured by the decay of stopping muons as a function of time	60
3.6	Schematic view of the LINAC and associated beam line	62
3.7	Detailed schematic view of the LINAC system	62
3.8	Schematic view of the beam line end cap	63
3.9	Time-of-flight corrected hit time distributions for events that contain 1 electron, 2 electrons and 3 electrons	64
3.10	Reconstructed vertex position distribution for LINAC data . .	65
3.11	Reconstructed energy distributions for LINAC data	66
3.12	Measured energy deviation ($\frac{Data-MC}{Data}$) for each position and energy measured with the LINAC	68
3.13	Averaged energy deviation ($\frac{Data-MC}{Data}$) at each energy value . .	68
3.14	Averaged angular resolution difference as a function of energy.	70
3.15	Averaged energy resolution difference ($\frac{Data-MC}{Data}$) as a function of energy	70
3.16	Schematic of the DTG accelerator head and pulse-forming electronics unit encased in the stainless steel housing	74
3.17	Measured (n, p) cross section for ^{16}O as a function of energy .	76

3.18	Distribution of neutron travel distance between the target production point to the creation point of ^{16}N from the neutron simulation	77
3.19	Overview of the DTG data taking cycle	78
3.20	The reconstructed vertex distribution for a typical data taking run	79
3.21	Model details for the decay of ^{16}N	81
3.22	The reconstructed energy distribution for data and MC	82
3.23	The position-weighted average energy spectrum for data . . .	84
3.24	Position dependence of the energy scale as measured by DTG data	85
3.25	Angular dependence of the energy scale from DTG data	86
3.26	Distribution of time since generator fire for several DTG runs.	87
3.27	The measured trigger efficiency as a function of energy for the LE, SLE1, SLE2, SLE3 triggers	89
4.1	Timing distribution of hit PMTs in a typical solar neutrino candidate event	92
4.2	Grid point locations used by vertex fitter	93
4.3	(A) $f(\cos\theta_{dir})$ relative probability distribution used by the direction likelihood fitter	94
4.4	Average number of photoelectrons per hit tube in the 3×3 tube patch containing the hit tube	98
4.5	Reconstructed total electron energy as a function of the reconstructed N_{eff} value	98
4.6	Definition of grid points used by the new goodness cut	102
4.7	The goodfrac distribution from the new goodness cut for a sample of real data and MC ^8B data	103
4.8	Triangle relation between pairs of hit PMTs	104

4.9	The original and clusfit vertex distributions for events with energies between 5.5 and 6.5 MeV for a sample of real data and a sample from the ^8B MC data	105
5.1	Total cross section for neutrino-electron scattering as a function of neutrino energy	110
5.2	The best estimate ^8B neutrino energy spectral shape ($\lambda(E)$) .	111
5.3	The $\sigma(E_\nu) \cdot \lambda(E_\nu)$ distribution for the ^8B spectrum and (ν_e, e) cross section	112
5.4	The $\frac{d\sigma(E_\nu)}{dT}$ distribution for a 12 MeV neutrino	113
5.5	The kinetic energy distribution of ^8B neutrino scattered electrons	114
5.6	The tuned attenuation coefficient (attenuation length) $^{-1}$ as a function of wavelength	117
5.7	Schematic diagram of neutrino electron scattering	119
5.8	Event rate as a function of energy for the ^8B and hep MC samples	120
5.9	$\cos \theta_{sun}$ distribution for the ^8B MC sample	121
6.1	Distribution of the total charge for each event collected during a typical run at SK	125
6.2	Distribution of time differences between events	127
6.3	Spallation maximum likelihood distributions from muons with fit tracks	130
6.4	Spallation maximum likelihood distributions from muons without a fit track	130
6.5	Definition of the d_{eff} used in the gamma cut	132
6.6	Reconstructed vertex and direction distributions of the solar neutrino sample	132
6.7	The energy distribution of events in the solar neutrino data sample at 4 steps in the reduction	134
7.1	The distribution of $\cos \theta_{sun}$ for the final sample of solar neutrino candidates	141

7.2	Definition of regions and bins used in the $\cos\theta_{sun}$ plot for the signal extraction method	143
7.3	An example of the non-flat background determination	145
7.4	The $\cos\theta_{sun}$ distribution for the final sample of solar neutrino candidates with the final converged time-smeared non-flat background overlaid	147
7.5	The $\cos\theta_{sun}$ distribution along with the time-smeared non-flat background distribution for each energy bin for energies 5.5-6.0 to 9.5-10.0 MeV	153
7.6	The $\cos\theta_{sun}$ distribution along with the time-smeared non-flat background distribution for each energy bin for energies 10.0-10.5 to 14.0-20.0 MeV	154
7.7	Definition of D1-D5 and N1-N5 bins based on the location of the Sun relative to the SK detector	156
7.8	Definition of the seasonal bins based on the Earth-Sun distance	158
7.9	The deviation ((Corrected-Measured)/Measured) for the energy spectrum for the $+1\sigma$ and -1σ absolute energy scale shifts	162
7.10	Corrections applied to the measured MC spectrum	165
7.11	Energy distribution of events identified as likely spallation events	176
7.12	Distribution of measured means for a known input mean value.	179
8.1	The measured solar neutrino recoil electron spectrum	187
8.2	The ratio of the measured to the expected recoil electron spectrum	188
8.3	The ratio of the measured to the expected recoil electron spectrum as measured during day time and night time periods . .	189
8.4	Ratio of the measured to expected event rates for all, all day, all night, and the 5 bins of day and night	190
8.5	Ratio of measured to expected event rates for the seasonal flux subsets	193
8.6	The ratio of measured spectral shape for data (Data/SSM) and the spectral shape resulting from the best fit χ^2	200

8.7	An overview of the neutrino oscillation simulation	203
8.8	Comparison of the recoil electron spectrum from the full simulation of the BP98 flux and the fast electron simulation of the BP98 flux	207
8.9	99%, 95%, and 90% excluded regions from a hypothesis test performed on a χ^2 analysis of the measured day and night spectra in the MSW region	211
8.10	99%, 95%, and 90% excluded regions from a hypothesis test performed on a χ^2 analysis of the measured day and night spectra in the just-so region	212
8.11	MSW 99% and 95% excluded regions based on the distance from the χ^2 minimum	213
8.12	Just-So 99% and 95% excluded regions based on the distance from the χ^2 minimum	214

ABSTRACT

Data collected at the Super-Kamiokande detector have been used to make observations of the flux and spectrum of neutrinos that originate in the fusion reactions inside the center of the Sun. Previous observations of solar neutrinos have resulted in fluxes that are one third to one half the values predicted by solar models, a situation that has been labeled “the solar neutrino problem”. The phenomena of neutrino oscillations is investigated as a possible solution to this problem. The Super-Kamiokande detector, located in Gifu, Japan, is a ring-imaging Cherenkov detector that detects the scattered electrons from neutrino-electron elastic scattering in the water of the detector. Recoil electrons with energies greater than 5.5 MeV are used to measure the total flux and spectrum of solar neutrinos. The observed scattering rate is found to be $15.58 \pm 0.31(stat.)$ events/day in the 22.5 kton fiducial volume. This is a factor of $0.458 \pm 0.009(stat.)^{+0.011}_{-0.007}(sys.)$ of the expected rate predicted by the solar model of Bahcall and Pinsonneault, verifying the previous observations of the solar neutrino problem. Observations of the spectrum of recoil electrons and variations in the neutrino flux in different times of the day and different seasons of the year are also performed. A comparison of the neutrino fluxes measured during day and night time periods is consistent with no difference, $\frac{D-N}{0.5(D+N)} = -0.041 \pm 0.039(stat.) \pm 0.007(sys.)$. The observed spectrum and flux variations appear to be consistent with the results predicted in the absence of neutrino oscillations. These results are therefore

used to generate exclusion regions in the neutrino oscillation parameter space. This dissertation describes in detail the analysis which generated these results.

CHAPTER 1

INTRODUCTION

Energy is produced in the Sun through nuclear fusion. For a star such as the Sun, this involves turning 4 protons into a helium nucleus to tap the α particle binding energy by:

$$4p \rightarrow {}^4\text{He} + 2\nu_e + 2e^+ + 26.73 \text{ MeV}. \quad (1.1)$$

This 26.73 MeV of energy is primarily released as photons, which slowly diffuse their way to the surface of the Sun over the course of $\sim 10^5$ years. This energy is eventually emitted from the surface of the Sun with a black body spectrum ($T_{\text{surface}} = 5780 \text{ K}$). All information these photons might contain regarding the nuclear reactions that created them is lost in the repeated interactions these photons undergo as they percolate out of the Sun.

On the other hand, the neutrinos created in these nuclear reactions have very small reaction cross sections, even in the highest density regions of the Sun. They travel freely, essentially undergoing no interactions, from the regions of the Sun where they are created to detectors here on Earth, where a small fraction are detected. These neutrinos still contain information regarding the nuclear reactions going on inside the center of the Sun, providing a window to the internal mechanisms of the Sun. Therefore, the study of solar neutrinos can serve as an important test for theories of stellar evolution and structure.

The study of neutrinos is also interesting from a particle physics perspective. Neutrinos are weakly interacting particles, that are known to come

in three flavors, one for each of the massive leptons that they are associated with, the electron (ν_e), the muon (ν_μ), and the tau (ν_τ). Neutrinos are associated with the weak interaction, and are created in nuclear decays (for example, beta decay), nuclear reactors, high energy particle accelerators, and the fusion reactions that power the Sun.

It has long been assumed that neutrinos are massless, but recent evidence would indicate that at least some flavors of neutrinos are massive[1]. Neutrino mass naturally leads to interesting effects like oscillation of neutrino flavor, where neutrinos change from one flavor state to another as they propagate through space. The possibility of neutrino oscillations increases the difficulty associated with studying neutrinos for information on the solar interior. With neutrino oscillations, any effects seen in the observed neutrinos, such as a deficit of neutrinos or a distortion of the energy spectrum, could be a result of neutrino oscillations, interesting solar physics, or both.

The Super-Kamiokande (SK) detector is a water Cherenkov detector built to search for, among other things, the interaction of solar neutrinos. Neutrinos of sufficient energy ($\gtrsim 6$ MeV), are detected in real-time by the elastic scatter of electrons. These scattered electrons are used to measure the flux of solar neutrinos, any distortion in the spectrum of these neutrinos, and any short or long term time dependence of the flux.

1.1 Solar Models and Neutrino Fluxes

The production of energy inside the Sun is not as simple as Eqn 1.1 would indicate. In reality, complex models of the Sun are used to predict the rates and types of neutrinos produced. These solar models start with a

homogeneous composition of gases, with hydrogen burning taking place in the center of the star. The models then evolve the state of the star to the present age, using the following assumptions:

- The Sun is in hydrostatic equilibrium. This implies the Sun is relatively stable, and is no longer using gravitational collapse as a source of energy.
- The energy transport inside the Sun occurs only by photons and convection.
- The Sun's source of energy is nuclear fusion.
- Changes in elemental abundances are only caused by fusion reactions.

The inputs to this solar model include the nuclear cross sections for the reactions occurring in the center of the Sun, the radiative opacities for photons, the initial elemental abundances (fixed by observations of the current values at the solar surface), and the equation of state for the solar interior. The model is evolved in time to the current age of the Sun, and the observed solar parameters (Table 1.1) are compared to the modeled results. An accurate solar model will result in a radius, mass and luminosity that agree with these observed parameters.

These solar models also treat the fusion reaction which power the Sun. For a star such as the Sun, 99% of the energy produced by nuclear fusion proceeds through the proton-proton (pp) chain, shown in Figure 1.1. The reactions are labeled with relative probabilities, as well as the names of the neutrinos

Table 1.1: Observed solar parameters[2, 3, 4].

Parameter	Value
Radius	$(6.96 \pm 0.01) \times 10^8$ m
Mass	$(1.9889 \pm 0.0003) \times 10^{30}$ kg
Luminosity	$(3.84 \pm 0.02) \times 10^{33}$ ergs/sec
Age	$(4.57 \pm 0.02) \times 10^9$ yr

produced. Nearly 100% of the time, the pp chain starts with primary proton-proton reaction, two protons forming a deuterium, a positron and a neutrino. These highly abundant, yet low energy neutrinos are the “pp” neutrinos. The other source of deuterium is the rare three body reaction labeled “pep”, also producing a neutrino. The deuterium produced quickly picks up a proton to form ^3He . The chain branches from here into three competing reactions, each with a unique endpoint. 86% of the time, the ^3He will find another like particle and creates a helium nucleus (^4He , an α particle) and 2 protons (pp-I), which will re-enter the chain from the top. A very small fraction of the time (0.00002%) the ^3He will pick up another proton to form ^4He with the creation of a “hep” neutrino (HeP). The remaining 14% of the the ^3He will react with a previously formed ^4He nucleus to create ^7Be . The majority of ^7Be undergoes an electron capture to form ^7Li , and the so-called ^7Be neutrino (pp-II). The ^7Li quickly captures a proton and forms two α particles. A small fraction of ^7Be will capture a proton to form ^8B , which quickly beta decays to an excited state of ^8Be , releasing the energetic ^8B neutrino (pp-III). The $^8\text{Be}^*$ quickly decays to two α particles.

The remaining 1% of energy results from the CNO cycle, where carbon, nitrogen and oxygen present in the solar interior serve as catalysts for the

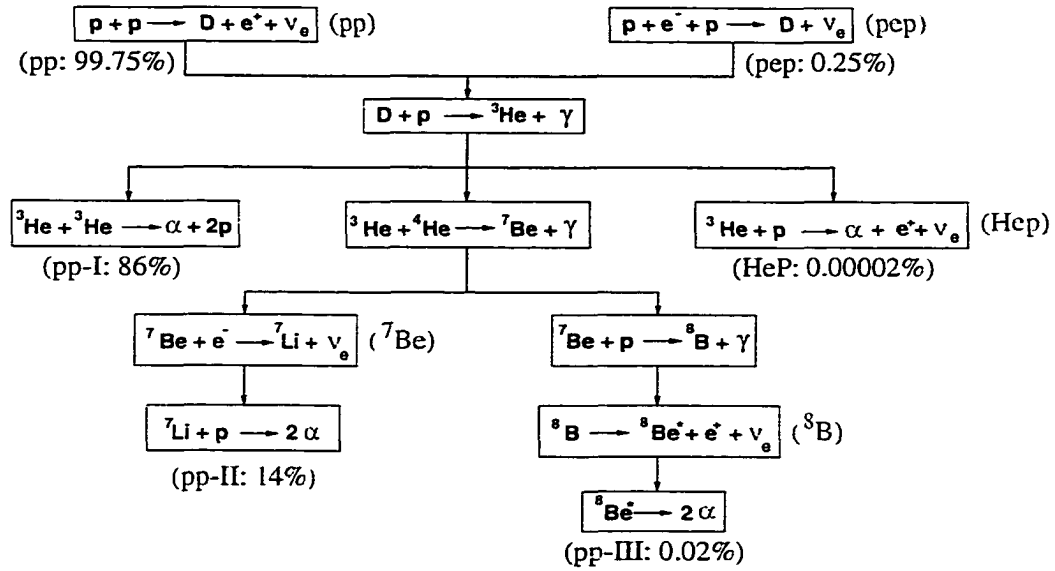


Figure 1.1: Schematic overview of pp chain fusion reactions that turn 4 protons into a helium nucleus (α).

conversion of 4 protons into a helium nucleus. As this represents such a small fraction of the energy produced by the Sun, it is not discussed further here, but is included in the solar models.

For this analysis, the solar model of Bahcall and Pinsonneault (BP98)[11] is used as the standard solar model (SSM). This model includes the effects of helium and heavier elements diffusion to the center of the Sun[3]. This model is used to obtain the overall flux of each type of neutrino in the pp chain (Table 1.2), as well as the spectral shape of each neutrino (Figure 1.2). This solar model also makes predictions for the density profile as a function of solar radius, and is shown in Figure 1.3. The distribution production points for each type of neutrino as a function of solar radius is shown in Figure 1.4. The neutrino fluxes and energy spectrum are used to make detailed simulations

Table 1.2: Total solar neutrino fluxes from the BP98 solar model[11]. Included are the 1σ uncertainties.

Reaction Source	Flux ($\times 10^{10} \text{cm}^{-2} \text{s}^{-1}$)
pp	5.96 ± 0.06
${}^7\text{Be}$	$(4.80 \pm 0.43) \times 10^{-1}$
pep	$(1.39 \pm 0.01) \times 10^{-2}$
${}^8\text{B}$	$(5.15^{+0.98}_{-0.72}) \times 10^{-4}$
hep	2.10×10^{-7}

of neutrino interactions in the detector, while the solar density profile and neutrino production distributions are used in models of neutrino propagation in the Sun.

Super-Kamiokande, as a water Cherenkov detector, is only sensitive to the ${}^8\text{B}$ and hep solar neutrinos, as shown in Figure 1.2. The pp, ${}^7\text{Be}$, and pep neutrinos all have energies below 2 MeV, and are undetectable in a water detector given their low energy, and the detector background rates at these energies. ${}^8\text{B}$ and hep neutrinos are the only types energetic enough to create recoil electrons above the high energy threshold of a water detector, and this analysis will concentrate exclusively on these two neutrino types. Unfortunately, the ${}^8\text{B}$ and hep are the rarest and most uncertain of the solar neutrinos produced.

The dominate uncertainty in the ${}^8\text{B}$ flux is in the cross section for the ${}^7\text{Be}(p,\gamma){}^8\text{B}$ reaction. At low energies, this cross section is parameterized by[6]:

$$\sigma(E) = S_{17}(E)E^{-1}e^{-2\pi\eta(E)} \quad (1.2)$$

where E is the center-of-mass kinetic energy, S_{17} is the S-factor for the

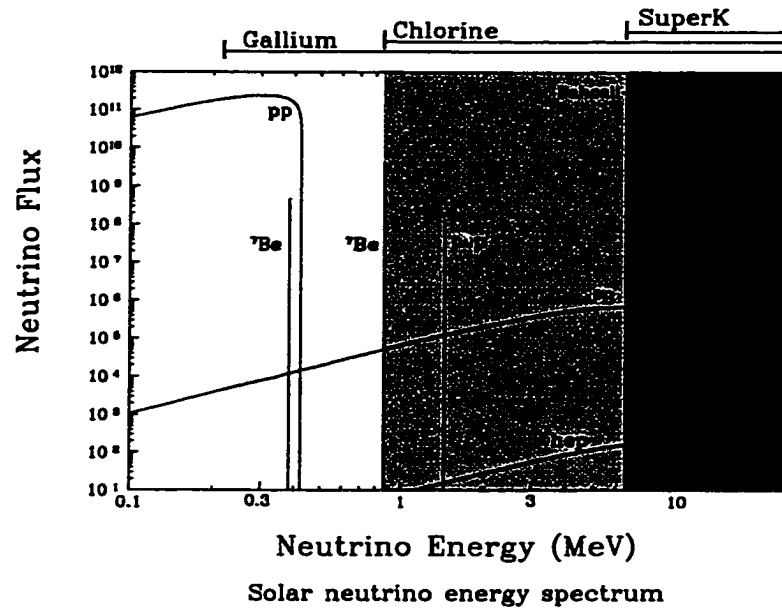


Figure 1.2: The predicted solar neutrino spectra for each type of neutrino produced in the pp chain. Arrows at the top indicate the range of sensitivity of each type of solar neutrino detector[5]. Note the logarithmic axes.

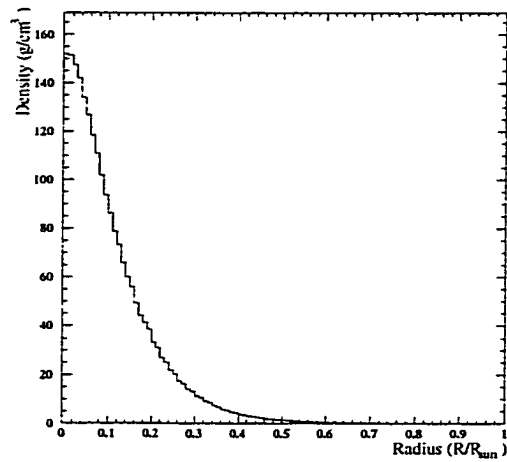


Figure 1.3: Density profile of the Sun as a function of solar radius from the BP98 solar model.

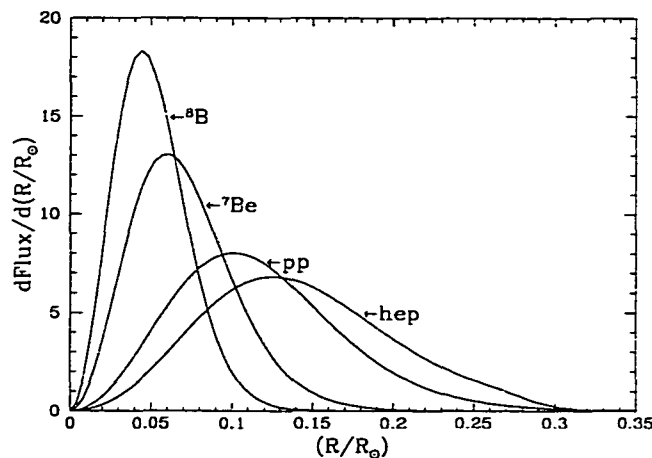


Figure 1.4: Neutrino production in the Sun as a function of solar radius for the 4 types of neutrinos produced by the pp chain[4].

${}^7\text{Be}(p,\gamma){}^8\text{B}$ reaction, $\eta = Z_1 Z_2 e^2 v^{-1}$. and v is the relative velocity of the reaction partners. The value of (S_{17}) is measured in the laboratory at energies much higher than those present in the center of the Sun. The solar value of S_{17} is obtained by extrapolating these measurements to lower energies, and this extrapolation results in the largest source of uncertainty for the ${}^8\text{B}$ neutrino flux. The BP98 solar model has adopted an S_{17} value of $19^{+8}_{-4} \text{eV} \cdot b$ (with 3σ errors)[7]. The uncertainty in this value represents a $\sim 10\%$ uncertainty in the ${}^8\text{B}$ flux. As this termination of the pp chain occurs only 0.02% of the time, this uncertainty does not impact the total solar luminosity. The only observable impact of changing this cross section is to change the expected ${}^8\text{B}$ neutrino flux.

Although the contributions from the hep neutrinos are expected to be much smaller than the ${}^8\text{B}$, the uncertainties in the hep flux are much larger. The source of this uncertainty is in the cross section for the ${}^3\text{He}(p, e^+ + \nu_e){}^4\text{He}$

reaction. No uncertainty in the hep flux of solar neutrinos is provided for the BP98 flux, but some estimates of this uncertainty indicate that a factor of ~ 20 in the hep flux would not be unreasonable[8]. Since the hep neutrinos extend to higher energies (~ 19 MeV), beyond the endpoint of the ^8B neutrinos (~ 15 MeV), they can complicate measurements of the neutrino spectrum at high energies. This complication is typically accommodated by treating the hep contribution as a free parameter.

1.2 Previous Solar Neutrino Observations

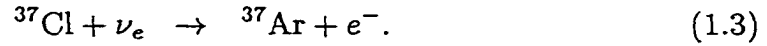
Prior to the observations at SK, three distinct types of solar neutrino experiments have been operated. Each type of detector is sensitive to a different range of neutrino energies, due to the different energy thresholds of the target material used. These different target materials include chlorine, water and gallium.

Since the cross section for neutrino interaction by the weak interaction is small, large number of targets are required to obtain just a few interactions. This requires that the detectors for solar neutrinos be large to allow detection of these elusive particles. These detectors are also built deep underground to shield them from the large cosmic ray flux at the Earth's surface which would otherwise obscure the detection of neutrinos.

1.2.1 Homestake Chlorine Detector

The first successful measurement of neutrinos from the Sun was performed by the Homestake chlorine detector[9]. The detector is located in the Homestake gold mine in Lead, South Dakota at a depth of 4200 mwe (meters water equivalent). The detector consists of a cylindrical tank containing 615 metric

tons (390,000 l) of liquid tetrachloroethylene (C_2Cl_4), a dry cleaning fluid. The detector is sensitive to solar neutrinos through the inverse beta decay reaction:



This reaction has an energy threshold of 0.814 MeV, making the detector sensitive to ^8B , ^7Be , pep, and hep neutrinos. The natural abundance of ^{37}Cl is 24.2%.

To make these measurements, data are collected in runs of 1-3 months in length. During these runs, ^{37}Ar is allowed to build up in the detector and at the end of the run, the ^{37}Ar produced is swept from the detector by bubbling He gas through the tank volume. The ^{37}Ar is chemically isolated in a cryogenically cooled absorber and is counted in a proportional counter, as it decays by emission of Auger electrons with a 35 day half life. During each run, a small amount of ^{36}Ar or ^{38}Ar carrier gas is added to the detector to measure the extraction efficiency, which is typically about 95%.

The Homestake detector has been measuring the flux of neutrinos since 1970. As of 1994[10], the detector had found a measured rate of ^{37}Ar production of

$$0.478 \pm 0.030(\text{stat.}) \pm 0.029(\text{sys.}) ^{37}\text{Ar atoms per day.}$$

Or in terms of solar neutrino units (SNU),

$$2.56 \pm 0.16(\text{stat.}) \pm 0.16(\text{sys.}) \text{ SNU,}$$

where:

$$1 \text{ SNU} = 1 \text{ capture per } 10^{36} \text{ targets per sec.}$$

The expected rate from the BP98 solar model is:

$$7.7^{+1.2}_{-1.0} \text{ SNU.}$$

The measured signal is only 33% of the expected rate. This deficit of the observed solar neutrino signal when compared with solar models is known as the “solar neutrino problem”.

1.2.2 Kamiokande Water Cherenkov Detector

The solar neutrino problem stood for almost 20 years before another experiment was able to make an independent measurement of neutrinos from the Sun. The Kamiokande detector[12] was upgraded in 1987, lowering the detectors threshold enough to allow the detection of solar neutrinos. Kamiokande was located in the Kamioka Mine, in Gifu, Japan at a depth of 2700 mwe. The detector contained a fiducial mass of 680 metric tons of water. This volume was monitored by 948 photo-multiplier tubes, each 50 cm in diameter, located on the walls of the cylindrical detector. Since Kamiokande was a water Cherenkov detector, it was only sensitive to the highest energy ^8B and rare hep neutrinos. Kamiokande detected neutrinos by the elastic scatter of electrons in the water,

$$\nu + e \rightarrow \nu' + e'. \quad (1.4)$$

The scattered electron is detected by the emission of Cherenkov light. As the direction of the electron is well correlated with the arrival direction of the incoming neutrino, measurement of the solar neutrino flux is performed by observing the excess of events over background coming from the direction of the Sun. In Kamiokande III, the minimum electron energy detectable was 7.5 MeV. Kamiokande II and Kamiokande III performed solar neutrino

observations covering all of solar cycle 22 (Jan 1987-Feb 1995) and found a measured ^8B neutrino flux[13] of

$$2.80 \pm 0.19(\text{stat.}) \pm 0.33(\text{sys.}) \times 10^6/\text{cm}^2/\text{sec}$$

The expected flux from the BP98 solar model is

$$5.15^{+0.98}_{-0.72} \times 10^6/\text{cm}^2/\text{sec}$$

The Kamiokande observations are significant for two reasons. First, they confirmed the existence of the solar neutrino problem, by measuring $\sim 50\%$ of the expected rate. Second, by the nature of the observation, they confirmed that these events are truly coming from the Sun. The design of Super-Kamiokande was based on knowledge gained during the operation of Kamiokande.

1.2.3 The Gallium Detectors

The chlorine and water detectors have been unable to measure the most predominate part of the solar neutrino flux, the low energy pp neutrinos. With an endpoint of 420 keV, the pp neutrinos require a different detection method. Two detectors using gallium, the SAGE and GALLEX experiments, began taking data in the early 1990's. Both experiments detect solar neutrinos by the inverse beta decay reaction:



This reaction has an energy threshold of 233 keV, making it sensitive to a large portion of the primary pp solar neutrino flux. The ^{71}Ge decays with a half life of 11.43 days.

The SAGE detector[14] located at the Baksan Neutrino Observatory in the Northern Caucasus Mountains of Russia began taking data in 1990. The

detector uses nearly 60 tons of metallic gallium. As in the chlorine detector, a quantity of ^{71}Ge is allowed to build up in the detector over an exposure period of ~ 1 month. The ^{71}Ge is chemically extracted and counted in a proportional counter to measure the flux of solar neutrinos. After nearly 8 years of operation, the observed ^{71}Ge production rate is found to be[14]:

$$67.2^{+7.2}_{-7.0}(\text{stat.})^{+3.5}_{-3.0}(\text{sys.}) \text{ SNU.}$$

The overall efficiency of the measurement has been checked with an intense neutrino source of ^{51}Cr . ^{51}Cr decays by electron capture to ^{51}V with neutrino energies of 751 keV (90.1%) and 426 keV (9.9%). The source activity used is 517 kCi. The ratio of the expected to the measured ^{71}Ge production rate is used as the measure of the overall efficiency and is found to be $0.95 \pm 0.11(\text{stat.})^{+0.05}_{-0.08}(\text{sys.})$ [15].

The GALLEX experiment[16] is located in the Gran Sasso underground laboratory outside Rome, Italy and began taking data in 1991. The detector uses 30.3 tons of gallium in a $\text{GaCl}_3\text{-HCl}$ solution. Exposures of ~ 20 days are taken before a chemical extraction is performed. The extracted ^{71}Ge is counted in a proportional counter. The measured ^{71}Ge production rate after 5 years of observation is found to be[17]:

$$77.5 \pm 6.2(\text{stat.})^{+4.3}_{-4.7}(\text{sys.}) \text{ SNU.}$$

The overall efficiency of the GALLEX detector was also checked using a ^{51}Cr neutrino source, and is found to be 1.04 ± 0.12 [18].

The expected rate of the BP98 solar model for the gallium detectors is:

$$129^{+8}_{-6} \text{ SNU,}$$

with 69.6 SNU from the primary pp neutrinos alone.

The gallium detectors measure $\sim 50\%$ of the expected rate and again confirm the existence of the solar neutrino problem, even when the flux of pp neutrinos is measured. The measured rates are only large enough to account for the expected pp neutrino contributions, the rate of which is strongly tied to the solar luminosity.

1.3 Solutions to the Solar Neutrino Problem

Four experiments have now verified the existence of a “solar neutrino problem”. Solutions to the solar neutrino problem typically fall into one of two types. The first type of solution involves changing the solar model, and adopting a model with different input parameters, or different dynamic prescriptions. The second type of solution involves changing the physics of neutrinos, not the solar models. In this case, the standard model is altered to allow non-conservation of neutrino flavor, and neutrino oscillations.

1.3.1 Modification of Solar Models

The modification of solar models, to create so-called non-standard solar models, has been suggested as a solution for the solar neutrino problem. This involves modification of model inputs, such as the S_{17} factor from above, or modification of model dynamics, such as reducing the central temperature of the Sun, to decrease the expected flux of neutrinos from the Sun.

Hata and Langacker[19, 20] have compared the resulting fluxes from a group of these non-standard solar models to the measured rates from the four experiments described above. Their analysis uses the dependence of the ^8B and ^7Be neutrino fluxes on the production of ^7Be and the resulting competition between proton capture and electron capture for ^7Be . The relative

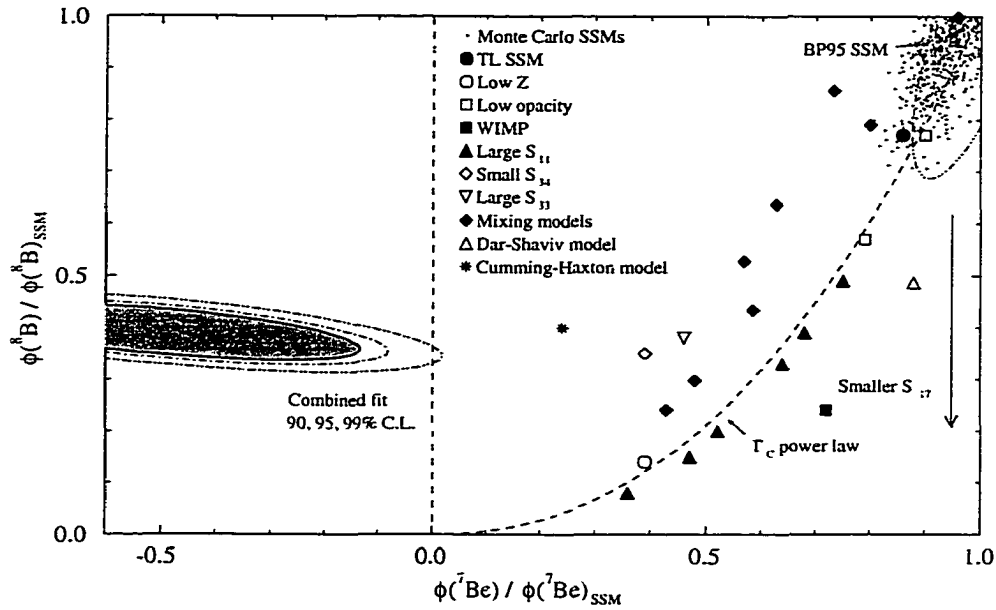


Figure 1.5: The constraints on the ^7Be and ^8B fluxes, measured relative to the standard solar model fluxes, from the combined results of the gallium, chlorine and water experiments at the 90% (shaded area), 95% (dot-dash line), and 99% (dot-dot-dash line)[20]. Also shown are the results from the standard and non-standard solar models. The power law dependence expected from changing the Sun's central temperature is also included (dashed line). References for the listed solar models can be obtained in Reference [20].

amounts of these two neutrino fluxes should be related, depending on the central temperature of the Sun. The hep neutrinos are not considered in this analysis, as their contribution to the measured fluxes is too small to be relevant. Figure 1.5 presents the results of their analysis, showing the ratio of modeled ^7Be flux to the SSM value versus the ratio of the modeled ^8B flux to the SSM value for many non-standard solar models. These solar models typically follow a predicted trend based on a central temperature power law, meaning if the central temperature is reduced, both the ^7Be and ^8B neutrino fluxes are decreased.

Also shown in Figure 1.5 are the results from combining the measured fluxes from the four experiments, shown as confidence level contours, predicting a ${}^8\text{B}$ flux of ~ 0.5 the SSM value, and a ${}^7\text{Be}$ neutrino flux of $-0.5 \times \text{SSM}$. This non-physical result of a negative ${}^7\text{Be}$ flux is driven by the contradictory results found in the experimental results. The Kamiokande experiment is sensitive only to the ${}^8\text{B}$ neutrinos, and is used to fix the ${}^8\text{B}$ flux. The gallium experiments are sensitive to pp, ${}^7\text{Be}$, and ${}^8\text{B}$ neutrinos, but only detect a signal large enough to cover the pp and ${}^8\text{B}$ contribution, which is required to maintain the observed solar luminosity. The chlorine detector, sensitive to both ${}^7\text{Be}$ and ${}^8\text{B}$ neutrinos, detects a flux lower than the value predicted by the Kamiokande ${}^8\text{B}$ -only result. When these results are combined, a negative, and non-physical, ${}^7\text{Be}$ flux is the only way to reconcile these results. This result is not significantly altered if any single detector type is dropped from this analysis[20].

This contradiction of the solar models with the experimental results seems to indicate that changing the solar model is not the correct answer to the solar neutrino problem.

1.3.2 Neutrino Oscillations

The second proposed resolution to the solar neutrino problem involves neutrino oscillations. If neutrinos have mass, then the non-conservation of neutrino flavor is allowed and a fraction of the electron-type neutrino flux created in the Sun could change to another type in transit to the Earth. When this mixture of neutrino types arrived at the detectors here on Earth, they would register a lower flux, as these detectors are less sensitive, or completely

insensitive, to other neutrino types. This changing of flavor is known as neutrino oscillations. Neutrino oscillations require a mass difference between the two mixed neutrino states, which implies that at least one of the neutrino masses be non-zero. This type of neutrino oscillation is known as vacuum oscillations.

The presence of matter can also influence the oscillation of neutrinos. As was first pointed out by L. Wolfenstein[21], and developed by S.P. Mikheyev and A.Y. Smirnov[22], electron type neutrinos experience an extra interaction potential in the presence of electrons that is not present for the muon and tau type neutrinos. Electron neutrinos can interact with electrons by the Neutral Current (NC) and Charged Current (CC) interactions, while the muon and tau neutrinos are limited to NC interactions. This so-called MSW effect can change the oscillation picture for electron type neutrinos in the presence of matter.

1.3.2.1 Vacuum Oscillations

If there are mass differences among the neutrino types, then the flavor eigenstate can be expanded in terms of mass eigenstates:

$$|\nu_e\rangle = a_1 |\nu_1\rangle + a_2 |\nu_2\rangle + a_3 |\nu_3\rangle \quad (1.6)$$

where:

$$\begin{aligned} |\nu_i\rangle &= (i = 1, 2, 3) \text{ neutrino mass eigenstates} \\ a_i &= \text{coupling constants, where } \sqrt{a_1^2 + a_2^2 + a_3^2} = 1 \end{aligned}$$

If, as a simplifying approximation, the oscillation between only two states is considered, then the relation between the flavor states (ν_e and ν_μ) and the mass states (ν_1 and ν_2) can be written as:

$$\begin{pmatrix} \nu_e \\ \nu_\mu \end{pmatrix} = \begin{pmatrix} \cos \theta & \sin \theta \\ -\sin \theta & \cos \theta \end{pmatrix} \begin{pmatrix} \nu_1 \\ \nu_2 \end{pmatrix} \equiv U \begin{pmatrix} \nu_1 \\ \nu_2 \end{pmatrix} \quad (1.7)$$

where θ is the mixing angle between the two states. If θ is zero, then no mixing takes place, where maximal mixing occurs for θ of $\frac{\pi}{4}$.

The time dependence of the mass eigenstates is obtained by solving the time-dependent Schrödinger equation:

$$i \frac{d}{dt} \begin{pmatrix} \nu_1 \\ \nu_2 \end{pmatrix} = H \begin{pmatrix} \nu_1 \\ \nu_2 \end{pmatrix} \quad (1.8)$$

where H is the vacuum Hamiltonian operator, which is diagonal for the mass eigenstates, with eigenvalues of:

$$\begin{aligned} E_i &= \sqrt{p^2 + m_i^2} \simeq p + \frac{m_i^2}{2p} \\ &\simeq E + \frac{m_i^2}{2E} \end{aligned} \quad (1.9)$$

It is assumed that the momentum (p) of the states are equal and that the masses of the eigenstates are much smaller than the neutrino energy ($m_i \ll E$). The time evolution of the mass eigenstates can then be written as:

$$\begin{pmatrix} \nu_1(t) \\ \nu_2(t) \end{pmatrix} = \begin{pmatrix} e^{-iE_1 t} & 0 \\ 0 & e^{-iE_2 t} \end{pmatrix} \begin{pmatrix} \nu_1(t=0) \\ \nu_2(t=0) \end{pmatrix} \quad (1.10)$$

In terms of the flavor eigenstates, this is rewritten:

$$\begin{pmatrix} \nu_e(t) \\ \nu_\mu(t) \end{pmatrix} = U \begin{pmatrix} e^{-iE_1 t} & 0 \\ 0 & e^{-iE_2 t} \end{pmatrix} U^{-1} \begin{pmatrix} \nu_e(t=0) \\ \nu_\mu(t=0) \end{pmatrix} \quad (1.11)$$

These time evolved flavor eigenstates are used to obtain the probability that a ν_e state at $t = 0$ is still a ν_e at some later time t :

$$P(\nu_e \rightarrow \nu_e; t) = 1 - \sin^2 2\theta \sin^2 \left[\frac{1}{2}(E_2 - E_1)t \right] \quad (1.12)$$

In terms of a distance traveled, L , and defining $\Delta m^2 = m_2^2 - m_1^2$:

$$\begin{aligned}
P(\nu_e \rightarrow \nu_e; L) &= 1 - \sin^2 2\theta \sin^2 \left[\frac{\Delta m^2 L}{4E} \right] \\
&= 1 - \sin^2 2\theta \sin^2 \left[1.27 \frac{\Delta m^2 [\text{eV}^2] L [\text{m}]}{E [\text{MeV}]} \right] \quad (1.13)
\end{aligned}$$

Similarly, the probability that a ν_e state at $t = 0$ is a ν_μ after traveling a distance L is given by:

$$P(\nu_e \rightarrow \nu_\mu; L) = \sin^2 2\theta \sin^2 \left[1.27 \frac{\Delta m^2 [\text{eV}^2] L [\text{m}]}{E [\text{MeV}]} \right] \quad (1.14)$$

The oscillation probabilities are functions of the distance traveled (L), the neutrino energy (E), the difference of the squared neutrino masses (Δm^2), and the mixing angle (θ). The values of L and E are set by the Earth-Sun distance and the incident neutrino spectrum, respectively. The values of Δm^2 and θ are so far undetermined. From this probability, an oscillation length (L_{osc}) can be derived:

$$L_{osc} = \frac{4\pi E}{\Delta m^2} = 2.48 \frac{E [\text{MeV}]}{\Delta m^2 [\text{eV}^2]} [m] \quad (1.15)$$

Vacuum oscillation will occur in vacuum, or in matter, but the behavior of electron type neutrinos will be changed in the presence of matter by the MSW effect.

1.3.2.2 MSW Matter Oscillations

When electron type neutrinos are propagating in matter, they experience an added potential, not experienced by the muon or tau type neutrinos. This added charged current interaction potential with electrons is expressed as:

$$V_e = \sqrt{2} G_F N_e \quad (1.16)$$

where G_F is the Fermi coupling constant, and N_e is the electron number density. When this potential is added to the time-dependent Schrödinger

equation for two component neutrino oscillation (Eqn 1.8), the following is obtained:

$$i \frac{d}{dt} \begin{pmatrix} \nu_e(t) \\ \nu_\mu(t) \end{pmatrix} = \left[U \begin{pmatrix} E_1 & 0 \\ 0 & E_2 \end{pmatrix} U^{-1} + \begin{pmatrix} V_e & 0 \\ 0 & 0 \end{pmatrix} \right] \begin{pmatrix} \nu_e(t) \\ \nu_\mu(t) \end{pmatrix}$$

After the removal of a common overall phase, this can be rewritten as:

$$i \frac{d}{dt} \begin{pmatrix} \nu_e(t) \\ \nu_\mu(t) \end{pmatrix} = \begin{pmatrix} -\frac{\Delta m^2}{4E} \cos 2\theta + \sqrt{2} G_F N_e & \frac{\Delta m^2}{4E} \sin 2\theta \\ \frac{\Delta m^2}{4E} \sin 2\theta & \frac{\Delta m^2}{4E} \cos 2\theta \end{pmatrix} \begin{pmatrix} \nu_e(t) \\ \nu_\mu(t) \end{pmatrix} \quad (1.17)$$

In the case of constant electron density, this equation can be diagonalized and recast in the form of Eqn 1.7:

$$\begin{pmatrix} \nu_e \\ \nu_\mu \end{pmatrix} = \begin{pmatrix} \cos \theta_m & \sin \theta_m \\ -\sin \theta_m & \cos \theta_m \end{pmatrix} \begin{pmatrix} \nu_1^m \\ \nu_2^m \end{pmatrix} \quad (1.18)$$

where ν_i^m are the mass eigenstates in matter, and θ_m is the matter mixing angle defined by:

$$\tan 2\theta_m = \frac{\sin 2\theta}{\cos 2\theta - \frac{L_{osc}}{L_0}} \quad (1.19)$$

where L_0 is the neutrino interaction length for CC interactions:

$$L_0 = \frac{2\pi}{V_e} = \frac{\sqrt{2}\pi}{G_F N_e} \quad (1.20)$$

The matter mixing angle will become resonant when $\cos 2\theta = \frac{L_{osc}}{L_0}$. This is the resonant condition, and electron type neutrinos will experience maximal mixing at the resonant electron density:

$$N_{e,res} = \frac{\Delta m^2 \cos 2\theta}{2\sqrt{2} G_F E} \quad (1.21)$$

This maximal mixing at the resonant density can occur even for small values of the vacuum mixing angle (θ). The probability that a ν_e is converted to a ν_μ after traveling in matter a distance L is now written:

$$P(\nu_e \rightarrow \nu_\mu; L) = \sin^2 2\theta_m \sin^2 \left(\frac{\pi L}{L_m} \right) \quad (1.22)$$

where:

$$L_m = L_{osc} \left(\frac{\sin 2\theta_m}{\sin 2\theta} \right) \quad (1.23)$$

These constant electron density solutions are also valid in matter of variable density if the changes in the electron density happens on a distance scale much larger than the matter oscillation length (L_m). For the general case of variable electron density, Eqn 1.17 is solved numerically.

Qualitatively, neutrino propagation in matter with a falling electron density (for example, as a neutrino travels from the center of the Sun to the vacuum of space) can be viewed as a level crossing problem. From Eqn 1.18, the relation between one matter mass state (ν_2^m) and the matter flavor states can be traced as a function of electron density:

$$\begin{aligned} |\nu_2^m\rangle &\sim |\nu_e\rangle && \text{Density} \gg \text{resonance} \\ |\nu_2^m\rangle &\sim (|\nu_e\rangle + |\nu_\mu\rangle)/\sqrt{2} && \text{Density} \sim \text{resonance} \\ |\nu_2^m\rangle &\sim \sin\theta|\nu_e\rangle + \cos\theta|\nu_\mu\rangle && \text{Density} \ll \text{resonance} \end{aligned}$$

This is illustrated in Figure 1.6, where a ν_e formed in the center (high electron density region) of the Sun will be primarily a ν_2^m state. As the neutrino propagates out of the Sun, through a region of falling electron density, this ν_2^m can adiabatically change to a near full ν_μ state. Even for small vacuum mixing angles, this can severely deplete the amount of electron neutrinos reaching the surface of the Sun. This same effect can regenerate the ν_e flux inside the Earth for some values of Δm^2 and $\sin^2 2\theta$.

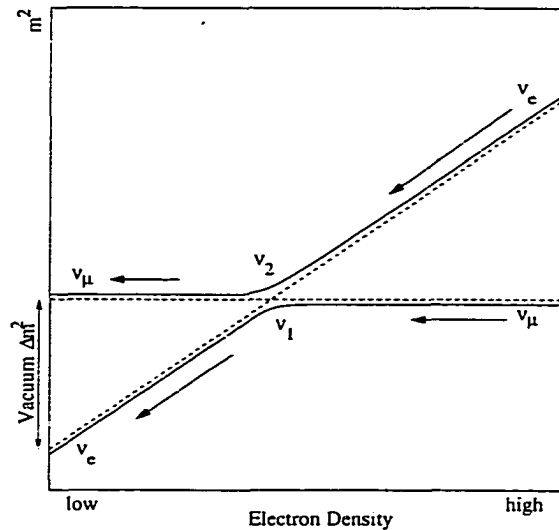


Figure 1.6: Level crossing of matter neutrino states. As the electron density falls, a ν_e can oscillate almost completely to ν_μ .

1.3.2.3 Oscillation Limits

The results from the experiments shown in Section 1.2 have been combined by Hata and Langacker[20] under the assumption of neutrino oscillations to generate allowed regions in the parameter space of $\sin^2 2\theta$ and Δm^2 . Each combination of $\sin^2 2\theta$ and Δm^2 was used in combination with the standard solar neutrino flux to generate the flux of neutrinos received at each detector. These fluxes are compared to the measured values, and this comparison is used to generate allowed regions in the neutrino oscillation parameter space. The overlap of the allowed regions from different experiments defines a set of allowed oscillation parameters that can explain the solar neutrino deficit. These allowed regions are shown in Figure 1.7 and Figure 1.8. Figure 1.7 presents the allowed regions for the Δm^2 region where MSW neutrino oscillations are expected to dominate. Two allowed regions

are found, one near maximal mixing, called the Large Mixing Angle (LMA) solution, and one near a mixing angle of $\sin^2 2\theta = 10^{-2}$, called the Small Mixing Angle (SMA) solution. Figure 1.8 presents the allowed region for the Δm^2 region where vacuum oscillations are expected to dominate.

Each of these three allowed regions predict their own unique characteristics on how the neutrino oscillations will be realized. The LMA solution predicts a regeneration of the electron neutrino flux as the “night-time” neutrinos pass through the Earth. This will appear as a higher measured flux at night, when compared to the day-time flux. The SMA solution predicts a strong energy dependence to neutrino oscillations. This will appear as a distortion of the measured neutrino spectrum when compared to the expected spectrum. The vacuum oscillation solution occurs in the Δm^2 region where the Earth-Sun distance is about equal to the oscillation length for solar neutrinos. Due to this chance coincidence of distances, these solutions are called “Just-So” oscillation. Just-So oscillations could manifest themselves as a seasonal variation of the measured flux as the Earth-Sun distance changes relative to the oscillation length. This variation would have to be in excess of the expected variation from the eccentricity of the Earth-Sun orbit.

The Super-Kamiokande detector has been designed and built to obtain a data sample with sufficient statistics to search for these effects. An observation of a measurable day/night flux difference, a distortion of the neutrino energy spectrum, or a seasonal dependence to the neutrino flux would provide solar model independent evidence of neutrino oscillations. In this analysis, the spectrum, day/night flux difference and seasonal flux variations are all measured and evaluated under a neutrino oscillation hypothesis.

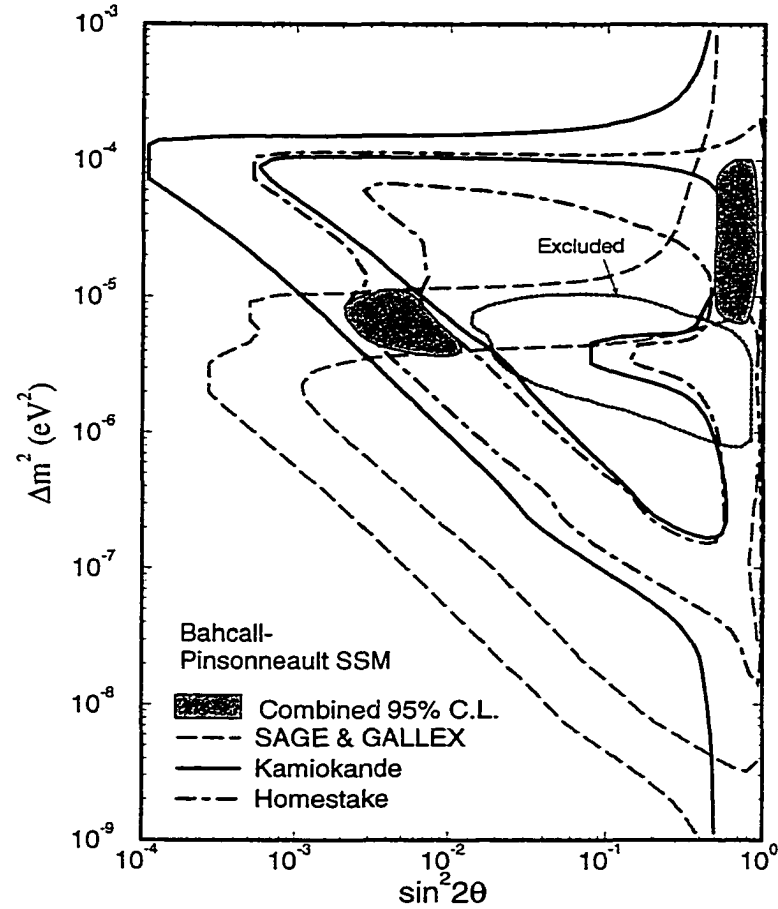


Figure 1.7: 95% allowed parameter space for neutrino oscillations in the Δm^2 region where MSW oscillations are expected to dominate. These allowed regions are made by combining the measured results from the gallium detectors (SAGE and GALLEX), chlorine (Homestake) and water (Kamiokande). The shown excluded region arises from a lack of an observed day/night flux difference in the Kamiokande data. Two combined allowed regions remain. Note that the x-axis is logarithmic.

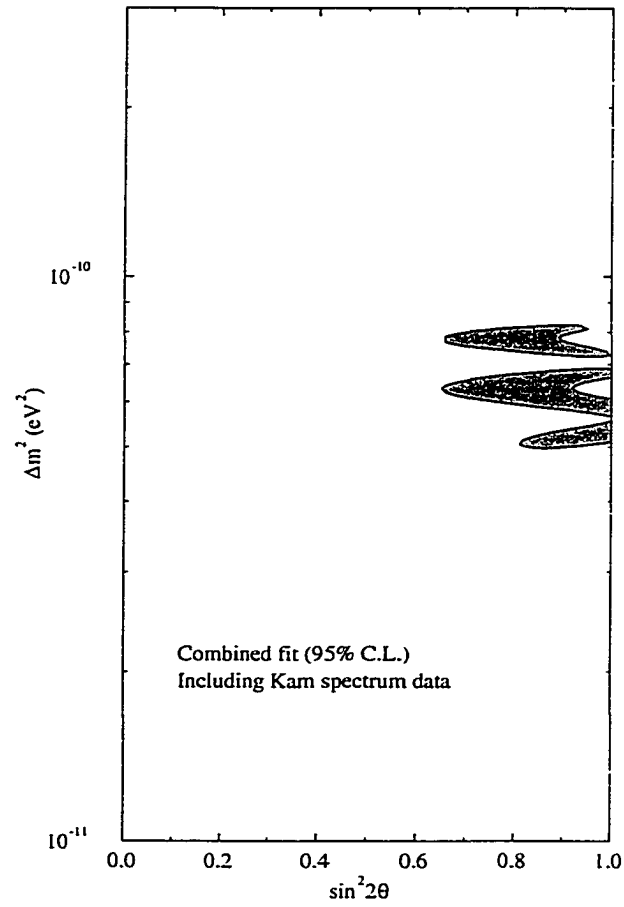


Figure 1.8: 95% allowed parameter space for neutrino oscillations in the Δm^2 region where vacuum oscillations are expected to dominate. Note that the x-axis is linear.

CHAPTER 2

DETECTOR DESCRIPTION

2.1 Neutrino Detection Principles

In order to study solar neutrinos, Super-Kamiokande (SK) operates as a ring-imaging Cherenkov detector. Solar neutrinos interact by neutrino-electron elastic scattering, and are capable of creating electrons with relativistic velocities. These electrons will radiate Cherenkov radiation if their velocity, u , exceeds the speed of light in water c/n , where c is the speed of light in vacuum, and n is the index of refraction of water. Cherenkov photons are emitted in a cone around the direction of travel of the electron with an opening angle, θ_c , of:

$$\cos\theta_c = \frac{1}{\beta n} \quad (2.1)$$

where β is the ratio of the electron's velocity to the speed of light in vacuum, $\beta = u/c$. The pure water inside SK has an index of refraction (n) of 1.33 in the wavelength region where the photomultiplier tubes are most sensitive (~ 400 nm). For a relativistic particle ($\beta \sim 1$), the Cherenkov radiation is emitted in water with an angle (θ_c) of about 42° . There is also a minimum energy required for creating Cherenkov radiation. For electrons in water, this minimum (threshold) energy is 0.768 MeV.

The number of Cherenkov photons emitted per unit of length traveled per unit frequency is a constant:

$$\frac{d^2 N_{\text{photon}}}{dL d\nu} = \frac{2\pi\alpha}{c} \sin^2\theta_c \quad (2.2)$$

This expression can be used to find the total number of Cherenkov photons emitted per unit of distance traveled, and for highly relativistic electrons in SK, about 390 Cherenkov photons are expected per cm traveled.

The distance traveled before a neutrino-scattered electron goes below the threshold energy is typically little more than a few centimeters at these energies. Therefore, the Cherenkov radiation can be treated as originating from single point in the detector and the cone-like nature of Cherenkov radiation will appear as a ring when projected onto the walls of the detector containing the light sensitive elements. For recoil electron events from solar neutrinos, multiple Coulomb scattering will change the direction of the electron as it travels in SK and blur the edges of the ring.

2.2 Detector Overview

Super-Kamiokande is located in the Kamioka Mine in Gifu Prefecture, Japan (137.32°E longitude, 36.43°N latitude). The detector is located underground (2700 m water equivalent) beneath the peak of Mt. Ikenoyama. The rock overburden of the detector reduces the cosmic ray flux entering the detector to an acceptable level (2.2 Hz). An artist's representation of the SK detector, showing a cut-away view of detector regions, is shown in Figure 2.1.

The SK detector is a cylindrical tank (41.4 m in height and 39.3 m in diameter) filled with 50,000 metric tons of ultra-pure water. The walls of the detector are constructed from welded stainless steel plates, backed with concrete. The detector is divided into inner and outer detector regions (ID and OD respectively) by a stainless steel frame structure that serves as an optical barrier and a mounting point for all photomultiplier tubes (PMTs),

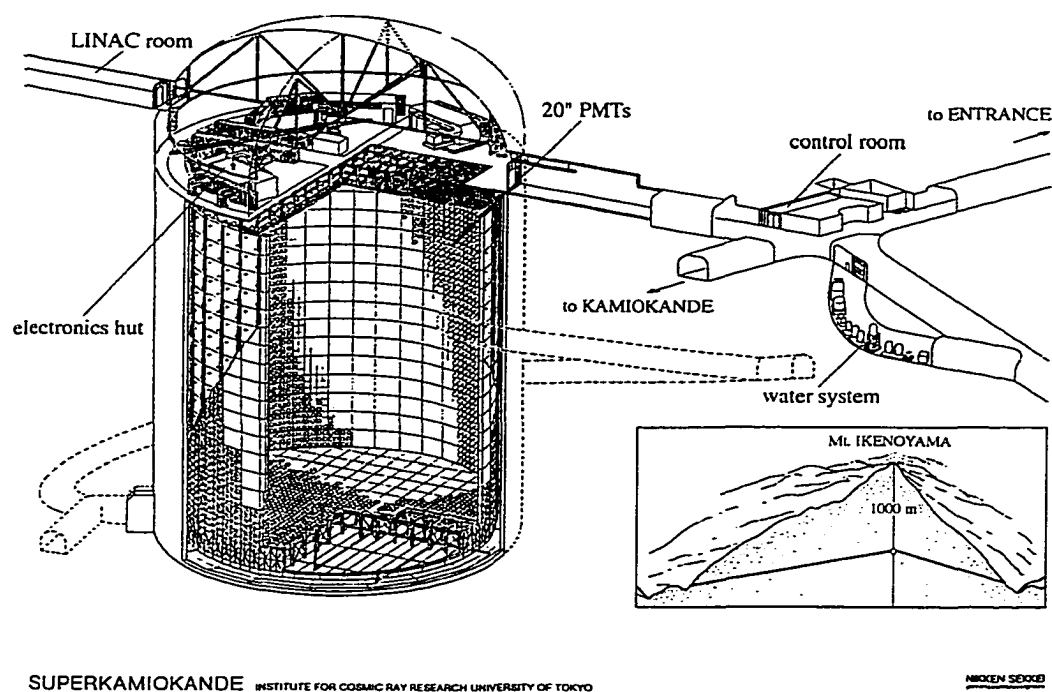
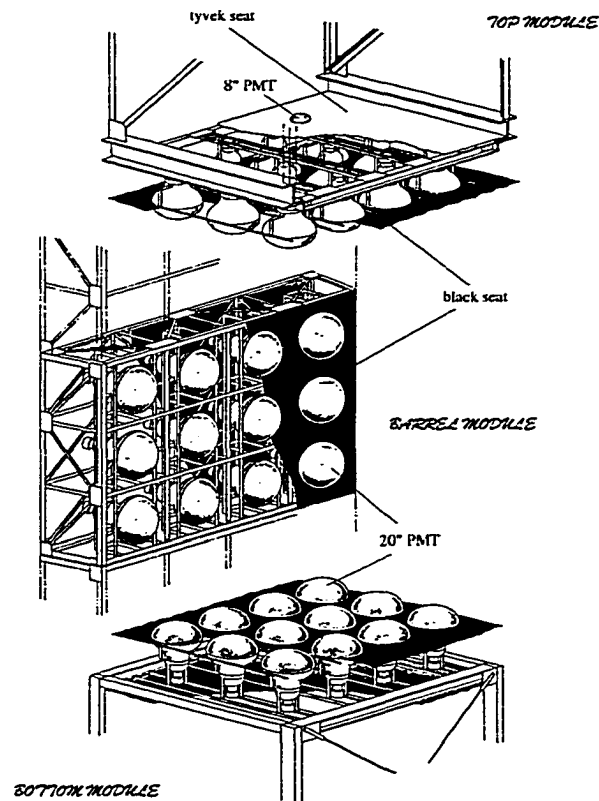


Figure 2.1: An artist's representation of the SK detector. The cut-away view shows the inner and outer detector regions, as well as the location of the detector within the mountain.



SUPERKAMIOKANDE INSTITUTE FOR COSMIC RAY RESEARCH UNIVERSITY OF TOKYO

MISSION SECRET

Figure 2.2: Schematic view of the PMT support frame used in SK.

which are the light sensing elements of the detector. The mounting structure for both inner and outer PMTs is illustrated in Figure 2.2. A local Cartesian coordinate system is established with the origin at the center of the tank, as illustrated in Figure 2.3.

The ID encloses 32,500 metric tons of water in a volume that is 36.1 m in height and 33.8 m in diameter. The fiducial volume, the portion of the detector volume where data used in the solar neutrino analysis are collected,

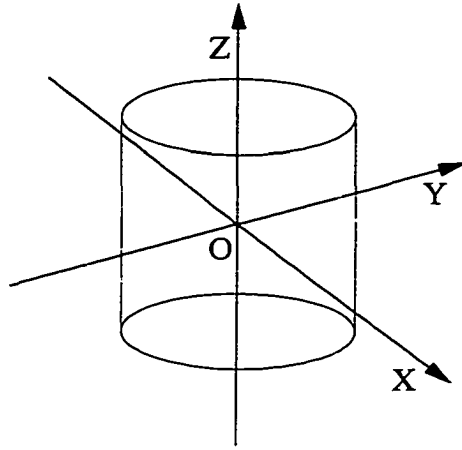


Figure 2.3: Local coordinate system used in the SK detector.

starts 2 m inward of the wall of the ID and contains 22,500 metric tons of water and is 32.1 m in height and 29.8 m in diameter. Cherenkov light in the ID is collected by 11,146 inward facing 50 cm PMTs distributed uniformly on the wall, providing 40% photocathode coverage. The remaining 60% of the inner detector walls are covered by black polyethylene sheets to reduce reflected light within the ID region, as well as to optically isolate the ID from the OD and the insensitive region enclosed by the PMT support structure.

The OD is the shell region that surrounds the ID and mounting structure. The thickness of the OD is 2.05 m on the top and bottom, and 2.2 m in the barrel region. 1,885 outward facing 20 cm PMTs collect Cherenkov light generated in the OD region. To enhance the light collection in the OD region, all surfaces are covered with white Tyvek sheeting, which has a reflectivity greater than 80% to Cherenkov photons. The OD region is used as a veto in the solar neutrino analysis to tag incoming particles and serves as a passive shield for gamma activity from the surrounding rock. The thickness

of the OD and the insensitive region enclosed by the PMT support structure represent ~ 7 radiation lengths and ~ 4.5 nuclear collision lengths.

All calibration systems and the huts containing the data acquisition electronics are located in the dome region above the detector tank. The tank is sealed to prevent mine air from contaminating the detector with radon gas. The dome area is supplied by a fresh air system that pumps air from outside the mine environment to reduce the radon levels in the area just above the tank. The walls in the dome area of the SK detector area are covered with a polyurethane material, called Mineguard, to help prevent radon gas from diffusing in from the rock. Double doors and a positive air pressure in the dome area help keep radon-rich mine air away from SK.

The detector is also surrounded by 26 Helmholtz coils to reduce the magnetic field in the detector. The large 50 cm PMTs are sensitive to external magnetic fields, and even in the Earth's field of 450 mG, the collection efficiency of the tubes is reduced. The coils reduce the magnetic field in the detector to the 50 mG, a level low enough to allow efficient operation of the large PMTs.

2.3 Water Purification System

Clean water is essential for making precise measurements of this kind. Any impurities in the water will limit the transmission of Cherenkov photons by absorption and scattering. Any dissolved radioactive impurities, like radon gas, will also add additional background for the solar neutrino analysis and make signal extraction more difficult. To reduce these effects, a water purification facility was built next to the SK detector to make and maintain the clean water of the detector.

The water purification facility at SK cleans water taken from the SK detector. The purification process consists of many stages to obtain output water of the highest purity. The steps involved are illustrated in Figure 2.4. When the detector is filled, the input water to the purification system is taken from a natural underground aquifer found in the mine. The water purification system consists of the following components:

- 1 μ m Filter: Removes large particulate contaminates, like dust.
- Heat Exchanger: Cools water heated by water pumps.
- Ion Exchanger: Removes metal ions.
- UV Sterilizer: Kills bacteria in the water.
- Vacuum De-gasifier: Removes dissolved gases, like oxygen and radon.
- Cartridge Polisher: A high performance ion exchanger, removes metal ions.
- Ultra Filter: Removes small particles down to 10 nm in size.
- Reverse Osmosis: A portion of the water is passed to the reverse osmosis filter, which removes additional dissolved gases, and is reintroduced to the water system.

The output of the water purification system is injected to the detector. The return water has an average resistivity of 18.20M Ω cm, very close to the chemical limit of 18.24M Ω cm. In normal operation, it takes about 1 month to process the entire detector volume with the water purification system.

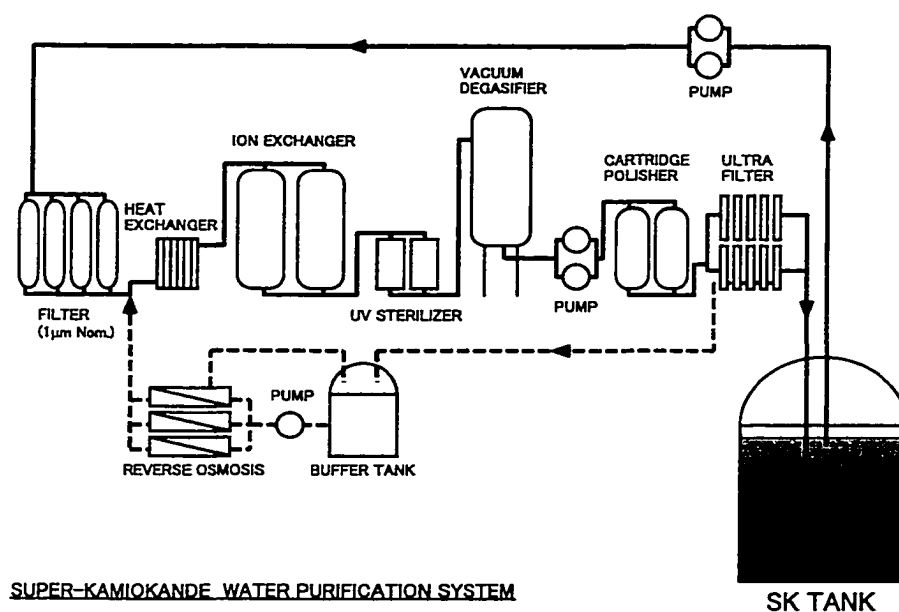


Figure 2.4: Schematic view of the water purification system used in SK.

2.4 Radon Free Air System

The small air space above the water inside the SK tank is filled with radon-free air from a special air system to prevent radon contamination of the detector water. A slight positive pressure is maintained in this space relative to the air pressure outside the tank to prevent radon gas from diffusing into the detector. A schematic diagram of the radon-free air system is shown in Figure 2.5. The radon-free air is generated by drying the input air, and passing this warm dry air over charcoal columns. The carbon in the charcoal absorbs the radon-gas, preventing it from entering the detector. The air is then filtered and injected into the region above the water in the SK tank. The injected air has a radon concentration of roughly 10 mBq/m^3 .

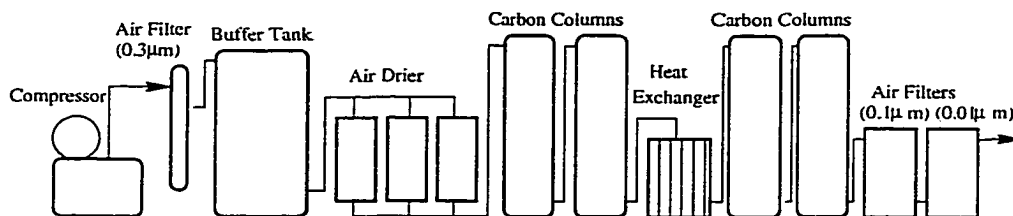


Figure 2.5: Schematic view of the radon-free air system used in SK.

2.5 Photomultiplier Tubes

Photomultiplier tubes (PMTs) are the light sensitive elements of the SK detector. These tubes convert single Cherenkov photons into electrical pulses, which are then measured by the data acquisition (DAQ) electronics. A tube is said to have a “hit” if a signal of sufficient size has been observed in the DAQ electronics.

PMTs are constructed of thin borosilicate glass, and the light sensitive surface is lined with a thin bi-alkali photocathode. The photocathode absorbs a photon and generates a single electron, known as a photo-electron. Photo-electrons are accelerated through an electric field generated by a $\sim 2\text{kV}$ potential that is applied to the tube toward a series of dynodes. These dynodes, when hit by a single electron, release $\sim 3\text{--}5$ more electrons, which are accelerated toward the next dynode. This is repeated until the single photo-electron has been multiplied to roughly 10^7 electrons. This multiplication factor is the gain of the PMT. These electrons are collected at the anode of the PMT and form the electrical signal read by the DAQ electronics.

2.5.1 Inner Detector 50cm PMTs

The PMTs used in the inner detector of SK are Hamamatsu model R1449 50.8 cm (20 inch) photomultiplier tubes. These tubes are an improved version

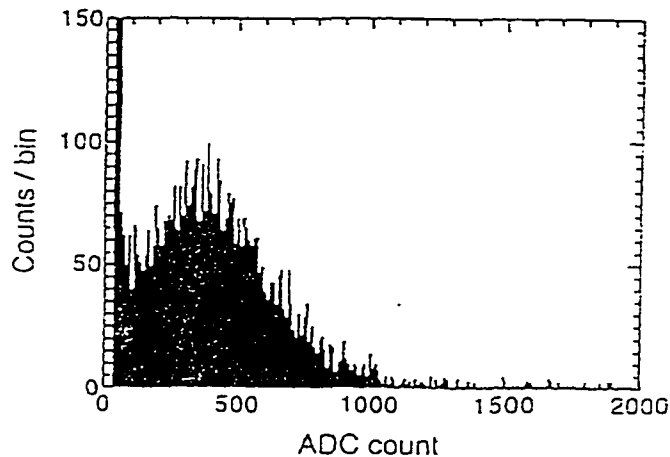


Figure 2.6: An ADC histogram demonstrating the single photo-electron peak for the 50 cm PMTs used in the ID of SK. The dark noise hits are located near the 0 ADC count bin[23].

of the 50 cm tube used in the original Kamiokande experiment[23]. As most PMT hits for the solar neutrino analysis only contain one photo-electron (p.e.), these tubes are designed to have a clear separation between dark noise hits and the 1 p.e. peak. The single p.e. peak for these tubes is shown in Figure 2.6, and shows clear separation between the dark noise and 1 p.e. peaks.

A schematic view of a typical PMT is shown in Figure 2.7 and their characteristics summarized in Table 2.1. 11,146 of these tubes provide 40% photocathode coverage in the ID region of SK. The quantum efficiency of these tubes, the probability that a photon will generate a photo-electron, is shown in Figure 2.8, and includes the transmission of the glass envelope as well as the photo-electron emission probability of the bialkali photocathode.

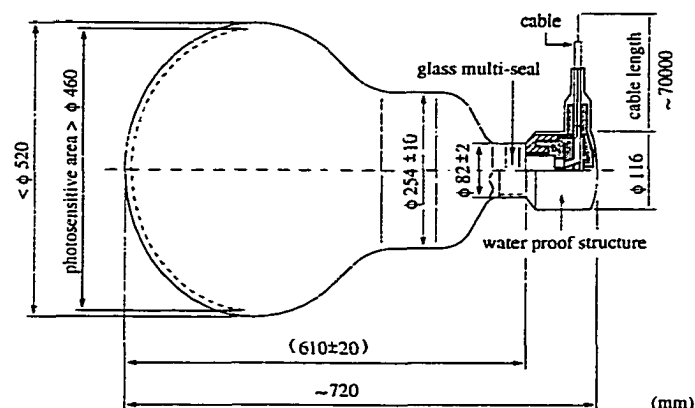


Figure 2.7: Schematic view of the 50 cm (20 inch) PMT used in SK.

Table 2.1: Summary of characteristics for the 50 cm PMTs used in the ID of SK.

Photocathode area	50.8 cm (20 inch) diameter
Shape	Hemispherical
Window material	4-5 mm thick Pyrex glass
Photocathode material	Bialkali (Sb-K-Cs)
Dynodes	11 stage, Venetian blind-type
Pressure tolerance	6 kg/cm ² water pressure
Quantum efficiency	22% at 390 nm (peak)
Gain	10 ⁷ at ~2kV.
Dark current	200 nA
Dark noise rate	3 kHz
Cathode non-uniformity	<10%
Anode non-uniformity	<40%
Transit time	100 ns
Transit time jitter	2.8 ns RMS at 1 p.e. levels

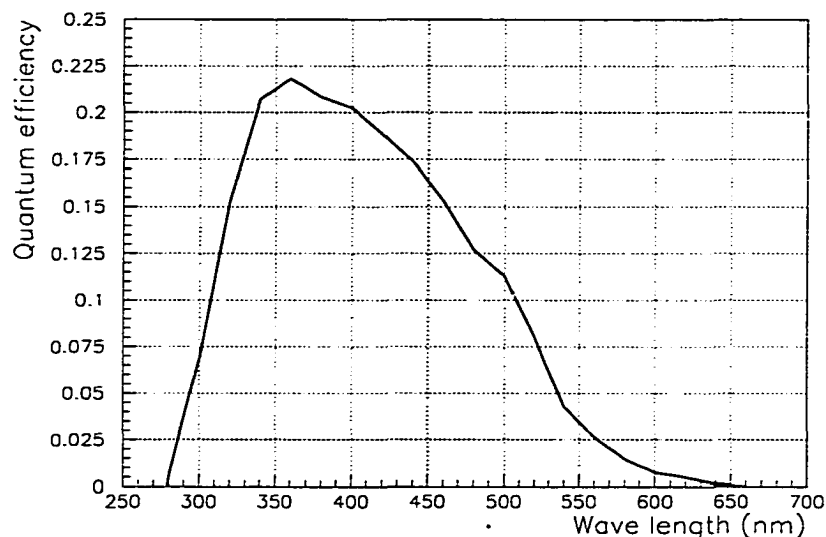


Figure 2.8: Quantum efficiency of the 50 cm PMTs used in the ID of SK as a function of photon wavelength.

2.5.2 Outer Detector 20cm PMTs

The OD region is equipped with 1,885 20 cm (8 inch) diameter Hamamatsu R-1408 PMTs. These tubes were first used in the IMB detector and were retrofitted for use in SK. The light collection of the OD PMTs is enhanced by the addition of acrylic plates ($\sim 0.4m^2$) containing a wavelength-shifting additive[24]. These plates absorb ultraviolet photons and re-emit photons in the blue wavelengths. These wave-shifter plates are attached to the face of the PMTs so that wave-shifted light is transmitted directly to the photocathode. These tubes typically operate at gains near 10^8 with $\sim 2kV$ supply voltages.

2.6 Data Acquisition Electronics

The data acquisition system is responsible for taking the stream of electrical pulses from every hit PMT and recording the time and size of each pulse.

The DAQ system must also be smart enough to recognize when collected hits are the result of dark noise, and to throw away these hits, or when hits are the result of real physics, generate a trigger and save the data as an event.

The ID and OD DAQ systems are different, due to different design goals and budget constraints. The ID DAQ's primary focus is dead-time-free data collection. Dead time results when the DAQ system is busy reading out data and is unable to take new data. To avoid dead time in the ID, only PMTs that contain hits are read out for each event, and each channel is equipped with dual signal processing hardware, so a single channel can collect information from new hits while being read out.

The primary job of the OD DAQ is to efficiently detect incoming particles, like cosmic ray muons. The OD DAQ is designed to have a long data acquisition period, collecting hits before and after the collected hits in the ID. The hits before and after the ID activity are used to determine if particles entered or left the ID region during an event. In the solar neutrino analysis, the OD is used as a veto, and any event with more than noise PMT hits in the OD is rejected as a possible solar neutrino candidate.

2.6.1 Inner Detector DAQ

The signal cables from the 11,146 PMTs are attached to a single channel of an Analog Timing Module (ATM). The ATM functions as a combination charge-to-digital and time-to-digital converter, recording the charge received and the relative time of each hit in one of two sub-channels. Each channel is self enabling, with a threshold of 0.32 p.e. required for a signal to be recorded. When a signal in a channel is recorded, an -11mV, 200 ns wide hitsum pulse

is generated. This hitsum pulse is added with all other channels, and if the sum exceeds a set threshold, a global detector trigger is issued. When this global trigger is issued, all channels that have been enabled with hits are digitized, and all ATM channels that have hits switch to their other sub-channel, to allow dead-time-free data taking. If no global trigger is issued in $1.1 \mu\text{sec}$, the hit information is lost, and the channel is reset. The digitized data is sent to a Super Memory Partner (SMP) module for transfer to the online computer system. The ATM channels have a 450 pC dynamic range, with a 0.2 pC resolution in charge, and a 1,300 ns dynamic range, with a 0.4 ns resolution in time.

ATM channels are placed in groups of 12 on a Tristan-KEK-Online (TKO) card, which is housed in a TKO crate. ATM cards are placed 20 cards to a TKO crate. Each TKO crate also contains a GO-NoGo (GONG) module to distribute global trigger information, and a Super Control Header (SCH) module to transfer the digitized data to the SMP module in the VME crate. There are 12 TKO crates in each of the 4 electronic huts located on the top of the SK detector. Each hut has two VME crates, each containing 6 SMP modules (one for each TKO crate of ATMs), as well as an interface card. The interface card is a Bit3 VME-SBUS adapter card and is used to send the data from the SMP modules to the memory of a Sun workstation. The data from the 8 Sun workstations are transferred via a dedicated FDDI optical network to the online host computer, where the data from each hut are assembled into an event. Environmental data, event time, trigger and OD PMT information are added from the appropriate electronic system located in a 5th, central electronics hut.

Each event in SK has two independent time records, used for relative and absolute event times. Relative timing between events is measured with a 48-bit counter driven by a 50 MHz clock. This clock can be used to measure the time between subsequent events to an accuracy of ~ 20 ns. The absolute time of each event is obtained from a GPS receiver which gives each event a UTC stamp. The accuracy of this absolute GPS time is about $10 \mu\text{sec}$.

An overview of the ID DAQ used at SK is presented in Figure 2.9. More details for the ID DAQ can be found in Reference [25].

2.6.2 Outer Detector DAQ

Since the PMTs in the OD do not have a separate signal cable, the signal from each tube is extracted from the high voltage supply line by a high voltage capacitor. This signal is sent to a custom-built Charge-to-Time Converter (QTC) module. If the height of a pulse from a PMT exceeds ~ 0.5 p.e., the QTC module generates an Emitter-Coupled-Logic (ECL) pulse. The start of the ECL pulse represents the hit time of each PMT signal, and the width of the ECL pulse is proportional to the log of the charge in a channel. The QTC module also generates a 200 ns wide pulse for triggering that is proportional in height to the number of hit channels in each QTC module. The ECL pulse is digitized by a Lecroy 1877 Fastbus Time-to-Digital Converter (TDC), which records the start and stop time of the ECL pulse. Outer detector data are recorded if a global trigger is received from the central hut. Hits from the OD tubes are saved in a window that starts $10 \mu\text{sec}$ before and ends $6 \mu\text{sec}$ after a global trigger. The TDC data are sent via a Fastbus Smart Crate Controller (FSCC) module to a Sun workstation, where it is sent to the online host for addition to the event data.

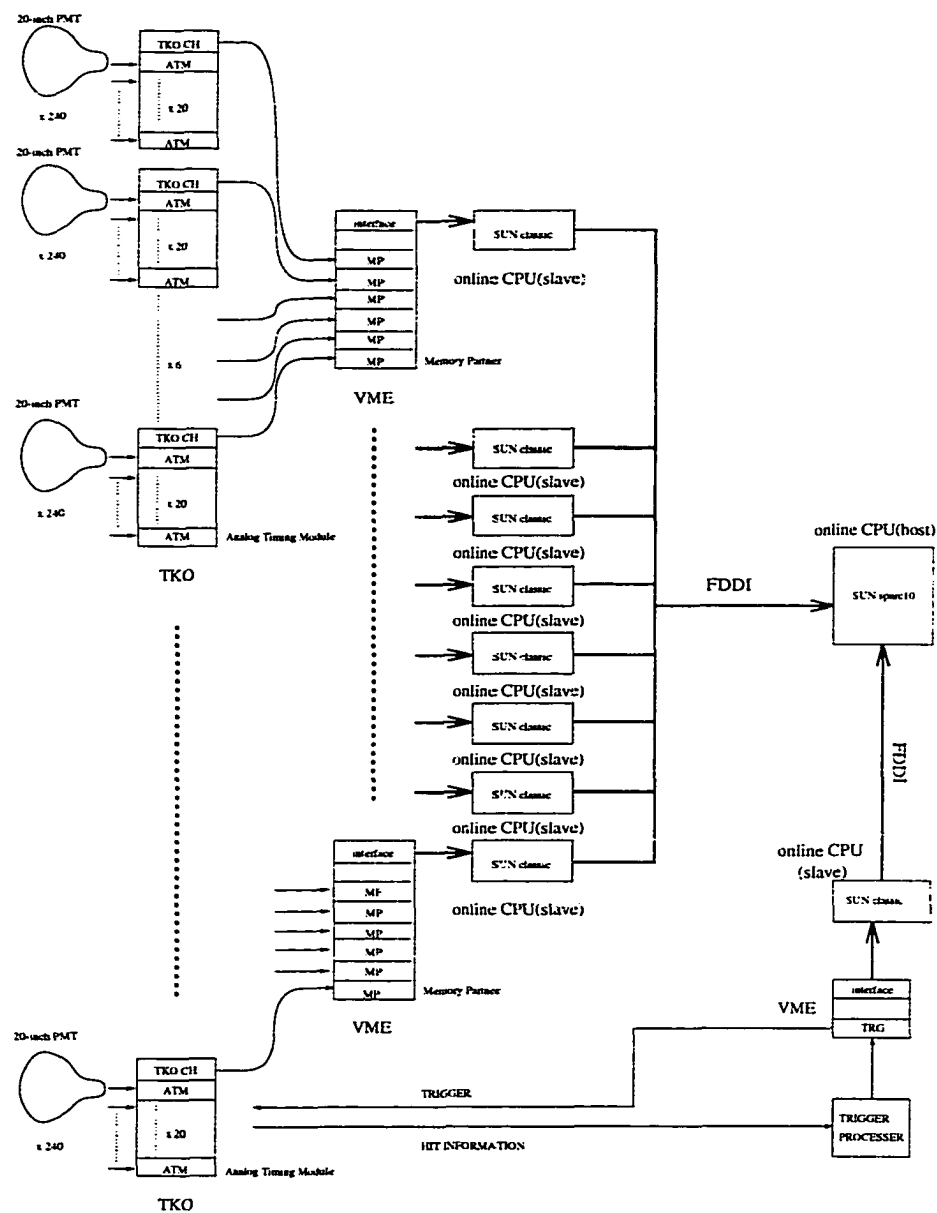


Figure 2.9: A schematic overview of the ID DAQ used at SK.

More details of the QTC modules can be found in Reference [26], and more details about the remainder of the OD DAQ can be found in Reference [25].

2.6.3 Triggers

There are numerous trigger types that are used at SK during data taking, including special triggers for calibration data. The most common triggers are the self-generating ones using the hitsum information from the ATM and QTC modules. The hitsum information from each ATM modules are summed, and then AC coupled, to reduce the effects of the constant dark noise contribution. This hitsum signal is distributed to many discriminators, which are set to different thresholds, and is used to generate the HE, LE and SLE triggers. The OD trigger is generated in a similar manner using the OD QTC hitsum signal. The OD DAQ is only read out for events that contain a HE and/or an OD trigger. The SLE trigger threshold has changed twice (being lowered each time) since its inception. The trigger threshold for each trigger type (HE, LE, SLE, OD) are summarized in Table 2.2, including the time dependence of the SLE trigger. Additional triggers are available for special run conditions (calibration) and for special event classes (unbiased clock trigger) and all trigger types are used to form a trigger word. The bits of the trigger word are summarized in Table 2.3. The LE and SLE triggers are the thresholds primarily used in the solar neutrino analysis.

2.7 SLE Online Reduction

After an event is built in the online host computer, the data are prepared to be sent out of the mine over a dedicated high speed network and written to tape. All events that have any trigger bit in addition to the SLE trigger are

Table 2.2: Summary of trigger thresholds for the self-generating trigger types.

Trigger Type	Run Period	Date of Run Period	Trigger Threshold
HE	1742-8058	May 1996-Oct 1999	340 mV (31 Hits)
LE	↓	↓	320 mV (29 Hits)
OD	↓	↓	19 OD Hits in 200 ns
Pre-SLE	1742-4141	May 1996-May 1997	None
SLE1	4142-7333	May 1997-May 1999	260 mV (24 hits)
SLE2	7334-7858	May 1999-Sep 1999	250 mV (23 hits)
SLE3	7859-8058	Sep 1999-Oct 1999	222 mV (20 hits)

Table 2.3: Summary of bits that compose the trigger word.

Bit	Trigger Type
1	Low Energy (LE)
2	High Energy (HE)
3	Super-Low Energy (SLE)
4	Outer Detector(OD)
5	Clock Trigger
6	Calibration Trigger
7	Global Trigger Veto Start
8	Global Trigger Veto Stop

automatically passed out of the mine. SLE only data, that is data which only has the SLE trigger bit set, is collected at very high trigger rates, ~ 100 Hz for SLE1, ~ 200 Hz for SLE2, and ~ 500 Hz for SLE3, and sending this much data out of the detector would overload the network and unnecessarily fill tapes and disks in the computer center. Therefore, events that only possess a SLE trigger are subjected to an additional reduction before the data are sent out of the mine.

The background for the solar neutrino analysis that is found in the SK detector has two noticeable features. First, this background grows exponentially in rate as the trigger threshold of the detector is lowered. The change from the SLE1 trigger to the SLE2 trigger was made by reducing the trigger condition by one hit tube, yet this change doubled the trigger rate. Second, this background seems highly correlated in position with the walls of the detector, with vertex distributions being highly peaked at the walls. Figure 2.10 shows the unfiltered reconstructed vertex distribution of these SLE events, with the strong correlation to the walls of the detector clearly visible.

Although the exact nature of this background is not completely understood, the vertex positions of these events are strongly correlated with the ID walls and PMTs and are clearly not solar neutrino events. In order to reduce the effects of this large background, an online event reconstruction and vertex cut has been implemented for these SLE triggered events. Only events which pass an online event reconstruction and fiducial volume cut are sent out of the detector and those that fail are dropped. This reduces the event rate sent out of the detector to ~ 10 Hz for the SLE only events.

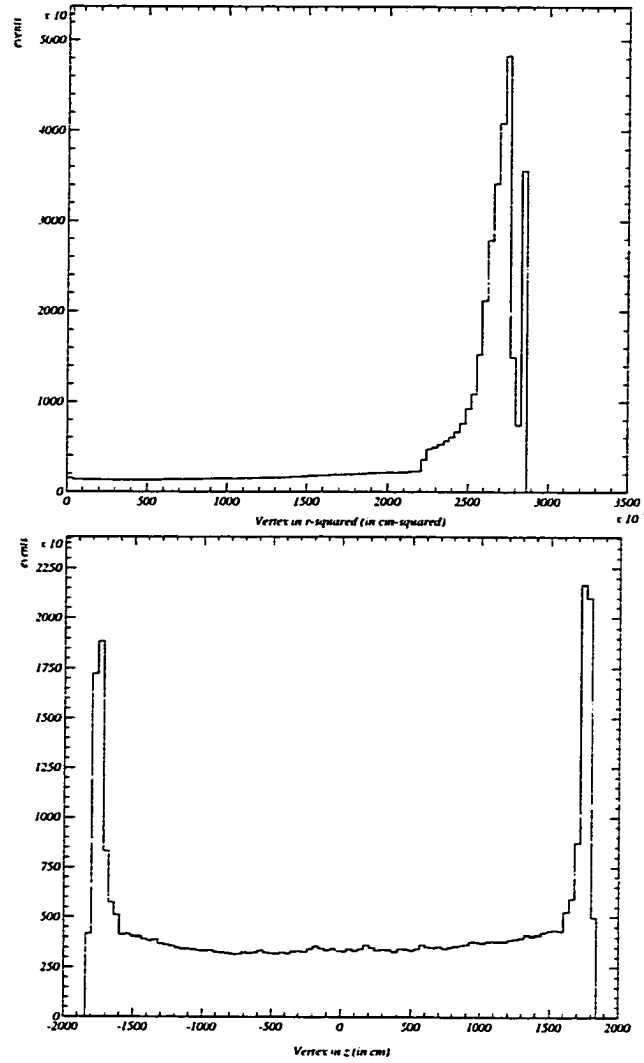


Figure 2.10: The reconstructed vertex distributions for R^2 ($x^2 + y^2$) and z for SLE triggered events. The large amount of background events can be seen near the ID walls.

2.7.1 System Overview

The SLE online event reconstruction runs on 6 dedicated Sun workstations located in the detector control room. For each SLE-only event, an event reconstruction is performed, and based on the reconstructed vertex, a fiducial volume cut is performed. Any events that reconstruct within 2 meters of the wall, or that fail to be reconstructed, are removed from the data stream. Only SLE events that have a reconstructed vertex in the 2m fiducial volume are sent out of the detector and recorded to tape. This results in a reduction of $\sim 20:1$, meaning 20 background events are found at the wall of the detector and are removed for every one event saved and passed out of the detector. Additionally, about 1 event per second is saved at random that was marked for removal in order to collect a background sample for further study and to monitor system performance.

The vertex reconstruction and fiducial volume cut are performed in two separate steps, with two different vertex fitters being used and a fiducial volume cut performed based on the vertex from each fitter. This two step process was chosen based on performance considerations. The first vertex fitter is a fast vertex fit, and successfully removes obvious noise events located at the wall of the detector. The second vertex fitter is a more precise fitter, but requires more CPU time for completion. To reduce the number of events passed to the slower, more precise fitter, a fiducial volume cut based on the fast fitter reconstructed vertex is first performed and only events that are found inside the 2m fiducial are passed to the precise fitter. A second 2m fiducial volume cut based on the precise fitter results is performed, and only

SLE events that are in the 2m fiducial volume based on reconstructed vertex positions from both fitters are saved and sent out of the detector.

2.7.2 First Fit

The first fit applied to the SLE events is performed with the Hayai vertex fitter, written by R. Svoboda. This fitter works in two steps. First, PMT hits in the ID are selected to be used in the fit. Second, the optimal vertex position is found by minimizing the timing residuals of all selected tubes.

2.7.2.1 Hit Selection

Each event is a mixture of hit PMTs resulting from Cherenkov photons from a physical event and hit PMTs from random dark noise. The hit selection is performed on each event as an attempt to separate the “real” hit PMTs in the ID from the hit PMTs due to random noise hits. This two step hit selection removes the $\sim 70\%$ of the raw number of tubes hits that are due to PMT noise.

The first step in the hit selection process is a causality cut on all hit PMTs. PMT hits that are associated with a single point in space-time (the true vertex) should be correlated with each other in space and time, while uncorrelated noise hits are going to populate space-time with a constant density. This concept is illustrated in Figure 2.11, showing the distance in space and time between pairs of hit PMT for a sample of events. The peak near (0,0) and the diagonal ridge are due to correlated events, while the constant background is from noise hits. The region within 10m in space and time¹ of (0,0) is selected to contain signal events. This method provides

¹time is measured in cm assuming a 29.94 cm/ns light speed in water

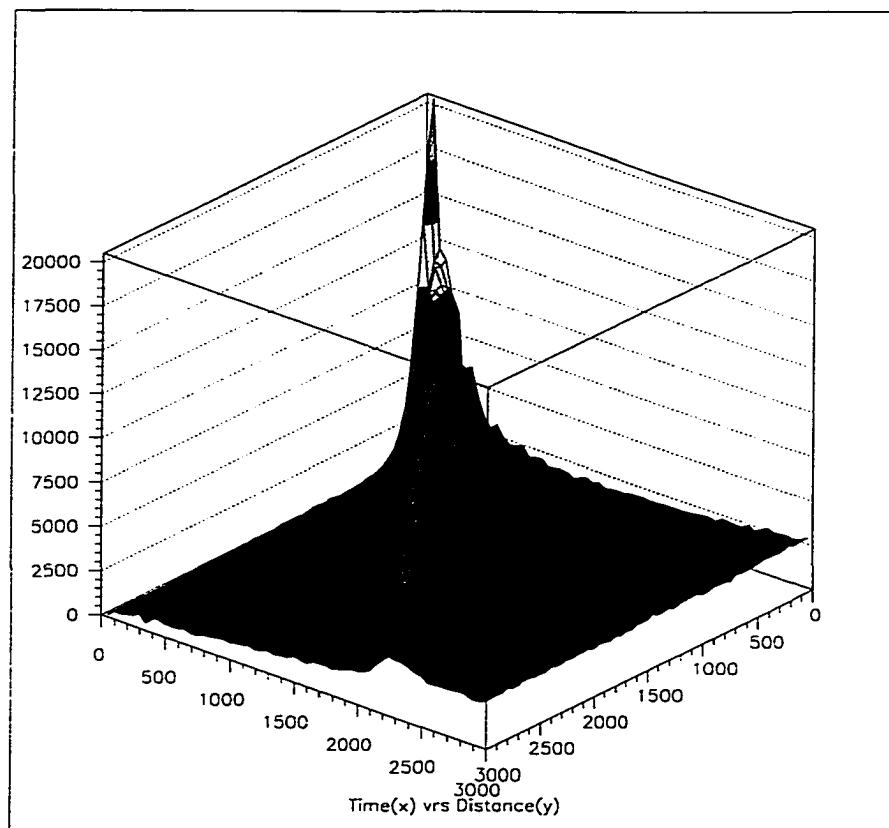


Figure 2.11: Distance and time differences between pairs of hit tubes for sample low energy events. Distance (left axis in cm) and time (right axis in cm, based on 29.94 cm/ns in water). The causality peak is located near (0,0). Hits are removed outside the 10 cm by 10 cm causal square.

a way to identify noise hits without having to find an event vertex. This reduction step removes $\sim 50\%$ of the tubes hits as noise hits.

The second step in the hit selection process is a time window cut. The time window cut identifies the time window that contains the maximum number of hit PMTs. This time window is taken to be 40 meters in size, roughly corresponding to the size of the detector. This fixed time window is moved throughout the distribution of hit times until the maximum number

of hit tubes is found. This time window cut removes an additional 40% of hit PMTs (after the causality cut is performed).

2.7.2.2 Vertex Determination

Once a set of PMT hits has been selected, the vertex that best represents this set of PMT hit times can be determined. An initial vertex position is taken to be the 1st moment of the selected hits. This initial guess is then moved 2m toward the center of the detector, to ensure that each event has a chance of being reconstructed inside the fiducial volume.

The vertex is determined by calculating the goodness of fit (gof) for each vertex location considered. For each hit PMT selected, the time-of-flight (tof) corrected hit time, which is a correction to the PMT hit time for the time required for a photon to travel from the vertex location to the hit tube, is determined. Then, the residual time (t_{res}) of each PMT is calculated by subtracting the mean hit time of all PMTs from the tof corrected hit times. The gof is defined as:

$$\text{gof} = \frac{1}{N_{sel}} \sum_{Hits}^{Selected} \exp\left(\frac{-t_{res}^2}{2\sigma^2}\right) \quad (2.3)$$

where N_{sel} is the number of selected hits used, and σ is an expected characteristic width of hits in time from PMT timing resolution. This gof value is calculated for the initial guess vertex, as well as for an array of 18 vertices uniformly distributed on a sphere surrounding the guess vertex, and the point with the best gof is chosen as the next guess vertex. This process is repeated until a single vertex location is repeatedly returned, then the size of the sphere of test vertex positions is reduced. The process is repeated, with successively smaller test vertex spheres until a best fit vertex position

is found. A 2m fiducial volume cut is performed based on this reconstructed vertex. Those events that are inside the fiducial volume are sent to the second fit, those outside are dropped.

2.7.3 Second Fit

The second fitter used in the SLE online reduction is the same fitter used in the analysis of solar neutrino events, known as *Kaifit*². The version used in the SLE online reduction has been slightly modified, using look-up tables to calculate exponentials in order to obtain greater computational speeds.

This vertex reconstruction proceeds in a similar fashion to the first vertex reconstruction. First, hit PMT selection is performed by finding the 200 ns time window (N_{200}) that contains the maximum number of hits in the event's hit PMT time distribution. The number of noise hits (N_{noise}) expected in this 200 ns time window is calculated using hits from outside this time window. The number of signal and noise hits are used to calculate the significance:

$$\text{significance} = \frac{N_{signal}}{\sqrt{N_{noise}}} = \frac{N_{200} - N_{noise}}{\sqrt{N_{noise}}} \quad (2.4)$$

The calculation of significance and N_{noise} is repeated for a set of progressively smaller time sub-windows. The sub-window with the maximum significance is chosen and all hits in that sub-window are used as the selected hits in the vertex determination. No causality cut is performed by this fitting routine.

The best vertex location is again based on choosing the best gof value from a set of test vertices. In this case, the set of test vertices is a grid that uniformly fills the entire detector volume. Once a best fit point is found on this coarse grid, a smaller grid centered about the best fit point is

²named after the author, Kai Martens

used, and this process is repeated until a best fit vertex position is found. A more detailed discussion of the details of this fitter can be obtained in Reference [27]

Events with a second fit reconstructed vertex found inside the 2m fiducial volume are sent out of the detector for further analysis and archival to tape. Those that fit outside the fiducial volume are dropped from the data sample.

CHAPTER 3

DETECTOR CALIBRATION

Proper calibration of a detector the size of Super-Kamiokande is a difficult and time consuming task. First, proper calibrations of the PMTs are required to ensure that the recorded time and charge of each hit PMT are properly interpreted. These PMT calibrations provide the proper translation from counts in a TDC or ADC to nanoseconds or picocoulombs. Second, calibrations are also responsible for ensuring proper understanding of the detector components, such as the water. A continuous measurement of the water transparency is needed to properly correct the light collection for long-term variations in water quality. Third, the calibrations are responsible for converting the number of hit tubes in each event into an energy value. An electron linear accelerator (LINAC), with energies tunable from 5-16 MeV, is used to set this energy scale. The decay ^{16}N atoms, created by neutrons from a deuterium-tritium neutron generator (DTG), are used to cross check and perform direction and position dependence studies of the energy scale. A major part of this thesis work involved the design, construction, and operation of the DTG calibration system.

3.1 PMT Calibrations

PMT calibrations for the ID are carried out to set the gain, at both high light levels and single photo-electron light levels, as well as to measure the relative timing of each channel as a function of input light level. These

calibrations are only summarized here, and a more detailed discussion can be obtained in Reference [27]. PMT calibrations for the OD[28] are also performed, but are not discussed here. These calibration constants are used to correct the recorded PMT data before any analysis is performed.

- PMT Relative Gain

The relative gain of each PMT is measured at high light levels (100-200 p.e.) using a Xe flash lamp, attached by optical fiber to a scintillator ball placed in the SK detector. The light level recorded by each tube is corrected for attenuation, acceptance and source uniformity to produce a “corrected Q” for each tube. The mean value of this “corrected Q” is adjusted by changing the high voltage of each PMT until all “corrected Q” values are nearly equal. The gains are set to be consistent within 7% of each other, and any remaining difference after the high voltage adjustment is corrected in software.

- PMT Absolute Gain

The absolute gain of each PMT at the single photo-electron light levels is measured using gamma rays from the nickel-californium calibration source (see Section 3.4). As the maximum gamma energy produced is about 9 MeV, each hit PMT only sees light at the 1 photo-electron level. The single photo-electron peak for a single tube generated in this manner is shown in Figure 2.6. The peak charge value for each channel is found and used as a charge/p.e. conversion factor for that channel. The mean charge/p.e. conversion factor for all ID PMTs is 2.05 pC/1 p.e.

- PMT Timing

The relative timing offsets of each PMT must be measured to correct for channel-to-channel variations in signal cable length and response time of the electronics. This will ensure that the recorded PMT hit times are all relative to the global trigger time. This correction depends on the input light level, as the arrival time will be shifted to earlier times as the light level increases, an effect known as *slewing*.

A laser calibration system is installed to measure these timing offset values. A pulsed nitrogen laser, with a ~ 3 ns pulse width, that is attached by optical fiber to a light diffuser located in the SK detector is used. The timing offsets are measured at light levels ranging from ~ 1 p.e. to several hundred p.e and are used to generate a “TQ map”, a lookup table of the timing offset for each PMT tube as a function of the measured light level.

3.2 Water Transparency Measurement

Cherenkov photons may travel up to 50 meters in the SK detector before they reach a PMT tube. At these distances, the loss of light due to absorption and scattering becomes significant and must be corrected for. To monitor the transparency of the water, two techniques are used. First, the wavelength dependence of the water transparency is measured using a tunable laser and CCD camera. This wavelength dependence is used to tune the Monte Carlo (MC) simulation. Second, the long term variation in the water transparency must be measured to obtain an energy scale that is not strongly dependent on the water quality. The decay of stopped muons is used for this purpose.

3.2.1 Laser Measurement

The laser measurement of the water transparency is performed using the system illustrated in Figure 3.1. At the center of this calibration system is a N₂ dye laser that produces monochromatic light with wavelengths from 337 to 600 nm. This light is sent by optical fiber to a MgO diffuser ball located in the SK tank. The signal from the diffuser ball is recorded with a CCD camera, and this measured signal is normalized by the signal from the reference PMT monitoring an integrating sphere. The normalized signal intensity from the CCD camera is measured at various depths in the detector ($I(d)$), and the measured results are fit to an exponential:

$$I(d) = I_0 \exp\left(-\frac{d}{\lambda}\right) \quad (3.1)$$

where λ is the water transparency determined by the fit and I_0 is an arbitrary normalization factor. The results from a 400 nm transparency are shown in Figure 3.2. A water transparency of $72.1 \text{ m} \pm 3.2 \text{ m}$ is found at 400 nm.

3.2.2 Decay Muon Measurement

The long term variation of the water transparency is measured using the decay electrons of stopped muons. This measurement is performed using data taking during normal detector operation, and minimizes the detector down time that would be required to make a weekly laser measurement. As this measurement uses real Cherenkov light, the water transparency value obtained is averaged over the Cherenkov spectrum, and is not directly comparable to the mono-chromatic measurements. The obtained value is instead used as an overall correction factor to remove long term variations in the water quality from the measured energy scale.

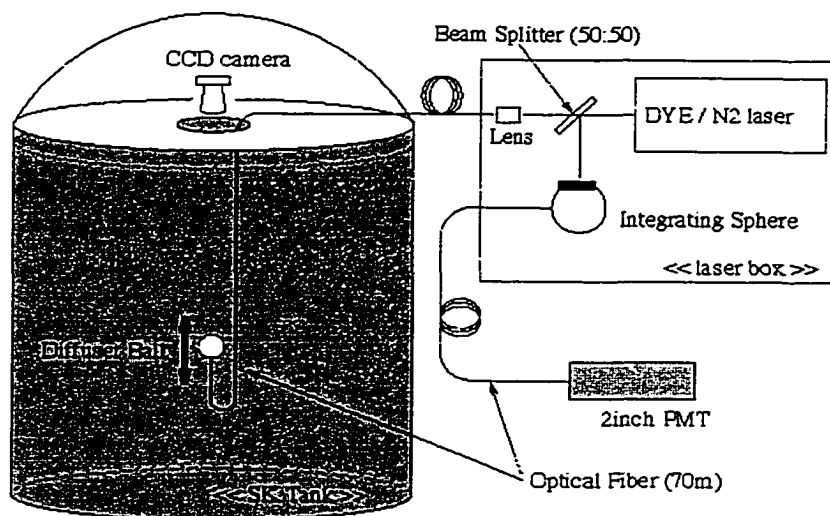


Figure 3.1: Schematic diagram for the system used to make laser measurements of the wavelength dependence of the water transparency.

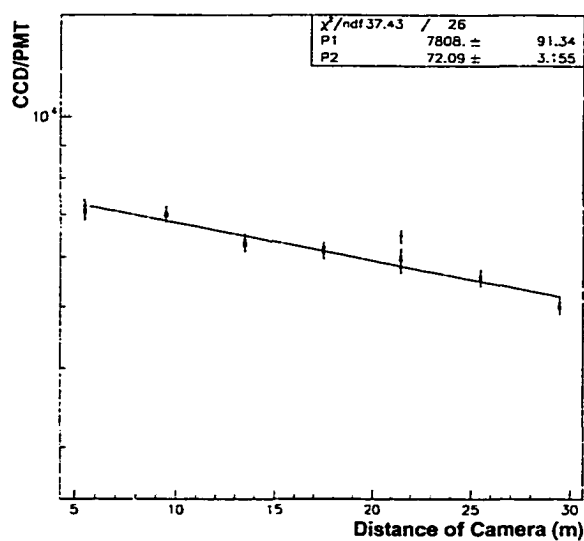


Figure 3.2: Water transparency measurement at 400 nm showing the normalized CCD signal as a function of diffuser ball depth in the detector. The measured transparency of 72.1 ± 3.2 m is obtained.

To perform this measurement, stopping muons are selected that meet the following criteria:

- The decay electron event must follow the stopping muon event within a 1.5-8 μsec time window. This ensures a relatively pure sample of decay electrons, as stopped muons decay with a half life of 2.04 μsec in water.
- The decay electron event must have a N_{eff} value greater than 70 (~ 10 MeV). This is to ensure that enough Cherenkov light is available to generate enough hits to perform the analysis.

These selection criteria generate $\sim 1,500$ decay events per day for this analysis. Once an event has been selected and the vertex and direction of the decay electron have been determined, the PMT hits used in the water transparency analysis are selected.

The hit selection criteria used is illustrated in Figure 3.3. Only hit PMTs that arrive within a 50 ns timing window from the reconstructed vertex position are taken. This eliminates tube hits from dark noise and reflected light. Next, only tube hits that are within a cone of opening angle 32° to 52° with respect to the reconstructed direction are taken. This ensures that only direct light is used in this analysis by removing scattered light. The selected hits on this ring are divided into 36 equal bins, and the N hits in the i_{th} bin are grouped together:

$$\Delta Q_i = \sum_{j=1}^N q_j \exp\left(\frac{d_j}{\lambda_e}\right) \quad (3.2)$$

where q_j is the charge measured in each selected PMT, d_j is the distance from the reconstructed vertex to each hit tube, and λ_e is the relative water

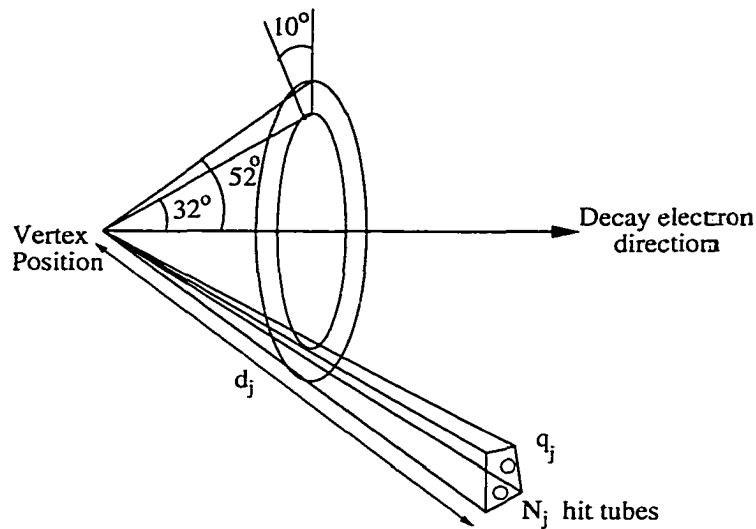


Figure 3.3: Schematic of the hit selection criteria used in the relative water transparency measurement from decay electrons. Only hit tubes that fall within a ring of opening angle of 32° to 52° are selected. This ring is divided into 36 equal bins, and each bin is treated separately.

transparency. The size of each bin can be regarded as small, and the charge in each bin can be rewritten as:

$$\Delta Q_i = \exp\left(\frac{r}{\lambda_e}\right) q(r) \quad (3.3)$$

where $r = \sum_{j=1}^N \frac{d_j}{N}$ is the mean distance to the hit tubes in each bin, and $q(r) = \sum_{j=1}^N q_j$ is the total charge in that bin.

The ΔQ_i value for all bins in any event should be equal, as it has been corrected for attenuation due to water transparency. The collected charge values can be averaged over the entire Michel spectrum by taking bins from many different events:

$$\overline{q(r)} = \exp\left(-\frac{r}{\lambda_e}\right) \overline{\Delta Q_i} \quad (3.4)$$

$$\log(\overline{q(r)}) = -\frac{r}{\lambda_e} + \log(\overline{\Delta Q_i}) \quad (3.5)$$

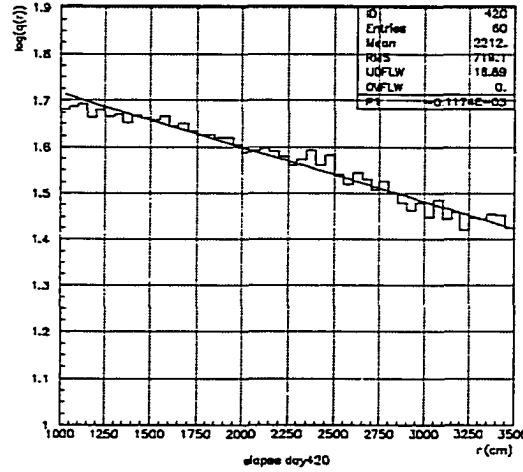


Figure 3.4: Distribution of $\log(q(r))$ versus r for a single days worth of decay electron events. This distribution indicates a relative water transparency value of 85.2 m.

In this manner, all decay electron events from a single day can be combined by plotting the $q(r)$ value versus r value for the 36 bins in each event. Figure 3.4 shows the distribution of $\log(q(r))$ versus r for a typical day's events. The inverse of the slope of this distribution is taken as the relative water transparency for that day. Data from a single week are combined, and a weekly water transparency value is calculated. The weekly water transparency value as a function of the detector operational time is shown in Figure 3.5. This relative water transparency value is used in the calculation of N_{eff} (see Section 4.3) to correct for the time dependence of the water transparency.

3.3 LINAC Energy Scale Calibration

To determine the energy scale, that is the conversion from the effective number of hit tubes (N_{eff} , see Section 4.3) to total electron energy, a linear

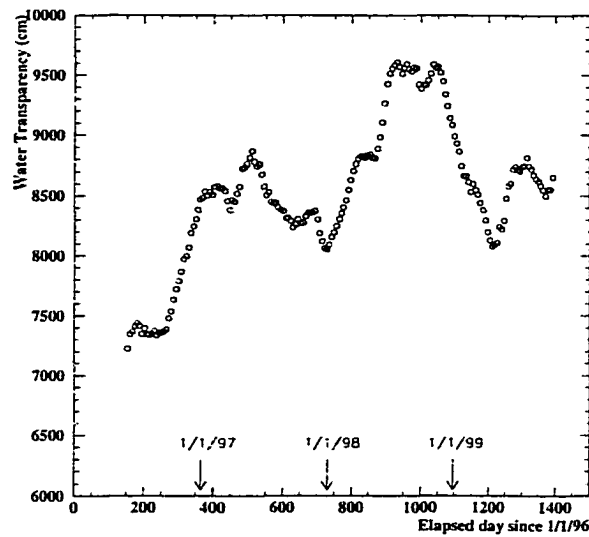


Figure 3.5: Relative water transparency as measured by the decay of stopping muons as a function of time. Time is measured in the number of elapsed days since 1/1/96.

accelerator of electrons (LINAC) is used. The LINAC produces downward-directed electrons inside the detector with a tunable energy, ranging from 5 to 16 MeV. This energy range is well matched to the energy range of recoil electrons from solar neutrinos.

Data collected with the LINAC calibration system at several different positions and energies are used to tune the detector response and set the absolute energy scale of a MC detector simulation. This tuned MC is then used to extrapolate the LINAC calibration to the entire range of energies, in all directions and over the entire detector volume. Remaining differences between the LINAC data and MC, as well as data from the DTG calibration (see Section 3.5), are used to evaluate systematic errors for the analysis of ${}^8\text{B}$ neutrinos.

3.3.1 LINAC Hardware

The LINAC is located 15m from the top of the SK detector, inset into the rock wall of the cavern, as illustrated in Figure 3.6. The LINAC is a Mitsubishi model ML-15MIII that was originally designed for medical uses. A detailed schematic of the LINAC and first bending magnet is shown in Figure 3.7. For operation at SK, a low-current electron gun was installed so that single electron flux levels could be obtained at end of the beam line. The beam is transported to the SK detector through 9 m of rock, across the top of the tank, and into the detector in a magnetically shielded, evacuated beam pipe. The end cap of the beam pipe, shown in Figure 3.8, is tapered to reduce the effects of shadowing and instrumented with a small scintillation counter that serves as a detector trigger. The end cap window is made of 100 μm -thick titanium to resist the forces of the external water pressure. The end cap is also equipped with scintillation counters ~ 80 cm from the exit window to veto events containing misaligned electrons. Additional information regarding the LINAC calibration system can be found in Reference [29].

Data may be collected at any of the 8 representative positions shown in Figure 3.6. Different depths in the detector are reached by adding additional beam pipe segments using the tower crane. At each position, 7 different electron energies are injected, ranging from 4.89 to 16.09 MeV. The absolute energy of the electrons from the LINAC system is measured using a germanium detector (Seiko-EG&G-Ortec model GMX-35210-P) with a germanium crystal 5.8 cm in diameter and 6.6 cm in length. The germanium detector is calibrated using various gamma sources as well as a calibration performed

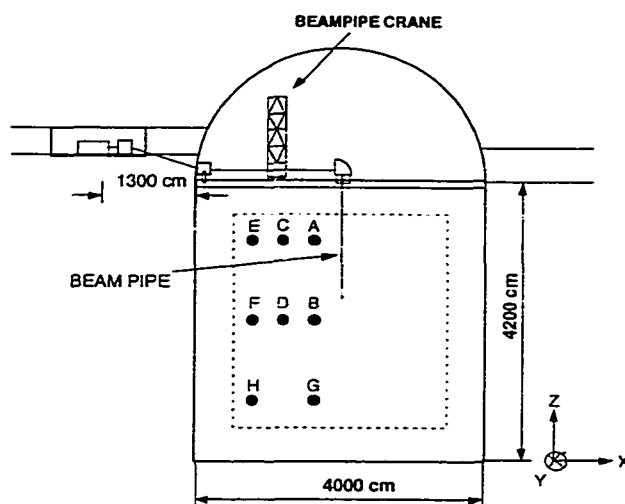


Figure 3.6: Schematic view of the LINAC and associated beam line. The lettered positions in the SK detector represent the locations where LINAC data has been taken.

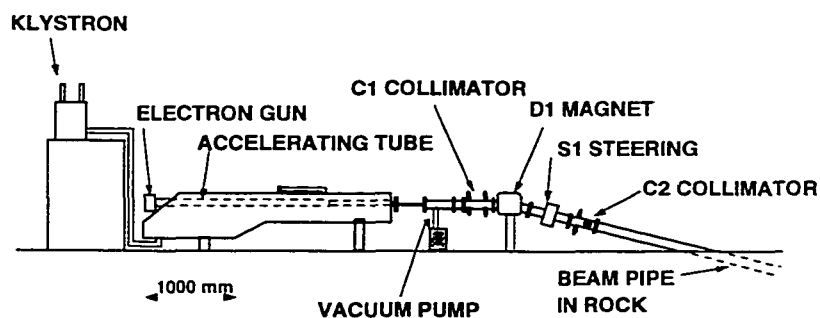


Figure 3.7: Detailed schematic view of the LINAC system, including the first bending magnet (D1). The current in the D1 magnet determines the beam momentum.

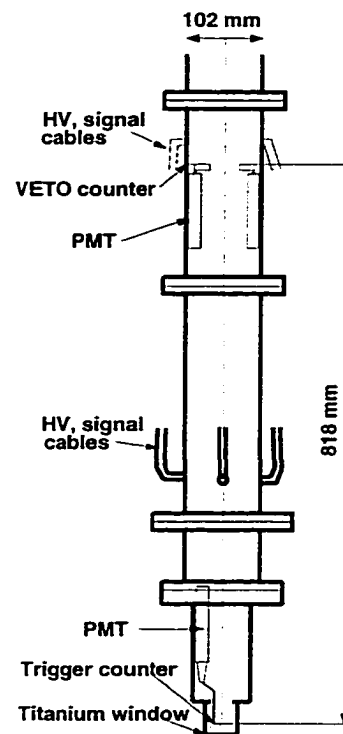


Figure 3.8: Schematic view of the beam line end cap. A scintillation counter used for triggering is located just above the $100\mu\text{m}$ Ti end cap. Also shown are the scintillation counters to detect off axis electrons.

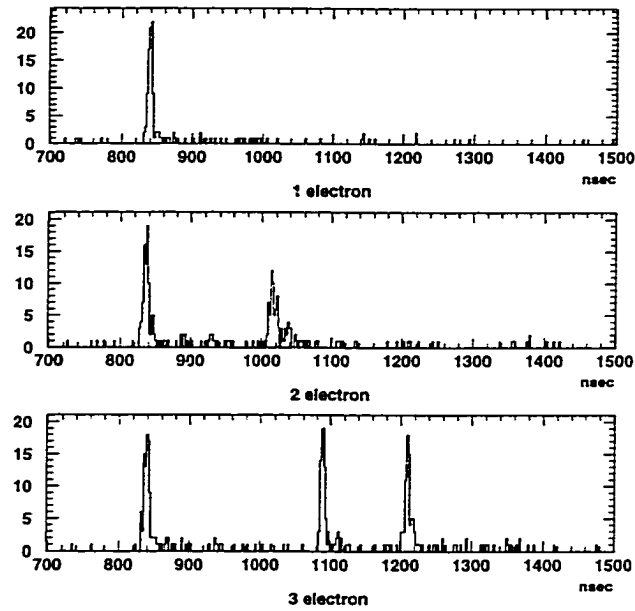


Figure 3.9: Time-of-flight corrected hit time distributions for events that contain 1 electron, 2 electrons and 3 electrons.

with internal conversion electrons from a ^{207}Bi source with energy selection performed by a beta spectrometer located at KEK-Tanashi.

Beam spills from the LINAC occur at a maximum rate of 60 Hz, with an average occupancy at the beam pipe end cap set to 0.1 electrons/spill. This low occupancy helps to reduce the number of events that could contain more than a single electron per spill. To remove any remaining multiple electron events, an additional cut is applied to the collected data. The time-of-flight corrected hit times, relative to the end cap location, of all hit PMTs are histogrammed for each event (see Figure 3.9), and the number of peaks is counted. Only events with a single peak are accepted for calibration purposes.

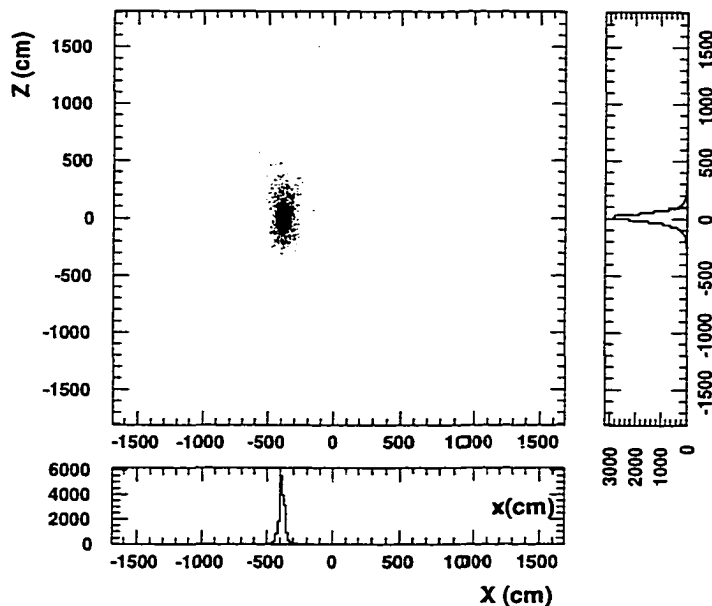


Figure 3.10: Reconstructed vertex position distribution for LINAC data taken at $(x,z) = (-4 \text{ m}, 0 \text{ m}, 0 \text{ m})$. A 2d scatter-plot and projections to the x and z axis are shown.

3.3.2 Results from the LINAC Calibration

Once the LINAC data are collected, they are passed through the same data reconstruction routines used for the solar neutrino analysis (see Chapter 4), including vertex position, direction and energy reconstruction. The reconstructed vertex distribution for a representative point $(-4 \text{ m}, 0 \text{ m}, 0 \text{ m})$ is presented in Figure 3.10. A sample of LINAC MC events are generated using the detector simulation, with all LINAC-related hardware included. The reconstructed energy distributions for LINAC data and MC from a representative position for each beam energy collected are shown in Figure 3.11.

The LINAC data are compared to the MC data sample as a check of the energy scale. Each energy distribution, as shown in Figure 3.11 is fit with a

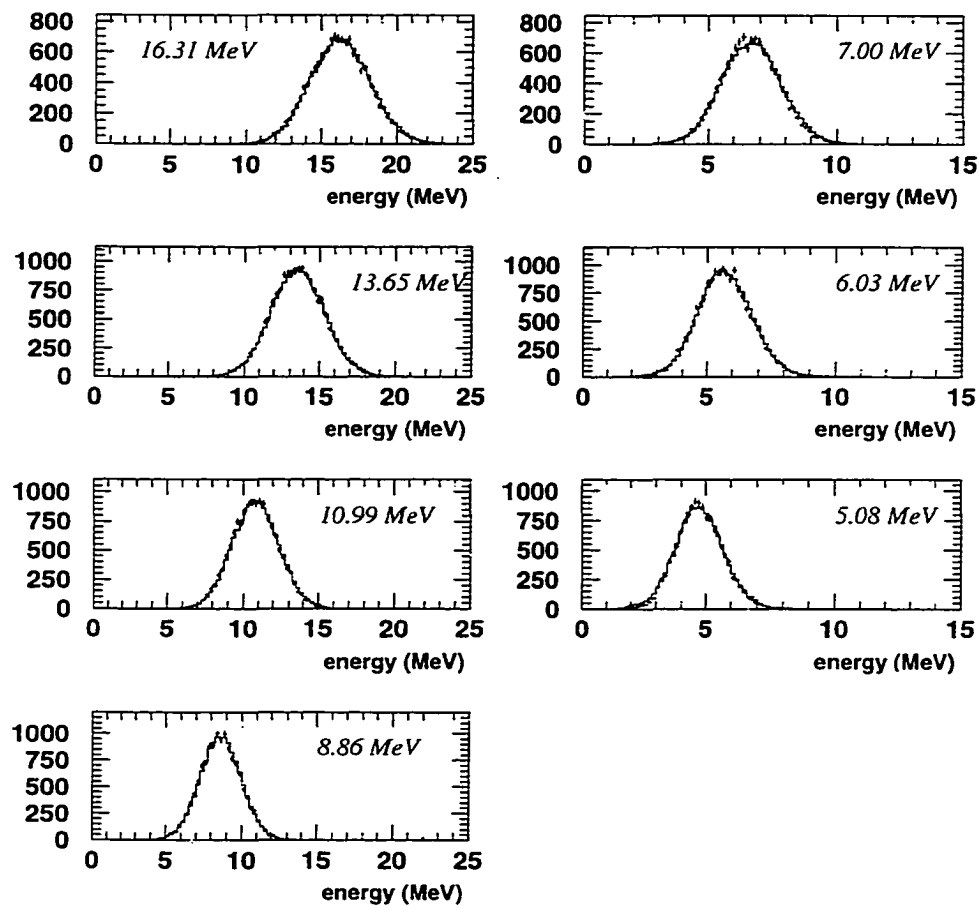


Figure 3.11: Reconstructed energy distributions for LINAC data (points) and MC (line) for the 7 energy modes from the $(x,z)=(-12\text{ m},+12\text{ m})$ position.

Gaussian curve, and the obtained peak position is taken as the measure of the energy scale at that beam energy. The 1σ width of the fit is used to measure the energy resolution. The same fit is performed for MC events, and the results from DATA and MC are compared at each position and energy. The deviation in the energy scale ($\frac{Data-MC}{Data}$) is found for each point and is plotted in Figure 3.12. The results from all LINAC positions are combined, and an averaged result at each energy value is obtained. These values represent the total energy scale uncertainty and are shown in Figure 3.13 with statistical and systematic errors of the LINAC calibration system included. As the energy of LINAC electrons decrease, a larger fraction of Cherenkov photons will strike LINAC-related equipment, most notably the beam line end cap. The large systematic errors at low energy arise from uncertainties in the reflectivity of these surfaces. The differences and errors are well within the $\pm 1.0\%$ range for the region of interest for the solar neutrino analysis.

The LINAC data are also used to obtain the angular, vertex and energy resolution of the detector as a function of energy. These measured resolutions are summarized in Table 3.1. The energy resolution is taken from the width of the Gaussian fit performed on the reconstructed energy distribution. The vertex resolution is defined as the size of a sphere that contains 68% of the reconstructed event vertices. The angular resolution is defined as the opening angle relative to the injection direction that contains 68% of the reconstructed directions. The averaged angular resolution difference between LINAC data and MC is shown in Figure 3.14. A 1.5% systematic difference is found in energy resolution, with the MC having the better energy resolution. The

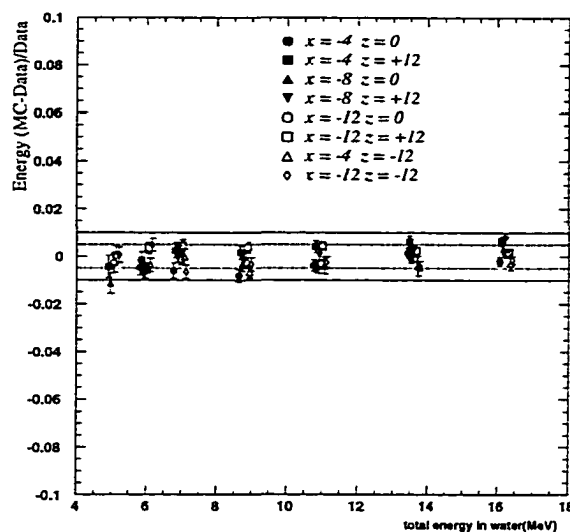


Figure 3.12: Measured energy deviation ($\frac{Data-MC}{Data}$) for each position and energy measured with the LINAC. Errors shown are statistical only. Dashed lines represent $\pm 0.5\%$ and solid lines represent $\pm 1.0\%$.

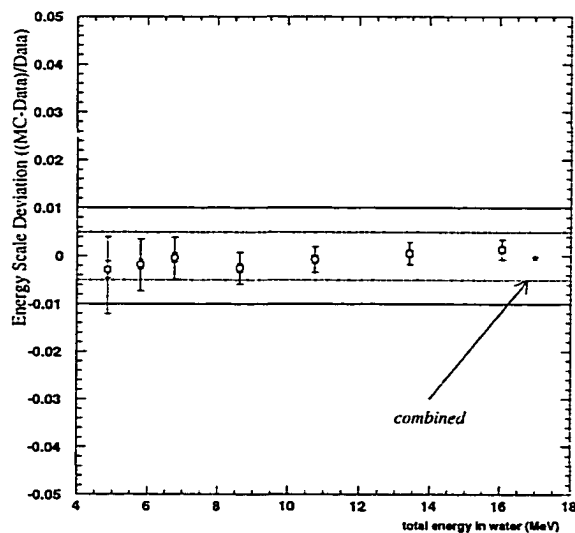


Figure 3.13: Averaged energy deviation ($\frac{Data-MC}{Data}$) at each energy value. Inner error bars represent statistical errors, while outer error bars represent the total error. Dashed lines represent $\pm 0.5\%$ and solid lines represent $\pm 1.0\%$.

Table 3.1: Summary of LINAC measured detector resolutions.

Electron Total Energy (MeV)	Energy Resolution (%)	Angular Resolution (degrees)	Vertex Resolution (cm)
4.89	21.4 ± 0.2	36.8 ± 0.1	178.8 ± 0.5
5.84	18.5 ± 0.1	34.5 ± 0.1	132.7 ± 0.4
6.79	17.9 ± 0.1	32.0 ± 0.1	107.8 ± 0.2
8.67	16.3 ± 0.1	28.4 ± 0.1	85.2 ± 0.2
10.78	14.8 ± 0.1	25.3 ± 0.1	72.9 ± 0.1
13.44	13.7 ± 0.1	22.5 ± 0.1	64.6 ± 0.2
16.09	12.7 ± 0.1	20.5 ± 0.1	59.7 ± 0.1

averaged energy resolution difference between LINAC data and MC is shown in Figure 3.15. The angular resolutions of the data and MC agree within $\pm 3\%$ for the energy range used in this analysis (5.5-20 MeV). These values are later used to search for systematic differences in the ^8B flux and spectrum measurements arising from these systematic differences.

3.4 Nickel-Californium Calibration Source

Gamma rays emitted by the thermal capture of neutrons on nickel wire ($\text{Ni}(n,\gamma)\text{Ni}$) are also used for calibration of the SK detector. Originally designed for energy scale calibration, uncertainties in the branching ratios and neutron absorption cross sections for different Ni isotopes limited the accuracy of this calibration. Therefore, the Ni source is used as a supplementary calibration source for evaluation of systematic errors and measuring the trigger efficiency. More details regarding the nickel calibration source are available from References. [27, 31].

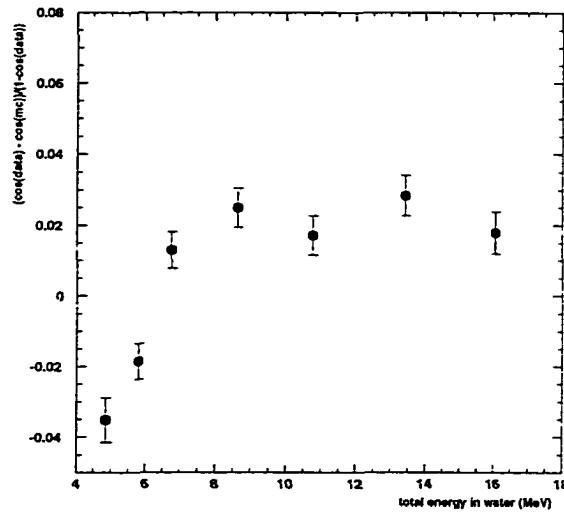


Figure 3.14: Averaged angular resolution difference as a function of energy. Errors shown are statistical only.

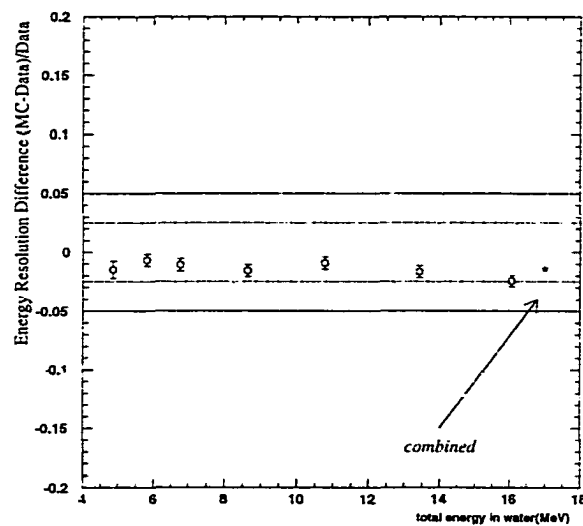


Figure 3.15: Averaged energy resolution difference ($\frac{Data-MC}{Data}$) as a function of energy. The combined point is an average over all energy values. Dashed lines represent $\pm 2.5\%$ and solid lines represent $\pm 5.0\%$. Errors shown are statistical only.

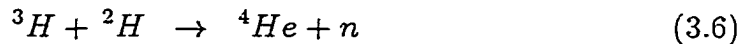
3.5 The DTG Calibration

The LINAC calibration has some limitations. The electrons produced are only downward-going when they exit the beam pipe. This introduces the possibility of an undetected direction dependence for the energy scale. The presence of the LINAC equipment in the tank during the calibration runs is another limitation. While this equipment is modeled in the LINAC simulation, it is still the largest source of systematic error for the LINAC calibration. Finally, the LINAC system can only be operated at a limited number of positions, with only 8 positions having been used so far. All of these positions are on the -X axis of the detector, and this calibration must be extrapolated to the entire detector volume, perhaps missing an unknown position dependence to the energy scale.

To supplement and cross-check the LINAC energy scale calibration, a new calibration source was built, one that addressed the limitations of the LINAC system. A deuterium-tritium neutron generator (DTG) pulsed calibration source was built and installed at SK. The DTG provides a source of 14.2 MeV neutrons which interact by the (n, p) reaction with ^{16}O in the water of the SK detector, creating ^{16}N . ^{16}N beta decays with a half life of 7.13 sec, and these decay events are used for calibration. The decay is isotropic, providing a way to check the energy scale in all directions. The ^{16}N is produced *in situ*, and the DTG equipment is withdrawn from the volume containing ^{16}N , providing a calibration source free from calibration equipment. The DTG system is designed to be easily portable, allowing operation at any calibration port in the SK detector.

3.5.1 DTG Equipment

At the center of the DTG calibration system is a MF Physics model A-211 pulsed neutron generator. The neutron generator creates neutrons by the deuterium-tritium reaction:



This reaction yields 14.2 MeV neutrons that are isotropically distributed. This commercially available unit consists of three pieces:

- An accelerator control unit where the high voltage (~ 500 V) supply, accelerator controls and operational interlock are located.
- A pulse-forming electronics unit where the ~ 100 kV pulses used by the accelerator are generated.
- An accelerator head that contains the deuterium/tritium ion source and target. The neutrons are created here.

The nature of the high voltage pulses between the pulse-forming electronics unit and the accelerator head limits the length of cables used to connect these units to a couple of meters. For operation at SK, where the separation between the accelerator control unit and the accelerator head could be up to 50 m, the pulse forming electronics unit was repackaged by MF physics, so that it could be directly attached to the accelerator head.

The pulse-forming electronics and accelerator head combined unit is lowered into the SK detector, and is used to generate neutrons *in situ*. This combined unit is encased in a water-tight stainless steel housing, as shown in Figure 3.16. The housing measures 150 cm in length and 16.5 cm in

diameter, fitting easily into the calibration ports provided on the top of the SK detector. The pulse-forming electronics unit is attached to the accelerator control unit by a cable bundle containing 10 coaxial cables for high voltage and accelerator control signals. The stainless steel housing is topped with a PVC end cap, with a custom-made, epoxy-filled cable feed-through. The housing also contains a water sensor, to detect water leaks. An ultrasonic water sensor (Omega LVU-700) is located on the top of the housing and is used as an operational interlock to ensure that the generator is only operated while submerged in the tank.

The DTG generates neutrons by colliding deuterium and tritium ions with a fixed metal hydride target, also containing equal parts of deuterium and tritium. These ions are created by a Penning ion source, using electric and magnetic fields to create a plasma along the source anode, and trapping the resulting electrons which ionize gas in the source region (see Figure 3.16). The gas pressure is regulated by the gas reservoir element. The deuterium and tritium ions are accelerated toward the target through an accelerating voltage of 80-180 kV. The target is biased positively with respect to the accelerating anode to prevent secondary electrons from damaging the ion source. The ion source, accelerating anode and target are enclosed in an evacuated enclosure, which is in turn enclosed in a protective aluminum housing. The pulse-forming electronics are enclosed in a similar aluminum housing and both units are filled with Shell Diala AX transformer oil for insulation and cooling.¹ The neutron generator can be pulsed at a maximum rate of 100 Hz, with each pulse yielding approximately 10^6 neutrons.

¹The original fluorine-based insulating fluid was replaced with oil to remove contamination from ^{16}N produced inside the generator from the (n, α) reaction on ^{19}F .

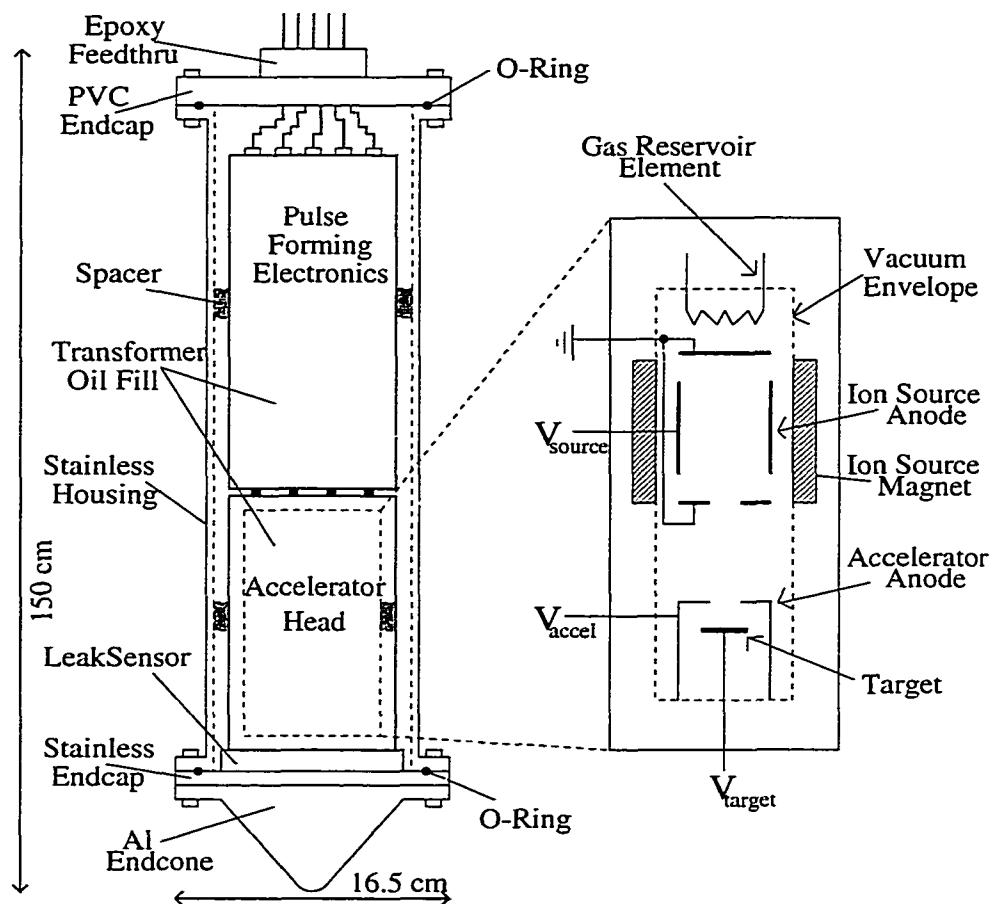


Figure 3.16: Schematic of the DTG accelerator head and pulse-forming electronics unit encased in the stainless steel housing. Additionally, the internal components of the accelerator head are shown.

The DTG is positioned in the SK detector using a custom-built computer-controlled crane. The crane was built by Allied Power Products of Beaverton, OR. It is built around a Columbia GVL 300 crane frame with a 3 phase variable-speed electric motor. The motor is controlled by a Durant programmable sequential controller (model 56460-400). The crane is equipped with 170' of 1/8" wire rope. The sequential controller is programmed with a simple algorithm that lowers the load for a fixed period of time, then raises it again. This program is initiated by remote command.

The crane is controlled by a Pentium computer running the LINUX operating system. A Computer Boards I/O card (model CIO-DIO24) is used to control a custom built interface box by a C program on the computer. The interface box is capable of initiating the raise/lower program on the sequential control of the crane, setting and removing the veto for the SK data acquisition (DAQ) system, and firing the DTG. The interface box can also relay status messages from the crane to the control PC, sent when the crane has finished moving up or down. The control program running on the PC directs the overall flow of data taking with the DTG.

The 14.2 MeV neutrons produced by the DTG are energetic enough to produce ^{16}N by the (n,p) reaction on ^{16}O in water of the detector. The measured cross section for this reaction is shown in Figure 3.17. The cross section for 14.2 MeV neutrons is about 40 mb. A simulation of neutrons in water using GCALOR and GEANT[32] was used to determine the expected yield, defined to be the fraction of neutrons that create ^{16}N in the water of SK. The expected yield was found to be 1.3%. The actual yield found during

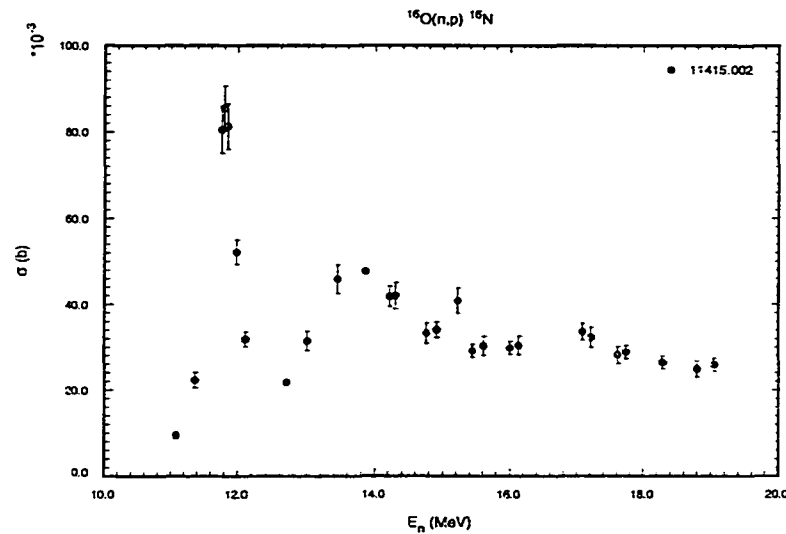


Figure 3.17: Measured (n, p) cross section for ^{16}O as a function of energy[30].

data taking at SK was $\sim 1\%$, in good agreement with the expected yield given the uncertainties in the absolute neutron flux. This simulation was also used to determine the average distance the neutrons traveled before creating ^{16}N . This distribution is shown in Figure 3.18, with a mean value of 20 cm.

The data taking cycle used while taking data in the SK detector is shown in Figure 3.19. Before the start of each cycle, the DTG is positioned 2 m above the position where data is to be taken. At the start of the cycle, the DTG is lowered 2 m into place and a veto to the SK DAQ is set, preventing data collection. Once in the proper position, the DTG is fired, creating a cloud of ^{16}N in the water around the end of the generator. Each time the DTG is fired it is actually pulsed three times at a rate of 100 Hz (30 ms to fire), producing ~ 3 million neutrons. Immediately after firing, the DTG is raised 2 m, leaving the cloud of ^{16}N to decay, well away from the DTG

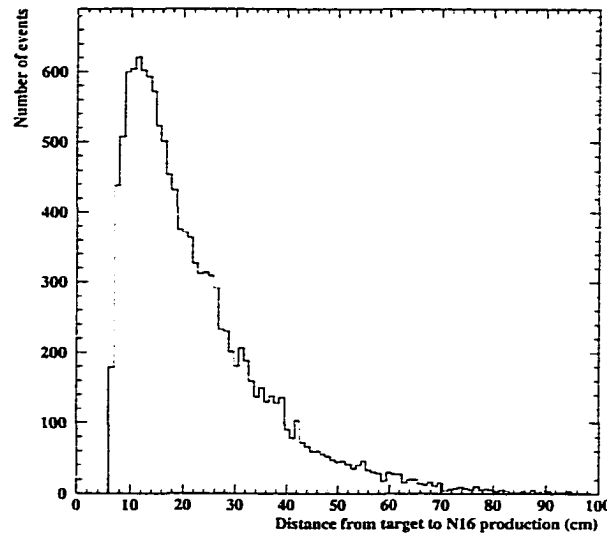


Figure 3.18: Distribution of neutron travel distance between the target production point to the creation point of ^{16}N from the neutron simulation.

equipment. The crane requires ~ 10 sec to withdraw the DTG and during this time roughly 60% of the ^{16}N created will decay. No data are collected while the crane is moving to prevent contamination of the data, as the motor generates a significant amount of electrical noise while in motion. Once the crane has stopped moving, data are collected from the decay of the remaining ^{16}N events. This cycle is repeated 25 times at each position in the SK tank, yielding a sample of $\sim 300,000$ ^{16}N events collected by SK.

3.5.2 Results from the DTG Calibration

Data collected during the DTG calibration runs are subjected to the same reconstruction as the solar neutrino data sample (see Chapter 4). Even though no special trigger is used to collect the ^{16}N decays from the DTG, a subtraction of the natural background is not required. In the fiducial volume, the natural background contributes $\ll 0.1\%$ to the data sample collected. The

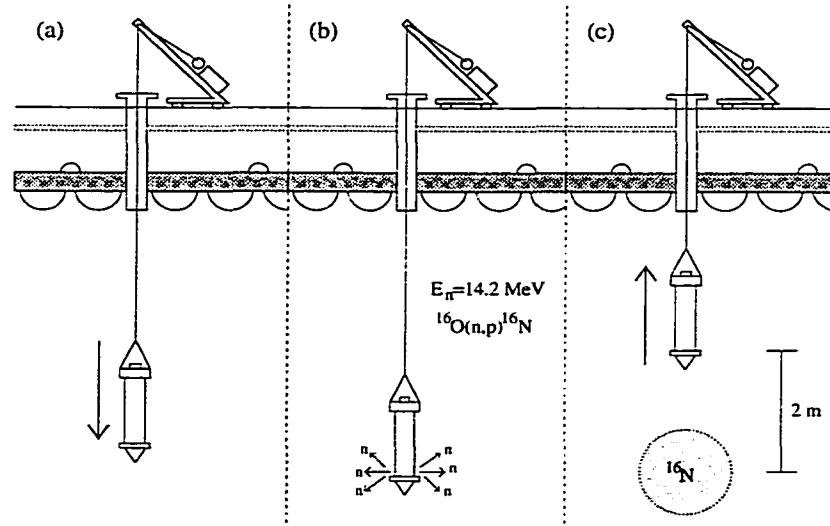


Figure 3.19: Overview of the DTG data taking cycle. In (a), the DTG is lowered to the position where data are to be taken. The DTG is fired in (b), and withdrawn (C) 2 m before data are collected.

reconstructed vertex distribution for a typical data taking run is shown in Figure 3.20. These distributions indicate that the cloud of ^{16}N is relatively undisturbed by the removal of the DTG, with just a small amount of smearing evident in the $+z$ distribution. The reconstructed direction distributions are consistent with an isotropic source.

For each position in the SK tank where the DTG is operated, an MC sample of ^{16}N events is created as well. Reflection of Cherenkov photons from the DTG equipment is included in this simulation, but is only expected for 0.1% of photons. The input to this MC is generated by a simulation of the decay of ^{16}N . All decay lines with a probability of 10^{-8} or greater are included in this simulation, and are listed in Figure 3.21. Also listed in the figure are the corrections for the beta spectrum included in the simulation and the

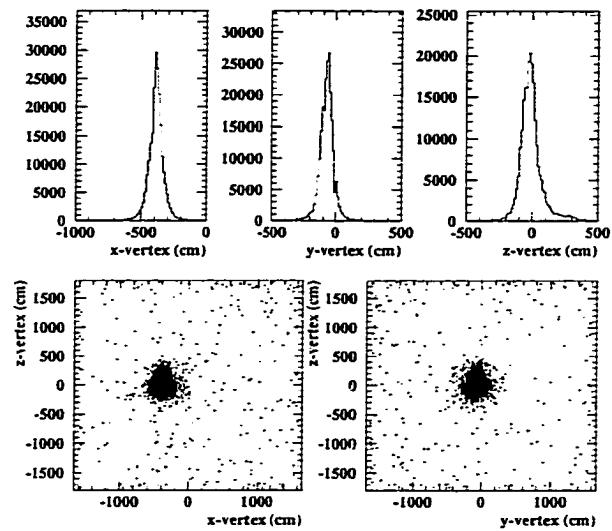


Figure 3.20: The reconstructed vertex distribution for a typical data taking run. These data were collected at $(-388.9 \text{ cm}, -70.7 \text{ cm}, 0 \text{ cm})$. The scatter plots of x - z and y - z vertex distributions each contain 10,000 events.

size of the effect on the overall spectrum[33]. These include corrections for nuclear recoil, the nuclear Coulomb field, finite nuclear corrections, Dirac wave function corrections and atomic screening. Additionally, the forbidden line shapes require corrections to the electron spectral shape[34]. These corrections mainly impact low energy electrons, and therefore have little overall effect, resulting in a 0.14% overall shift in the peak energy. These corrections mainly impact low energy electrons, and therefore have little overall effect. The modeled electron and gamma energies are then input into the detector simulation.

The same reconstruction is applied to the MC as to the data. The energy distributions for a representative position for both DTG data and MC are presented in Figure 3.22. The peak (~ 7 MeV) in the energy distribution is dominated by events with a 6.1 MeV gamma ray in coincidence with an electron of 4.3 MeV endpoint energy. 28% of the events contain an electron with an endpoint energy of 10.4 MeV and are the primary source of the observed high energy tail. The shape of the energy spectrum at low energies (< 5 MeV) is primarily determined by the trigger threshold of the detector. These distributions are fit with a Gaussian function between 5.5 MeV and 9.0 MeV, and the peak positions are found. These numbers serve as the measure of the absolute energy scale by calculating the deviation of peak positions, $\frac{MC-DATA}{DATA}$, and this procedure is repeated at each data position in the SK tank.

To obtain a global result from the data collected at many different positions in the SK detector, a position-weighted average is performed. Data

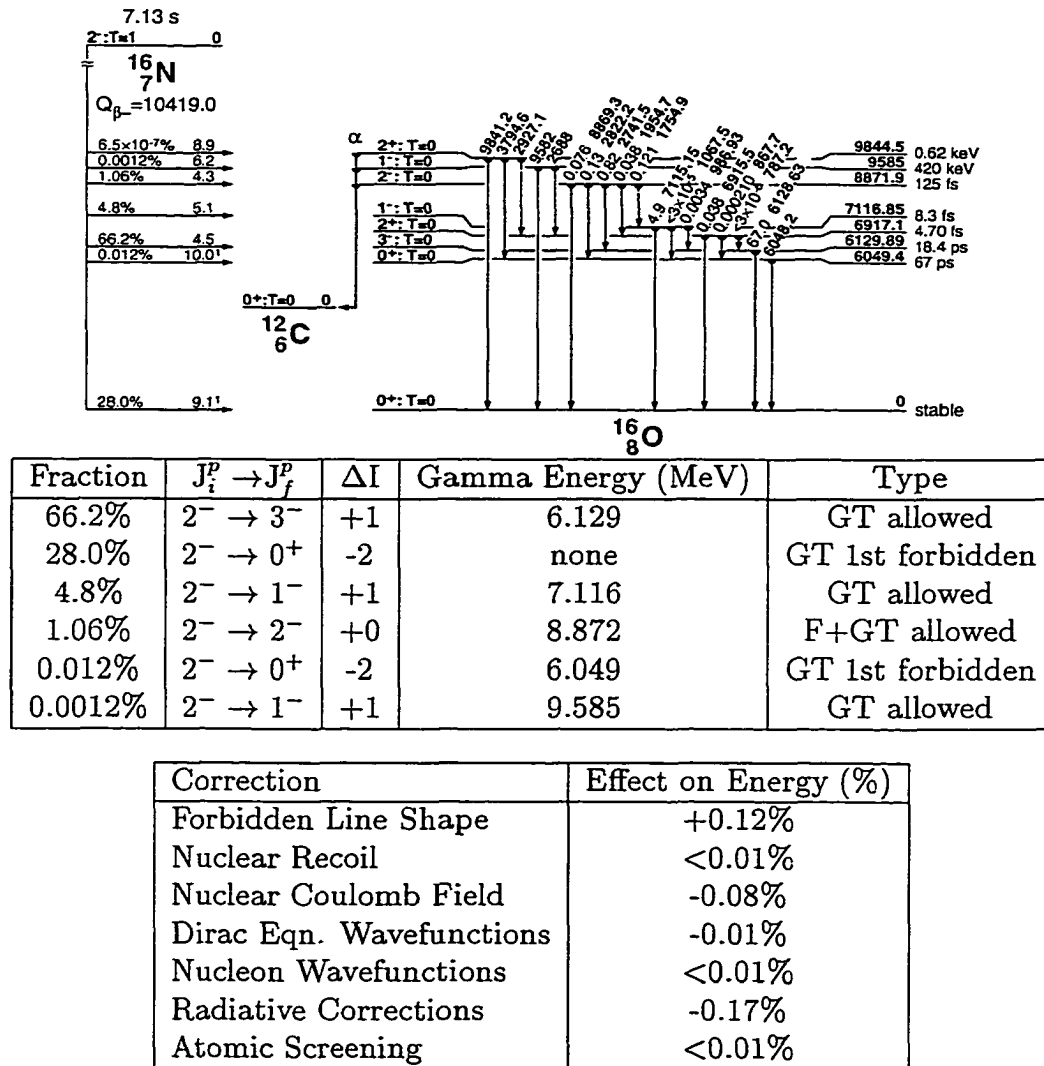


Figure 3.21: Model details for the decay of ^{16}N . The level diagram is taken from Reference [35]. Also listed are the included decay lines, as well as the corrections included in the decay simulation with the size of the correction on the overall energy spectrum.

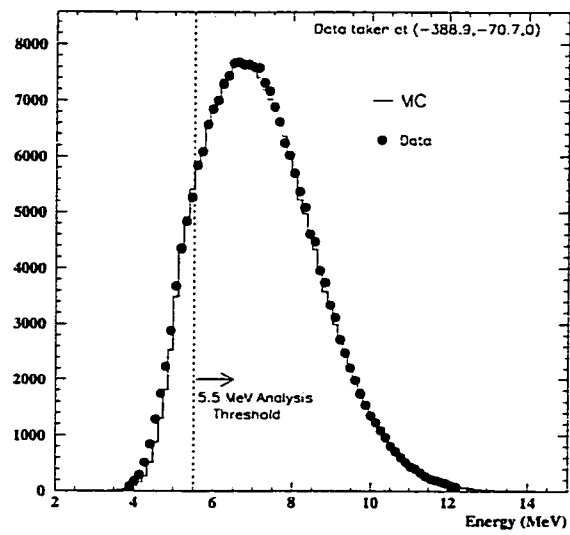


Figure 3.22: The reconstructed energy distribution for data and MC. The data (points) and MC (line) are fit with Gaussian functions above the 5.5 MeV analysis threshold. These data were collected at (-388.9 cm, -70.7 cm, 0).

Table 3.2: Position weights used in the position-weighted average for DTG data. The $r=1521$ has no weight as it is outside the fiducial volume.

r location (cm)	r weight (%)	z location (cm)	z weight (%)
79	2.53	1500	7.89
395	13.49	1200	14.04
797	30.69	600	18.71
1239	53.29	0	18.72
1521	0.0	-600	18.71
		-1200	14.04
		-1500	7.89

at SK were collected in 6 different calibration ports, representing 4 unique radial slices (r) of the fiducial volume, with 7 depths in the detector (z) at each port. Each slice of the detector in the r or z coordinate is assigned a weight based on the fraction of the 22.5 kton fiducial volume it represents. These weights for each r and z slice are listed in Table 3.2. Each position is assigned a weight by multiplying the r and z weight based on the location of the DTG data. As the solar neutrinos interact uniformly throughout the detector volume, this position-weighted average provides a more realistic representation of the energy scale than a simple average. The measured spectra for data and MC are combined based on these weights, and the position-weighted average energy spectrum from DTG data and MC created, shown in Figure 3.23. The agreement between data and MC is excellent.

The data from the DTG are also used to measure the position and direction dependence of the energy scale. The position dependence of the energy scale, shown in Figure 3.24, is obtained as a function of r and z by performing a position-weighted average over z and r , respectively. The

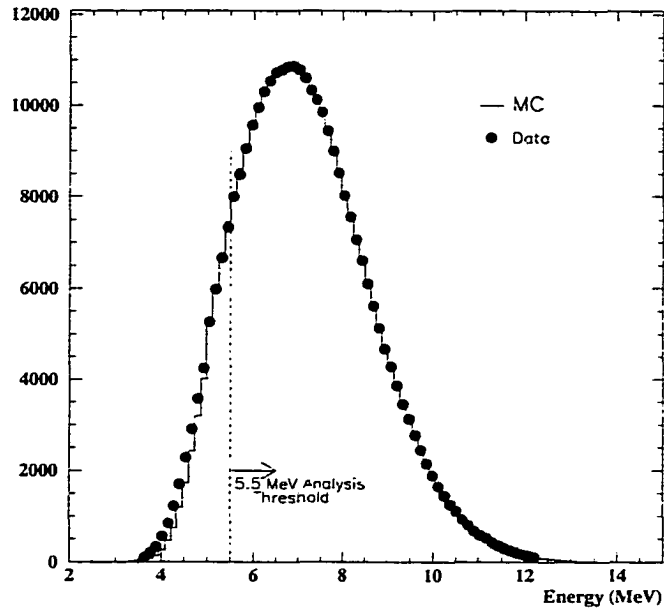


Figure 3.23: The position-weighted average energy spectrum for data (points) and MC (line).

direction dependence of the energy scale is obtained by dividing the data in subsets at each position based on the reconstructed direction, performing a Gaussian fit on the energy spectrum of each subset, and then performing a position-weighted average over all DTG data positions in the detector for each direction. The direction dependence is studied as a function of zenith angle, measured with respect to the vertical (z) axis of the detector, and as a function of azimuthal angle, measured in the x - y plane. The resulting angular dependence of the energy scale is presented in Figure 3.25. The measured position and direction dependence of the energy scale are used to determine systematic errors for the solar neutrino analysis (see Chapter 7).

As a check for background contamination from other nuclides, the half life of ^{16}N is measured using the collected data. The time since generator

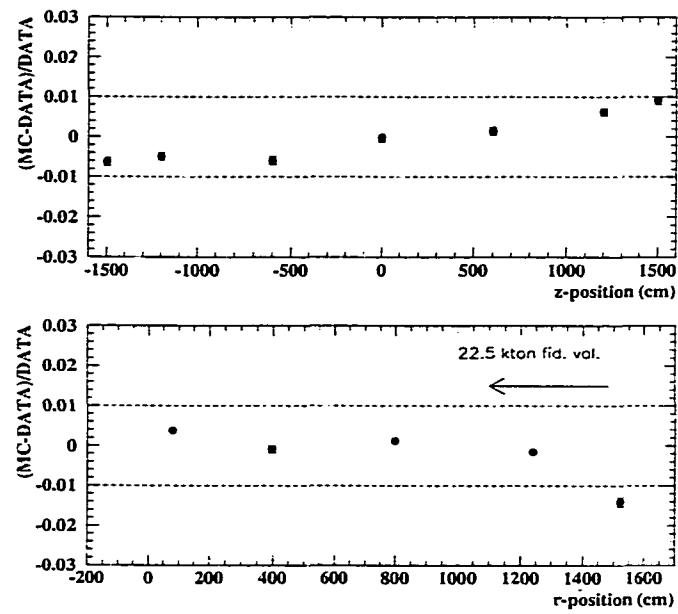


Figure 3.24: Position dependence of the energy scale as measured by DTG data. At each r and z vertex position, a position-weighted average over all z and r positions, respectively, is performed. Only statistical errors are shown. Dashed lines indicate deviations of $\pm 1\%$.

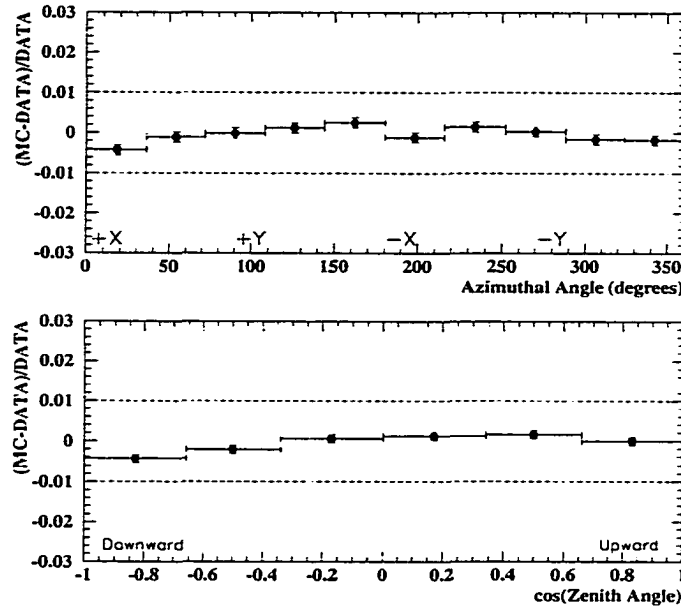


Figure 3.25: Angular dependence of the energy scale from DTG data. Dashed lines indicate deviations of $\pm 1\%$.

fire for each event collected is plotted, and the data from several positions are combined for additional statistical weight. The histogram of this decay time and the calculated best fit are shown in Figure 3.26. The best fit half life of 7.13 ± 0.03 sec is in excellent agreement with the expected value of 7.13 ± 0.02 sec[35], indicating that a clean sample of ^{16}N is obtained.

3.5.2.1 Systematic Errors of the DTG calibration

The systematic errors for the DTG calibration for the absolute energy scale measurement are summarized in Table 3.3. The systematic error for shadowing of Cherenkov photons by DTG related equipment after it is withdrawn is determined by the fraction of photons that could be absorbed, assuming a “black” housing, and is estimated to be $\pm 0.1\%$. The simulation of neutrons in the DTG setup indicates that small amounts of background

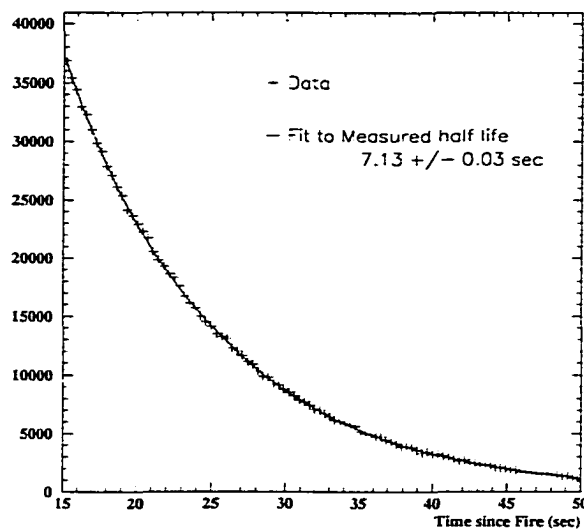


Figure 3.26: Distribution of time since generator fire for several DTG runs. Data with time since fire less than 15 sec are not included to ensure that all data are taken after the crane has been fully withdrawn.

Table 3.3: Summary of systematic errors from the DTG calibration.

Contamination from natural background	$< 0.01\%$
^{16}N MC decay modeling	$\pm 0.1\%$
Unmodeled decay lines	$< 0.01\%$
Shadowing of Cherenkov photons	$\pm 0.1\%$
DTG data selection systematic	$\pm 0.1\%$
DTG related radioactive background	$\pm 0.1\%$
Total Systematic Error	$\pm 0.2\%$

isotopes are created, including ^{24}Na , ^{62}Co , and ^{28}Al . Most nuclides created have long half lives and/or insufficient energy to trigger SK, but a MC simulation indicates a small amount of gamma contamination is possible, and a systematic error of $\pm 0.1\%$ is conservatively chosen. The DTG data selection systematic error results from a vertex position cut made to the data to remove background events occurring near the walls of the detector from the data sample.

The total position-averaged energy scale deviation, $(\frac{MC-DATA}{DATA})$, measured with the DTG calibration system is found to be $-0.04\% \pm 0.04\%(\text{stat.}) \pm 0.2\%(\text{sys.})$, indicating excellent overall agreement between the DTG data with the LINAC-based MC simulation.

3.6 Trigger Efficiency

The DTG and the nickel-californium calibration sources are used to measure the trigger efficiency as a function of energy. When making these measurements, an additional trigger level that corresponds to a 150 mV trigger (about 14 hits) is added. This trigger level is low enough to ensure a 100% trigger efficiency in the energy region where the SLE and LE triggers start to

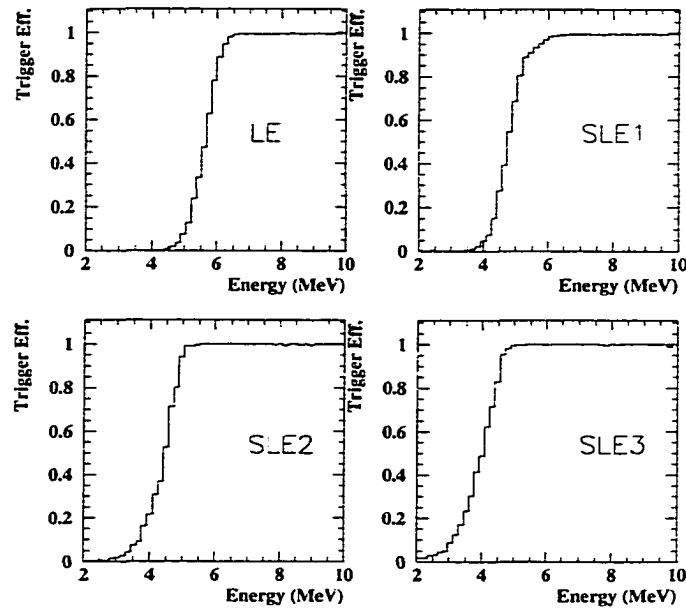


Figure 3.27: The measured trigger efficiency as a function of energy for the LE, SLE1, SLE2, SLE3 triggers. The LE and SLE1 trigger efficiencies are measured using the nickel-californium source, while SLE2 and SLE3 are measured with the DTG.

become inefficient. The trigger efficiency is then determined by finding the ratio of the number of events that trigger the LE/SLE trigger to the number of events that trigger the 150 mV trigger as a function of energy.

The measured trigger efficiency as a function of energy is shown for the LE, SLE1, SLE2, and SLE3 trigger levels is presented in Figure 3.27. For events with energies greater than 5.5 MeV, those events considered for the solar neutrino analysis, the SLE1 trigger efficiency is $>90\%$, and the SLE2 and SLE3 trigger efficiencies are $\sim 100\%$. Events collected during the LE-only run period are only considered for energies greater than 6.5 MeV, where the LE trigger efficiency is $\sim 100\%$.

CHAPTER 4

EVENT RECONSTRUCTION

This chapter details the event reconstruction algorithms, the results of which will be used in the reduction of the sample of events to a final sample of neutrino candidates. Events collected in SK are divided into two categories, depending on the total charge of all hit PMTs in the event. Events with 1000 p.e. or fewer are considered as candidates for the solar neutrino reduction. Events with greater than 1000 p.e. are considered muons, and are used in the spallation cut portion of the solar neutrino reduction.

For each event in the solar neutrino sample (<1000 p.e.), the vertex, direction and energy are reconstructed. Additionally, the “new goodness” cut and the “clusfit” vertex reconstruction algorithms are used to discriminate background events from scattered electrons from solar neutrinos. The results from these algorithms are later used in the data reduction portion of the solar neutrino analysis.

For each event in the muon sample (>1000 p.e.), a muon track fitter attempts to find the entry and exit point of each track. Multiple muons and stopping muons are also fit with this algorithm. These reconstructed muon tracks are used in the spallation cut to calculate likelihood values that are used to remove events that are likely spallation events.

4.1 Vertex Reconstruction

As previously discussed (see Section 2.7), the vertex reconstruction program used in the solar neutrino analysis uses the relative timing of each hit

PMT to determine the optimal fit location in the tank. This reconstruction is a two step process. First, the set of hit PMTs to be used in the fit is selected. Then, a vertex position that best represents the selected hits is determined by minimizing the timing residual of each selected PMT. The timing residual is the hit time of each PMT after it has been corrected for the photon travel time from the vertex location. The hit PMTs from a point source will ideally have zero timing residuals when the time of flight from the true vertex is considered.

Hit PMT selection is performed by obtaining the 200 ns window in the hit PMT time distribution that contains the maximum number of hit tubes. This is illustrated in Figure 4.1. Times t_1 and t_4 denote the start and end times of the event, respectively, while times t_2 and t_3 define the 200 ns window containing the maximum number (N_{200}) of hits. An estimate of the number of noise hits (N_{noise}) in the 200 ns window is obtained using hits from outside this time window. The significance ($\frac{N_{200}-N_{noise}}{\sqrt{N_{noise}}}$) is calculated for the selected time window. A series of progressively smaller time windows are tried, and the set of hits from the time window with the maximum significance is selected for the fit.

The vertex is found by searching a grid of fixed vertex locations and finding the grid point that has the largest goodness of fit (gof) value:

$$\text{goodness of fit (gof)} = \frac{1}{N_{sel}} \sum_{i=1}^{N_{sel}} \exp\left(\frac{-t_{res}^2}{2\sigma_t^2}\right) \quad (4.1)$$

where N_{sel} is the number of selected PMT hits, t_{res} is the residual time of each hit PMT, and σ_t is the measured PMT timing resolution, which is taken to be 5 ns here. The grid points used in this search are shown in Figure 4.2,

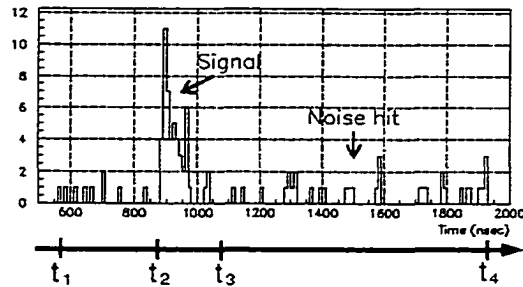


Figure 4.1: Timing distribution of hit PMTs in a typical solar neutrino candidate event[36]. Times are defined in text.

and fill the entire detector volume. After a best fit location on this rough grid is found, a fine grid about the best fit point is created, and the fit procedure repeated until a best fit point is obtained. The gof value obtained from the best fit point has a value between 0 (bad fit) and 1 (perfect fit) and is used as a measure of the fit quality. Additional details of the vertex reconstruction algorithm can be obtained in References [27, 31].

The vertex resolutions of this reconstruction algorithm are measured using the LINAC calibration system. Table 3.1 contains the averaged vertex resolution for each LINAC beam energy. A vertex resolution of ~ 73 cm is found for 10 MeV electrons.

4.2 Direction Reconstruction

Once a vertex location in the SK detector has been determined, the direction of travel for the electron is reconstructed based on the conical pattern of the emitted Cherenkov light. A maximum likelihood function is used to determine the reconstructed direction about the vertex position. The likelihood

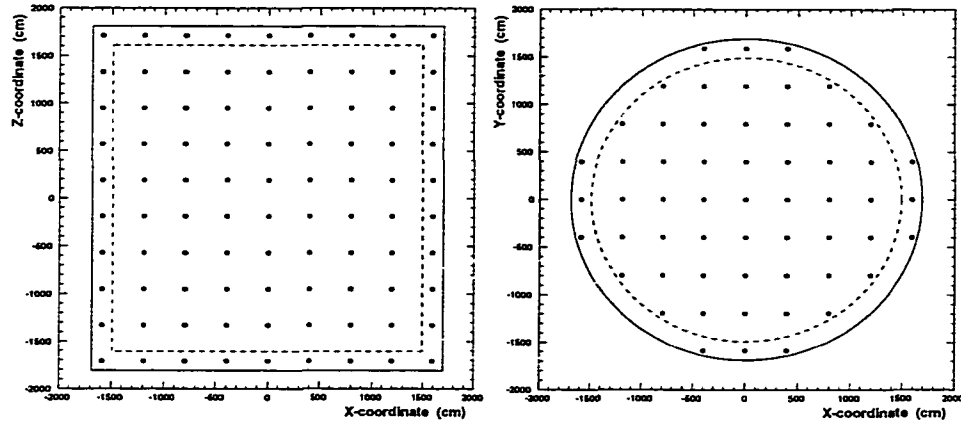


Figure 4.2: Grid point locations used by vertex fitter. Solid lines denote the boundaries of the inner detector, and dashed lines indicate the fiducial volume boundary.

function used is:

$$L(dir) = \sum_i \log(f(\cos \theta_{dir}))_i \times \frac{\cos \theta_i}{a(\theta_i)}. \quad (4.2)$$

$\cos \theta_{dir}$ is the opening angle between a trial direction and the vector connecting the vertex position to the i^{th} hit PMT location. The function $f(\cos \theta_{dir})$ is the relative probability distribution that a photon will be emitted at a given angle relative to the direction of travel. This distribution, shown in Figure 4.3, is generated using a MC simulation of 10 MeV electrons using the known input electron direction and location of all hit PMTs relative to this direction. This distribution peaks at 42° , with broad tails caused by multiple Coulomb scattering of the electron and scattering of Cherenkov light in the water. $\cos \theta_i$ is the angle between a vector normal to PMT tube face and the vector connecting the vertex position to the i^{th} hit PMT location. The function $a(\theta_i)$ is a correction factor for the acceptance of the PMT photocathode as a function of incident angle, and is also shown in Figure 4.3.

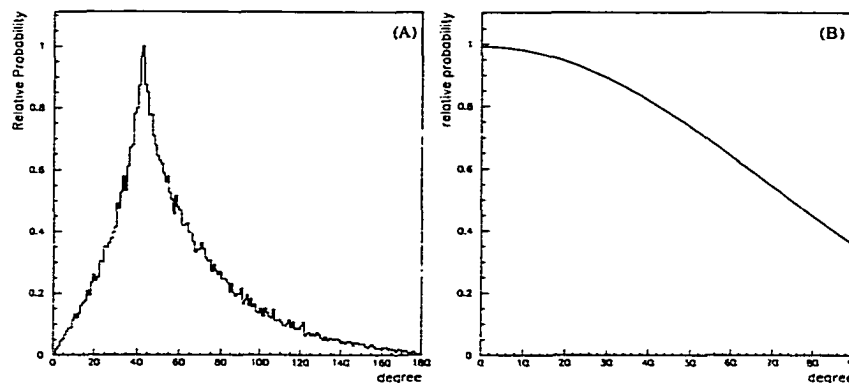


Figure 4.3: (A) $f(\cos \theta_{dir})$ relative probability distribution used by the direction likelihood fitter. (B) The angular acceptance correction used for the PMTs as a function of incident angle[31].

The direction of travel for an electron is determined by varying the trial direction in a series of successively smaller steps until the direction with the largest likelihood value is found. This direction is taken as the reconstructed travel direction for the electron. The angular resolution of this direction fit is measured using the LINAC calibration system (see Section 3.3).

The angular resolution of this direction reconstruction algorithm is measured using the LINAC calibration system, which has a known, downward-directed, input direction. Table 3.1 contains the averaged angular resolution for each LINAC beam energy. An angular resolution of $\sim 25^\circ$ is found for 10 MeV electrons.

4.3 N_{eff} and Energy Reconstruction

Once a vertex and direction are determined, the energy of the electron must be reconstructed. Since roughly 6 photoelectrons are collected per MeV of energy, events in the energy range of interest for the solar neutrino

analysis (5-20 MeV) will have very few PMTs that register more than a single photo-electron. Therefore, the number of hit tubes is used as the primary measure of energy. This procedure avoids the difficulties associated with the poor charge resolution of PMTs near the single photon level, as well as small changes in the collected charge from electronic noise.

The number of hits, N_{hit} , is determined by taking all hits that fall within a 50 ns window in timing residuals calculated using the reconstructed vertex location. This timing cut reduces the contribution from noise hits to the reconstructed energy. The N_{hit} value is then corrected for known detector and position dependent effects to obtain an effective number of hits, N_{eff} . These include corrections for light attenuation in the water, PMT dark noise, multiple photoelectrons, and geometrical acceptance of the PMTs, among others. The N_{eff} value is defined by:

$$N_{eff} = \sum_{i=1}^{N_{hit}} [(X_i + \epsilon_{tail} - \epsilon_{dark}) \times \frac{N_{all}}{N_{oper}} \times S(\theta_i, \phi_i) \times \exp(\frac{r_i}{\lambda(run)}) \times G_{kek}(i)] \quad (4.3)$$

where:

- X_i is the expected number of photoelectrons in a hit channel and is based on the occupancy of the nearest neighbor PMTs. This number is calculated based on ratio ($x_i = \frac{n_i}{N_i}$) of the number of hit neighbor tubes (n_i) in the 3×3 tube patch to the number of alive neighbor tubes that could have been hit (N_i). The value of X_i is then determined, based on Poisson statistics and the assumption of a uniform light level over this 3×3 tube patch, to be:

$$X_i = \begin{cases} \frac{\ln[(1-x_i)^{-1}]}{x_i} & x_i < 1 \\ 3.0 & x_i = 1 \end{cases} \quad (4.4)$$

This average number of photoelectrons per hit PMT is shown in Figure 4.4 as a function of the number of hit tubes in the 3×3 tube patch centered about the considered hit tube. The value at $x_i = 1.0$ is determined by extrapolation.

- ϵ_{tail} is a correction for reflected light that is outside the 50 ns time residual window. The number of hits in a 100 ns time residual window is determined (N_{100}) and the correction is taken as:

$$\epsilon_{tail} = \frac{N_{100} - N_{50}}{N_{50}} \quad (4.5)$$

- ϵ_{dark} is a correction for dark noise hits collected during the 50 ns time window. This correction is:

$$\epsilon_{dark} = \frac{N_{alive} \cdot R_{dark} \cdot 50ns}{N_{50}} \quad (4.6)$$

where N_{alive} is the number of alive tubes, and R_{dark} is the measured average dark noise rate for the current run.

- $\frac{N_{all}}{N_{oper}}$ is a correction to account for dead PMTs as a function of time where N_{all} is the total number of PMTs in the SK detector (11,146) and N_{oper} is the number of PMTs operational during the current run.
- $S(\theta_i, \phi_i)$ is the effective photocathode area of each hit PMT as a function of the photon arrival directions, θ_i and ϕ_i . The ϕ asymmetry is caused by shadowing of nearest neighbor tubes at large values of θ .

- $\exp(\frac{r_i}{\lambda(run)})$ is a correction for light attenuation as the photons travel a distance r_i from the vertex position to the hit tube location. The relative water transparency, $\lambda(run)$, is measured weekly using the decay electrons of stopped muons (see Section 3.2.2).
- $G_{kek}(i)$ is a quantum efficiency correction factor. 375 PMTs were manufactured prior to the main set of PMTs, and these tubes are found to have slightly higher quantum efficiencies. These “KEK” tubes are penalized appropriately:

$$G_{kek}(i) = \begin{cases} 0.833 & \text{for the 375 KEK PMTs} \\ 1.00 & \text{all other PMTs} \end{cases} \quad (4.7)$$

The value of N_{eff} has been designed to remove all position, detector and water transparency related effects and return a uniform value over the entire fiducial volume and in all detector run periods.

The obtained value of N_{eff} is closely related to the visible energy deposited by the electron before it went below the Cherenkov threshold. However, in this analysis, the total electron energy is used instead of visible energy, and includes corrections for the energy deposited below Cherenkov threshold and for the electron rest mass. The N_{eff} to total energy translation function is obtained during a special MC simulation of mono-energetic electrons performed with the LINAC-tuned detector simulation. The reconstructed total energy as a function of N_{eff} is shown in Figure 4.5.

4.4 Muon Reconstruction

Muons pass through the SK detector at a rate of about 2 Hz. As these high energy particles pass through the detector, they will occasionally interact with a ^{16}O nucleus and create radioactive spallation products. These

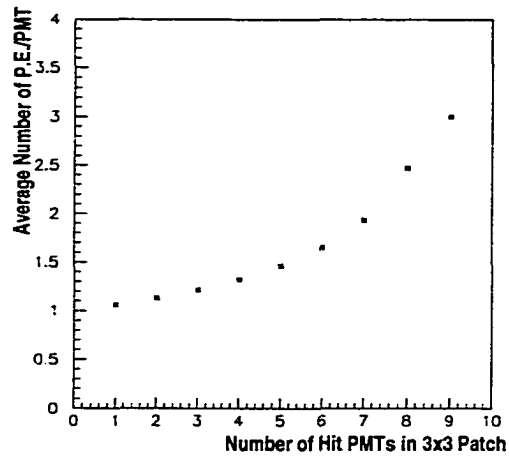


Figure 4.4: Average number of photoelectrons per hit tube as a function of the number of hit tubes in the 3×3 tube patch containing the hit tube.

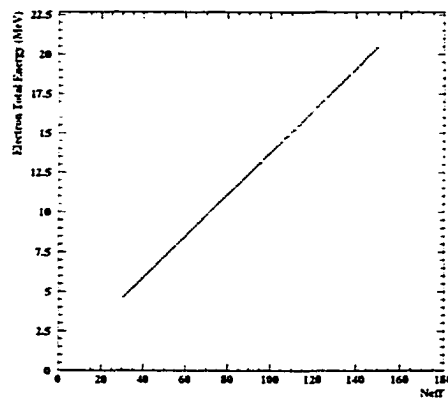


Figure 4.5: Reconstructed total electron energy as a function of the reconstructed N_{eff} value.

spallation products often have a decay which can mimic solar neutrino events, and are the dominate background for solar neutrinos above ~ 6 MeV. These decays do have strong temporal and spatial correlations to the path of the parent muon in the detector. In order to reduce this background, all muons found in SK are fit with a muon track fitter, which determines the entry and exit points, as well as the track, or path, of the muon through the detector. This fit is later used in a likelihood analysis to remove the spallation events from the solar neutrino sample. This muon fitter also can fit multiple muons, that is more than a single muon track present in the detector at the same time, as well as muons that stop inside the detector volume and do not exit. Stopping muons can produce decay electrons, or, if it is negatively charged, can be captured by a ^{16}O nucleus to create ^{16}N . ^{16}N candidates are searched for separately and are used as a source of detector calibration.

The muon fitter for the spallation analysis reconstructs muons tracks by identifying an entry point based on the earliest cluster of in-time hit tubes. The exit point is identified as being the largest cluster of high-charge tubes, since the Cherenkov ring will get progressively smaller as the muon approaches the wall. This simple reconstruction algorithm works well for $\sim 85\%$ of muons. The measured track resolution from MC simulation of cosmic ray muons is 67 cm. More precise algorithms are used for multiple muons, stopped muons and corner clipping muons, and are well described in Reference [36]. These fit results are used by the spallation likelihood analysis to identify spallation events.

4.4.1 Muboy-Stopped Muons for the ^{16}N Analysis

A separate muon fitter is used for finding stopped muons, which are a potential source of ^{16}N . The Muboy muon track fitter, written by R. Svoboda, fits all types of muons, including single through-going muons, multiple parallel muon tracks, corner-clippers (muons that just pass through a corner of the detector), and stopping muons. More details regarding this muon fitter can be obtained in Reference [28].

Muboy identifies the entry and exit point in a manner similar to the spallation muon track fitter described above. Stopping muons are identified by looking at the amount of Cherenkov light that was produced in the last 200 cm of the fitted track. If there is a deficit of Cherenkov light in this last part of the track segment, and no in-time hits are found in the OD detector, then a muon is called a stopped muon. The stop-point is then determined by finding the point along the muon track where the Cherenkov light production falls below 40% of the average light production. This point is then identified as the stop point.

This stop point is taken as the input to the ^{16}N search program. A study of these stop positions and the subsequent positions of decay electrons indicates that the fitted stopped-muon position from Muboy is 45 cm short of the true stopping muon position. In the search for ^{16}N events, the stopping muon position is shifted 45 cm farther along the muon track to account for this offset.

4.5 Other Reconstruction Tools

With the addition of SLE data, a solar neutrino sample below 6.5 MeV, additional tools are required to separate the true solar neutrino-induced

electron events from background events. New event reconstruction and analysis tools have been developed for this purpose. The two new tools used in this analysis are the “new goodness” cut and the “clusfit” vertex fitter.

4.5.1 New Goodness Cut

The new goodness cut¹ is designed to separate background events from the true electron Cherenkov ring-like events in the data sample. These background events include events that have small, tightly-spaced clusters of hit tubes, presumably originating from gamma ray activity near the PMT glass. These events are often reconstructed inside the fiducial volume, as the PMT hits are very close in time and space, and the collected hit information has little power to differentiate widely separated vertex positions. True events from an electron in the fiducial volume will have PMT hits with a noticeable separation in time and space, and only the true vertex will return a good fit.

The new goodness cut takes advantage of these fundamental differences between background and electron events. For this cut, goodness of fit (gof) values (same definition as in Section 4.1) are calculated on a 10m×10m grid perpendicular to the fitted direction of the event, as illustrated in Figure 4.6. The goodness fraction is then calculated:

$$\text{goodfrac} = \frac{\text{Number of grid points with } GDN_i > (GDN_0 - 0.2)}{\text{Total number of grid points}} \quad (4.8)$$

where GDN_i are the gof values calculated at each grid point, and GDN_0 is the gof value calculated at the original reconstructed vertex. If this fraction

¹The new goodness cut developed by Y. Fukuda.

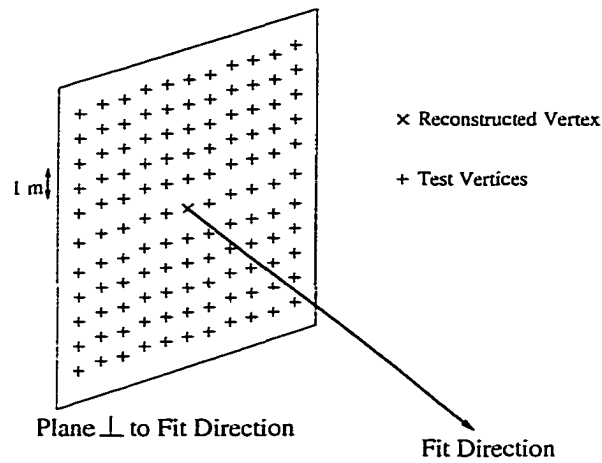


Figure 4.6: Definition of grid points used by the new goodness cut.

exceeds a cut value (set to 20%), then the event is labeled as a background and removed.

A distribution of the goodfrac parameter for a sample of real data from the solar neutrino reduction and for a sample of ^8B MC events is presented in Figure 4.7. This cut removes $\sim 50\%$ of the data sample, while preserving $> 90\%$ of the MC sample.

4.5.2 Clusfit

The clusfit algorithm² is another vertex reconstruction algorithm, with a hit selection routine that is different from the original vertex fitter. By using a different hit selection algorithm, non-physical background events are given another chance to be fit near the wall, where a fiducial volume cut based on this second vertex would remove them. Good electron events in the fiducial volume are most likely reconstructed at the same location, and another separation between signal and background is achieved.

²Clusfit developed by M. Smy.

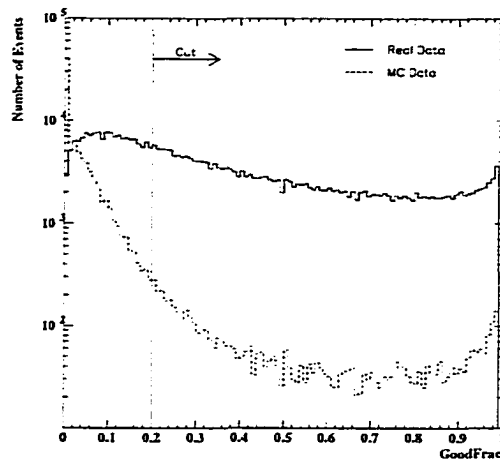


Figure 4.7: The goodfrac distribution from the new goodness cut for a sample of real data and MC ^8B data. The cut at 0.2 is shown as well. Please note that this is a log plot.

The hit selection procedure is carried out in a manner similar to the Hayai vertex fitter (see Section 2.7.2). First a causality cut is performed on the hits. Hits that can be paired with any other hit in the event within 1250 cm in space and 35 ns in time of each other are saved as a selected hit. Next, hits are again paired with each other, this time with the requirement that pairs satisfy a triangle relation, as illustrated in Figure 4.8. This simply states that for a pair of hits to originate from a physical vertex, the spatial distance between two hit tubes (ΔR) must be greater than the time difference between the tube hits (Δt). If this is true, then the hit pair is said to be correlated. From this set of correlated pairs, the largest set of mutually correlated hits is selected and used by the grid fit.

The grid fit works in a manner similar to the original vertex reconstruction algorithm, with a slightly modified grid. The grid locations to be searched are

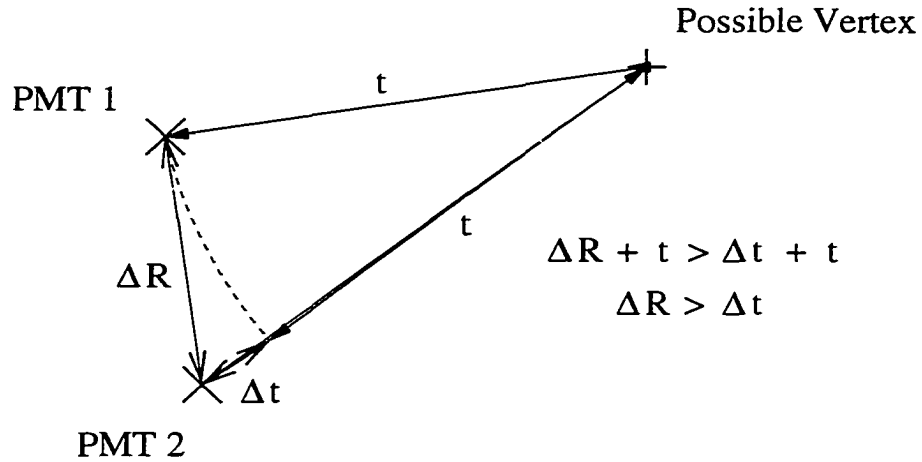


Figure 4.8: Triangle relation between pairs of hit PMTs. A pair of hit tubes must satisfy the relation $\Delta R > \Delta t$ to be considered a correlated pair. PMT hit times are expressed as distances under the assumption of a constant 21.6 cm/ns light speed.

arranged in a cylindrically symmetric pattern providing more possible vertex reconstruction positions in the region outside the fiducial volume. A series of finer grids are used around the best fit grid point until a final reconstructed vertex position is found.

Figure 4.9 shows the original and the clusfit reconstructed vertex distributions in r and z for a set of real data events from the sample of solar neutrino candidates, as well as for a sample of ^8B MC data. Both of these data samples are shown after a 2 m fiducial volume cut on the original reconstructed vertex has been performed. For the real data sample, roughly 25% of the events that originally reconstructed inside the fiducial volume, have clusfit vertices outside the fiducial volume and can be removed from the data sample. The MC data sample has $> 95\%$ of the data sample still reconstructed inside the fiducial volume.

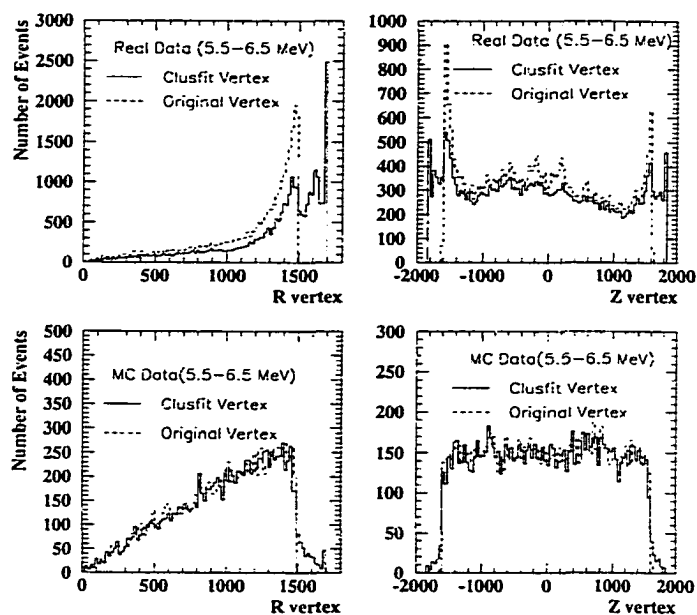


Figure 4.9: The original and clusfit vertex distributions for events with energies between 5.5 and 6.5 MeV for a sample of real data and a sample from the ^8B MC data. A second fiducial volume cut based on the clusfit vertex to remove background in this energy range.

The new goodness cut and the clusfit algorithm are used in the data reduction (see Chapter 6) to reduce the background levels below 6.5 MeV by more than 50%.

CHAPTER 5

NEUTRINO SIMULATIONS

Super-Kamiokande does not directly measure the flux of solar neutrinos. SK is only capable of measuring the rate of neutrino-scattered electrons above a set energy threshold. In order to turn this number into a flux of solar neutrinos, a MC simulation of the theoretically modeled flux must be performed. First, the rate and spectrum of scattered electrons must be calculated from the modeled neutrino flux and cross sections for neutrino-electron scattering. These scattered electrons must then be input into the SK detector simulation, which simulates secondary electron interactions, Cherenkov light generation, and PMT responses to produce simulated data. These simulated data are then subjected to the same reconstruction and reduction as the real data. A comparison of the measured event rates between data and MC is used to find the measured flux.

5.1 Neutrino Interaction Simulation

Solar neutrinos are detected in SK by the elastic scatter of electrons:

$$\nu + e \rightarrow \nu' + e'.$$

This analysis uses the Bahcall-Pinsonneault 1998 (BP98) solar model[11] as the source of the input neutrino spectrum. The modeled ^8B neutrino flux of $5.15 \times 10^6 \text{ cm}^{-2} \text{ s}^{-1}$ (see Section 1.1) is used as a convenient normalization for the simulation.

Super-Kamiokande is sensitive to both ^8B and hep solar neutrinos. The hep contribution is expected to be $\sim 1,000$ times smaller than the expected

^8B contribution. This section details the modeling of scattered electrons based on the theoretically modeled ^8B neutrino spectral shape. The hep neutrinos are not directly discussed, but the procedures are similar for hep, with the appropriate modeled spectral shape used, and the hep simulation is performed for completeness.

5.1.1 Neutrino-Electron Cross Section

The interaction of a neutrino with an electron in the SK detector occurs by the weak force, and the cross sections for these reactions are typically very small. The neutrino-electron differential scattering cross section is taken from in Reference [38], and is given by:

$$\begin{aligned} \frac{d\sigma(E_\nu)}{dT} = & \frac{2G_F^2 m (\hbar c)^2}{\pi} \{ g_L^2(T) [1 + \frac{\alpha}{\pi} f_-(z)] + \\ & g_R^2(T) (1-z)^2 [1 + \frac{\alpha}{\pi} f_+(z)] - \\ & g_R(T) g_L(T) \frac{m}{E_\nu} z [1 + \frac{\alpha}{\pi} f_{+-}(z)] \} \end{aligned} \quad (5.1)$$

where:

$$E_\nu = \text{Energy of neutrino (MeV)}$$

$$T = \text{Recoil electron kinetic energy (MeV)}$$

$$z = \frac{T}{E_\nu}$$

$$G_F = \text{Fermi coupling constant[2]}$$

$$= (1.16639 \pm 0.00001) \times 10^{-11} \text{MeV}^{-2}$$

$$m = \text{Electron mass[2]}$$

$$= 0.510999 \text{MeV}$$

$$g_L^{(\nu_e, e)}(T) = \rho_{NC}^{(\nu_e, e)} \left[\frac{1}{2} - \kappa^{(\nu_e, e)}(T) \sin^2(\theta_W) \right] - 1$$

$$g_R^{(\nu_e, e)}(T) = -\rho_{NC}^{(\nu_e, e)} \kappa^{(\nu_e, e)}(T) \sin^2(\theta_W)$$

$$\begin{aligned}
g_L^{(\nu_\mu, e)}(T) &= \rho_{NC}^{(\nu, e)} \left[\frac{1}{2} - \kappa^{(\nu_\mu, e)}(T) \sin^2(\theta_W) \right] \\
g_R^{(\nu_\mu, e)}(T) &= -\rho_{NC}^{(\nu, e)} \kappa^{(\nu_\mu, e)}(T) \sin^2(\theta_W) \\
\rho_{NC}^{(\nu, e)} &= 1.0126 \pm 0.0016 \\
\kappa^{(\nu_e, e)}(T) &= 0.9791 + 0.0097I(T) \pm 0.0025 \\
I(T) &= \frac{1}{6} \left\{ \frac{1}{3} + (3 - x^2) \left[\frac{1}{2} \ln\left(\frac{x+1}{x-1}\right) - 1 \right] \right\} \\
x &= \sqrt{1 + \frac{2m}{T}} \\
\kappa^{(\nu_\mu, e)}(T) &= 0.9970 - 0.00037I(T) \pm 0.0025 \\
\sin^2(\theta_W) &= 0.2317
\end{aligned}$$

Eqn. 5.1 includes terms to incorporate QED (Quantum Electrodynamic) effects, and radiative corrections. The functions f_+ , f_- , and f_{+-} are used to include the QED corrections and are also taken from Reference [38]. The two forms of the functions g_L and g_R are included here for (ν_e, e) and (ν_μ, e) scattering. In the absence of neutrino oscillations, only the (ν_e, e) form is used and includes contributions from charged current (CC) and neutral current (NC) interactions in the cross section. The (ν_μ, e) represents only NC component of the scattering cross section. Non-electron, active neutrinos (ν_μ or ν_τ) will only interact by the NC reaction with electrons. For the standard simulation of ^8B neutrinos, only (ν_e, e) are considered, but (ν_μ, e) will be included for simulations that include neutrino oscillations.

As the interaction of a neutrino and an electron is a 2-body process, the reaction kinematics are relatively simple. A neutrino of energy E_ν can produce a maximum electron recoil kinetic energy of:

$$T_{max} = \frac{2E_\nu^2}{2E_\nu + m} \quad (5.2)$$

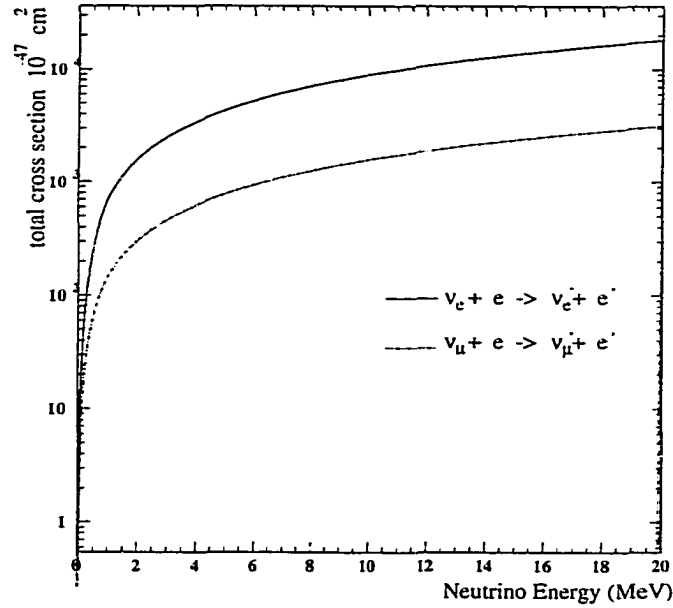


Figure 5.1: Total cross section for neutrino-electron scattering as a function of neutrino energy. The total cross sections for both (ν_e, e) and (ν_μ, e) are presented.

by the conservation of energy and momentum. To calculate the total cross section for a neutrino energy E_ν , the differential cross section is numerically integrated from zero to T_{max} . The total neutrino-electron scattering cross section as a function of neutrino energy is presented in Figure 5.1, showing the cross section for (ν_e, e) and (ν_μ, e) . These numbers are in excellent agreement with the tabulated cross section values published in Reference [38].

5.1.2 Creating ^8B Scattered Electrons

In order to perform the detector simulation of solar neutrino events in SK, neutrino energies must be selected from the ^8B neutrino spectra, the kinetic energy of the recoil electron must be chosen, and the rate of scattered electrons must be normalized to the incident neutrino flux.

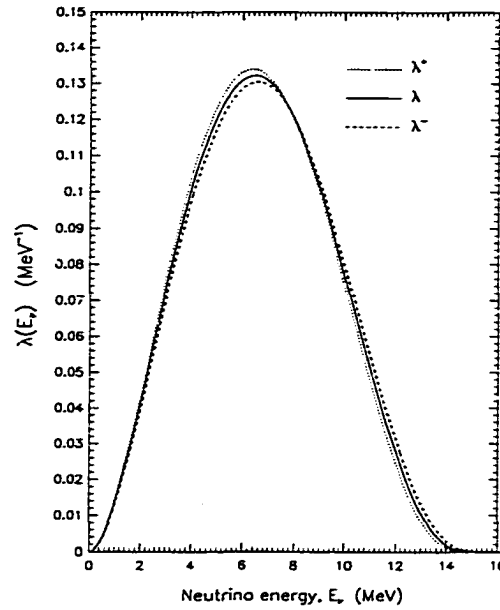


Figure 5.2: The best estimate ${}^8\text{B}$ neutrino energy spectral shape ($\lambda(E)$) with the $\pm 3\sigma$ maximum theoretical and experimental uncertainties (λ^+ and λ^-).

The best estimate neutrino spectral shape ($\lambda(E_\nu)$) from the BP98 solar model is shown in Figure 5.2[37]. Also shown are the $\pm 3\sigma$ combined theoretical and experimental uncertainties in the spectral shape (λ^+ and λ^-). This spectrum is derived from terrestrial measurements of the beta spectrum from ${}^8\text{B}$ decay. The primary source of these errors is the experimental uncertainty in the measurement of the intermediate ${}^8\text{Be}^*$ state, which leads to an uncertainty in the inferred neutrino energy. The temperatures in the center of the Sun are not high enough to significantly affect the neutrino spectral shape.

The product $\sigma(E_\nu) \cdot \lambda(E_\nu)$ provides the relative probability that a neutrino of energy E_ν will interact by scattering an electron in the SK detector. The $\sigma(E_\nu) \cdot \lambda(E_\nu)$ distribution is presented in Figure 5.3. Neutrino energies to be used in the detector simulation are randomly chosen from this distribution.

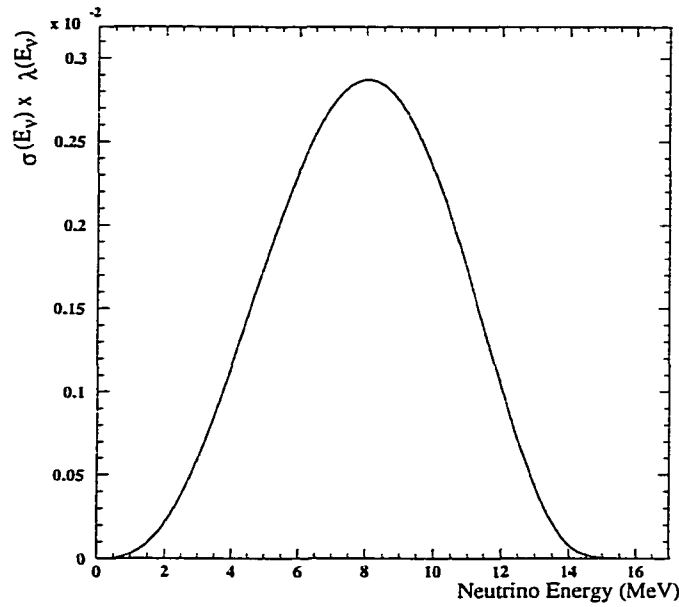


Figure 5.3: The $\sigma(E_\nu) \cdot \lambda(E_\nu)$ distribution for the ^8B spectrum and (ν_e, e) cross section. This distribution is used to choose an input neutrino energy.

Once a neutrino energy is selected from Figure 5.3, the recoil electron kinetic energy must be chosen. For a fixed neutrino energy, E_ν , the electron kinetic energy is chosen from the normalized differential cross section distribution, $\frac{d\sigma(E_\nu)}{dT}$. Figure 5.4 shows the $\frac{d\sigma(E_\nu)}{dT}$ distribution for a 12 MeV neutrino energy. For every 12 MeV neutrino scattered in the SK solar neutrino simulation, the electron kinetic energy is chosen from this distribution. It is interesting to note that a 1 MeV electron is somewhat more likely than a 10 MeV electron.

If the process of choosing a neutrino energy, followed by a recoil electron kinetic energy, is repeated 10 million times, the kinetic energy distribution for elastically scattered electrons is generated. The kinetic energy distribution of ^8B neutrino scattered electrons is presented in Figure 5.5. Even though

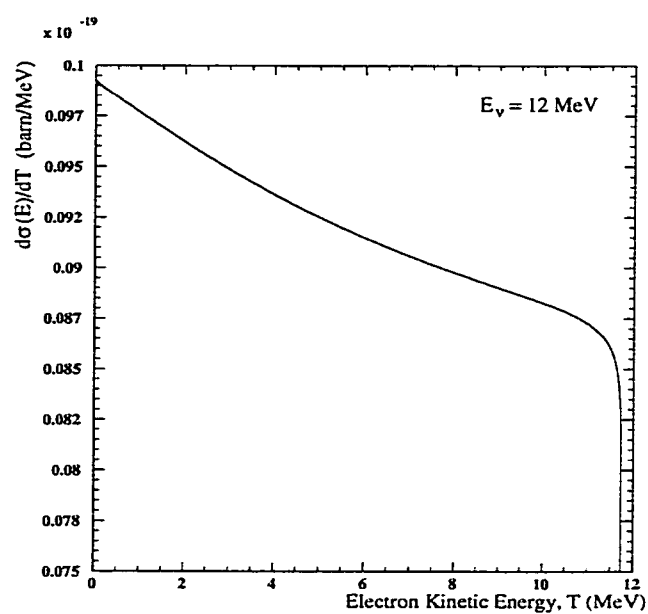


Figure 5.4: The $\frac{d\sigma(E_\nu)}{dT}$ distribution for a 12 MeV neutrino. Recoil kinetic energies for electrons from 12 MeV neutrinos are chosen from this distribution. Note that this plot is zero suppressed.

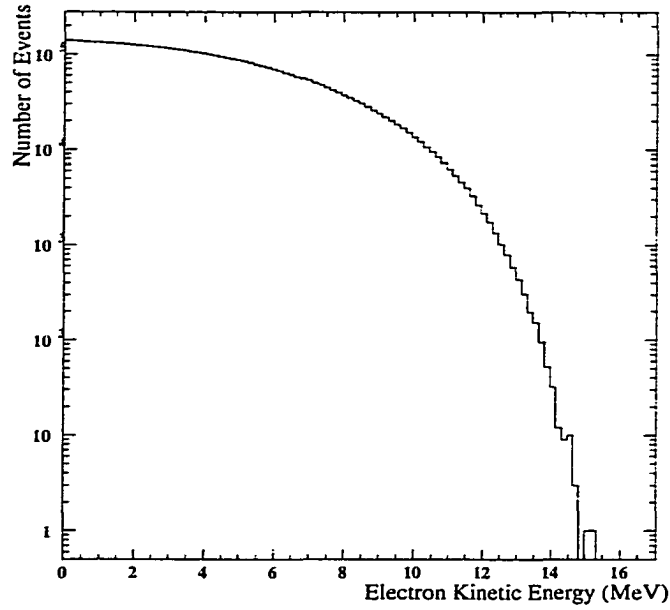


Figure 5.5: The kinetic energy distribution of ^8B neutrino scattered electrons. This is the spectrum of electrons that is input to the detector simulation.

an ~ 8 MeV neutrino is the most likely to be scattered in the detector (see Figure 5.3,) the favored production of low kinetic energy electrons (as shown in Figure 5.4) generates a falling spectrum of recoil electrons, and the peak at ~ 8 MeV is completely washed out.

5.1.2.1 ^8B Flux Normalization

The rate of scattered electrons is used as an overall normalization of the number of MC events generated. The normalization is obtained using the input flux normalization, spectral shape and cross section for (ν_e, e) scattering and numerically integrating:

$$\begin{aligned}
 N_{s_B} &= N_e N^{^8B-BP98} \int_0^\infty \sigma(E_\nu) \lambda(E_\nu) dE_\nu \\
 &= 287.6 \text{ Recoil electrons per day}
 \end{aligned} \tag{5.3}$$

where:

$$\begin{aligned}
 N_e &= \text{Number of electrons in the SK inner detector} \\
 &= 1.081 \times 10^{34} \text{ electrons} \\
 N^{8B-BP98} &= \text{Flux normalization from the BP98 solar model[11]} \\
 &= 5.15 \times 10^6 \text{ cm}^{-2} \text{ s}^{-1}
 \end{aligned}$$

Note that this is the number of scattered electrons at all energies (0~15 MeV) and is used to normalize the input to the detector simulation. The expected measured rate is obtained after the detector simulation is completed and all steps of the reduction are applied to the simulated data.

5.1.2.2 Hep Flux Normalization

The hep flux normalization is obtained in a manner similar to the ^8B flux normalization:

$$\begin{aligned}
 N_{HEP} &= N_e N^{HEP-BP98} \int_0^\infty \sigma(E_\nu) \lambda(E_\nu)^{HEP} dE_\nu \\
 &= 0.170 \text{ Recoil electrons per day}
 \end{aligned} \tag{5.4}$$

where:

$$\begin{aligned}
 N^{HEP-BP98} &= \text{Hep flux normalization from the BP98 solar model[11]} \\
 &= 2.10 \times 10^3 \text{ cm}^{-2} \text{ s}^{-1} \\
 \lambda(E_\nu)^{HEP} &= \text{Hep neutrino energy spectral shape[39]}
 \end{aligned}$$

5.2 Detector Simulation

Once a neutrino energy and an electron kinetic energy are chosen, the information is input into the SK detector simulation. This simulation tracks the electrons as they move and interact in the simulated detector, generates

and tracks Cherenkov photons from the electron, and simulates the response of PMTs and electronics to create a simulated event.

The detector simulation used is based on Geant 3.21, a particle interaction simulation from CERN[32]. This package is capable of simulating electro-magnetic interactions between 10 keV and 10 TeV. For electrons, this simulation package models multiple Coulomb scattering, Cherenkov light generation, δ -ray generation, and Bremsstrahlung photon creation. The propagation, scattering and absorption of Cherenkov photons are also included. Compton scattering and pair-production are included for higher energy photons.

Most parameters in the MC detector simulation are tuned to match observed or theoretically expected values. The response of the PMT and electronics are tuned to reproduce the measured signals from the detector. Reflectivity of surfaces in the detector (PMT glass, black sheet, etc.) are modeled to match measured values. To properly set the response of the MC simulation, the PMT timing resolution, the scattering to absorption ratio of the water and the PMT collection efficiency are tuned to match calibration data from the detector.

The PMT timing resolution for single photoelectrons is tuned using the measured vertex resolution from the LINAC calibration. The MC timing resolution is tuned until the resulting MC vertex resolution reproduces the value from the LINAC calibration data (see Section 3.3). The PMT timing resolution values measured in the manner are in good agreement with the previously measured laboratory values[40].

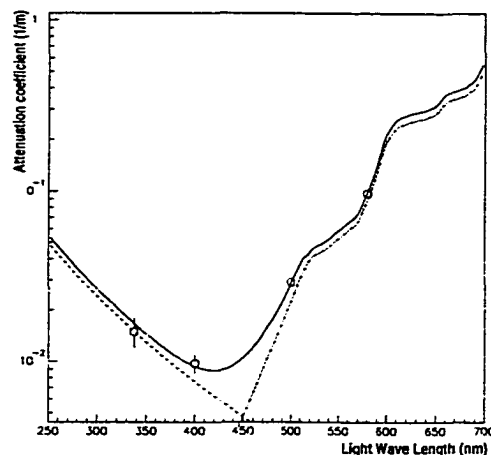


Figure 5.6: The tuned attenuation coefficient (attenuation length) $^{-1}$ as a function of wavelength (solid line). The two theoretical components (dashed = scattering and dot-dashed = absorption) are also shown. The measured values of the attenuation length are shown as open circles, and agree well with the modeled attenuation length.

The scattering to absorption ratio for Cherenkov photons is also tuned from calibration data. The overall light attenuation of the water is measured directly (see Section 3.2.1), but the ratio of scattering to absorption is not directly measured. At wavelengths shorter than ~ 400 nm, Raleigh scattering is expected to be the dominant component for light attenuation. At wavelengths longer than ~ 430 nm, absorption begins to dominate the light attenuation. The ratio of these two components is tuned so that the measured positional dependence of the LINAC data and MC simulation agree. The MC curve for light attenuation is shown in Figure 5.6. The measured attenuation lengths are in good agreement with the tuned attenuation length as a function of wavelength.

The PMT collection efficiency is the final parameter tuned. This parameter is adjusted to equalize the energy scales between LINAC data and MC

simulation. The value of 78% chosen here is in agreement with the previously measured mean collection efficiency of 70%[40].

5.2.1 Simulation Input

Since the distance to the Sun is a function of the time of year, solar neutrino events are generated to match the livetime distribution of the detector. The number of dead PMTs and the relative water transparency are also input into the detector simulation to generate MC data that reproduces the actual data as closely as possible. To prevent the statistical error of the MC calculation from limiting the accuracy of measurements, 50 times the expected number of recoil electrons are generated and input to the MC simulation.

For each live minute simulated, the known position of the sun is used to obtain the neutrino input direction, and a random location in the ID of the SK detector is chosen as an input vertex. The recoil electron direction is generated using the chosen recoil kinetic energy and the input neutrino energy according to:

$$\cos \theta_{scatter} = \frac{1 + \frac{m}{E_\nu}}{\sqrt{1 + \frac{2m}{T}}} \quad (5.5)$$

This is illustrated in Figure 5.7, where $\cos \theta_{scatter}$ is defined as the angle between the direction of the incident neutrino and the direction of the scattered electron. The angle $\phi_{scatter}$ is randomly chosen.

5.2.2 Simulation Output

The SK detector simulation outputs data in the same format as real data, so that the same reconstruction (see Chapter 4) and reduction (see Chapter 6) algorithms are easily applied. Additionally, a trigger simulation routine is applied to the simulated data. For the LE trigger level (see Section 2.6.3),

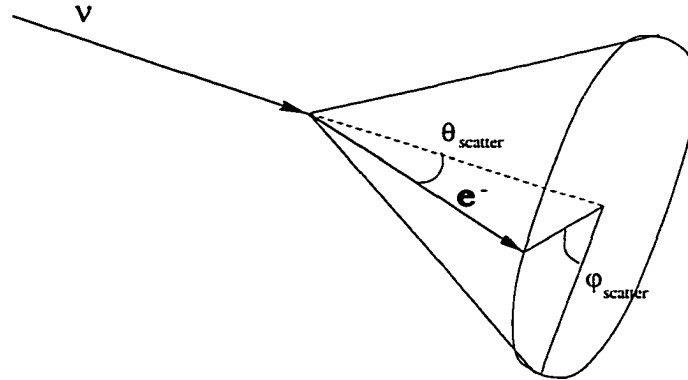


Figure 5.7: Schematic diagram of neutrino electron scattering. This interaction defines the angle $\cos \theta_{scatter}$.

this trigger simulation reproduces the hardware trigger setup by generating simulated hitsum pulses for each hit PMT. When the sum of these simulated hitsum pulses exceeds a threshold, a simulated LE trigger is assigned. The threshold is tuned so that the trigger efficiencies of data and MC agree. For the SLE trigger threshold, 3 separate tuned trigger thresholds are considered (SLE1, SLE2, and SLE3 as described in Section 2.6.3) and an off-line reproduction of the online SLE software reconstruction is implemented. Only SLE events that pass the appropriate trigger simulation and the online reduction simulation are considered for the MC analysis.

After the reconstruction and reduction are completed, the MC event rate is determined by normalizing the number of events remaining by the appropriate flux normalization (from Section 5.1.2.1). The expected event rate for the energy range of 5.5-20.0 MeV is found to be 33.92 events/day/22.5 kton for the ^8B flux and 0.034 events/day/22.5 kton for the hep flux. Therefore the total expected event rate for the BP98 solar model is found to be

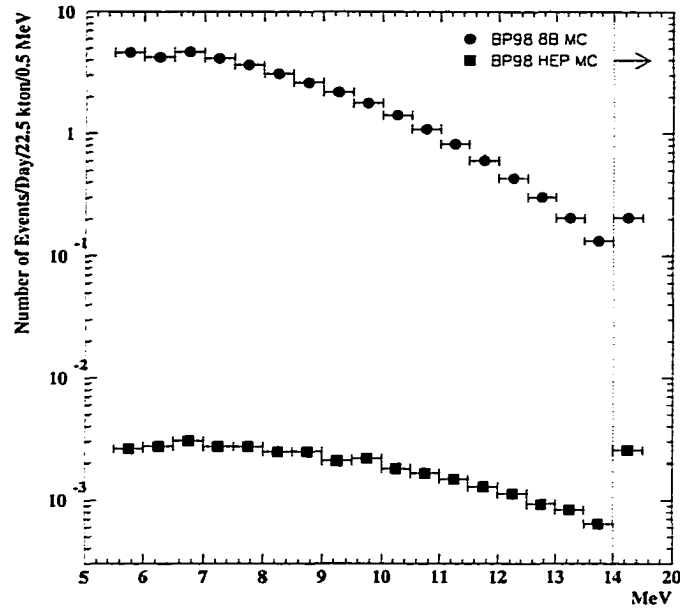


Figure 5.8: Event rate as a function of energy for the ^8B and hep MC samples. The last bin contains all events between 14.0-20.0 MeV.

33.95 events/day/22.5kton. The event rate for these final MC samples as a function of energy is presented in Figure 5.8. For each event in the MC sample, the $\cos \theta_{sun}$, which is the cosine of the angle between the reconstructed electron direction and the input neutrino direction, is also determined. The $\cos \theta_{sun}$ distribution for the ^8B MC sample is presented in Figure 5.9. The strong forward-peaking of this distribution will be used to extract the solar neutrinos from the actual data.

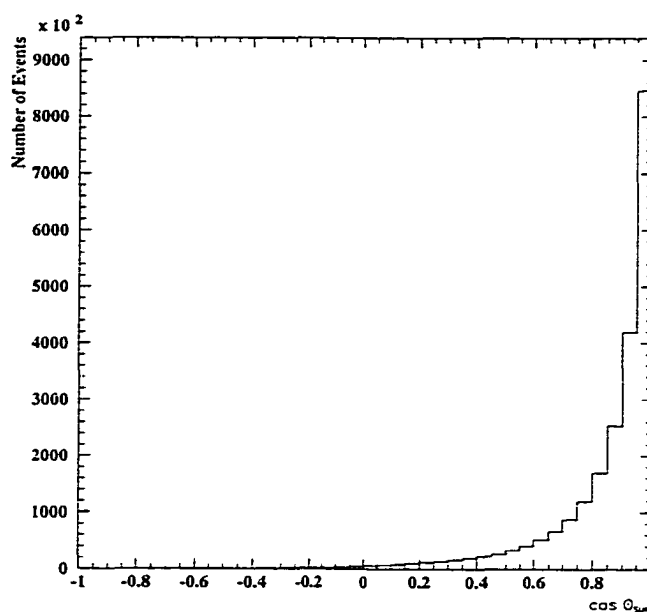


Figure 5.9: $\cos \theta_{sun}$ distribution for the ^8B MC sample. $\cos \theta_{sun} = 1.0$ corresponds to events that are coming directly from the direction of the sun.

CHAPTER 6

DATA REDUCTION

Super-Kamiokande began taking data on April 1, 1996. The first two months of data were removed from the solar neutrino analysis, as the water quality was initially inadequate for an effective solar neutrino search. The data used for this analysis were collected at Super-Kamiokande between May 31, 1996 and October 28, 1999. During this period, 980.4 live days of good data were collected, for a duty cycle of 79%.

Data are collected in runs. Each run is limited to a maximum length of 24 hours to limit recorded file sizes, and a new run is started anytime the detector configuration is changed. The data used in this analysis covers SK run numbers 1742 to 8058. Each run is further divided into sub-runs, each lasting 5-10 minutes depending on the trigger rate.

Each run and sub-run collected are evaluated based on the length of the run/sub-run, as well as measured rates of known backgrounds, and labeled as good or bad. The criteria for good run/sub-run selection is:

- The run must be longer than 5 minutes in length. Runs stopped with less than 5 minutes of running time are usually indicative of a problem with the data acquisition system.
- Each sub-run must be longer than 30 seconds. A short sub-run usually occurs at the end of a run, and can contain incomplete events.

- The rate of events identified as originating from flashing PMTS, events identified as electronic noise, or events with incomplete PMT data must not exceed set thresholds. If any of these event rates are high, this is usually a sign of a detector problem and the run or sub-run is removed.

Data from the SK detector are collected at a rate of 10-20 Hz, depending on the SLE trigger threshold (see Section 2.7). For the 980 live days analyzed here, the data sample contains 1.1×10^9 events. The expected rate from the BP98 solar model (33.9 events/day) is $\sim 33,000$ solar neutrino events with recoil electron energies above 5.5 MeV. The reduction described in this chapter is used to reduce this large data set to a much smaller, final sample of solar neutrino candidates, on which the solar signal extraction can be performed.

As a check that the data reduction is not affecting the measured rate of solar neutrino interactions in the SK detector, the decay events of ^{16}N created by the capture of a μ^- on ^{16}O are used. These events occur at a rate similar to that of solar neutrino interactions, and are collected as a background to the solar neutrino analysis. The measured rate of these events is compared with the rate expected from the measured stopping muon rate and serves as an overall check of the reduction.

6.1 Reduction Steps

The data sample reduction is performed in three steps. This separation of the reduction into pieces allows for replacement of cuts in later steps of the reduction without reprocessing the entire data sample. The first reduction targets the removal of obvious backgrounds, such as flashing PMTs and

events outside the fiducial volume. The spallation cut removes radioactive decay events produced by nuclear interactions of cosmic ray muons as they pass through the SK detector. The second reduction consists of additional cuts to remove backgrounds from the sample, especially those at lower energies.

This reduction is only applied to those events which could be solar neutrinos. Events which are obvious cosmic ray muons are removed by a cut based on the total charge of the event. The total charge distribution of collected events for a typical run is shown in Figure 6.1. Those events with more than 1000 p.e. (~ 100 MeV) are assumed to be cosmic ray muons, and a muon track fitter is used to find the path of the muon through the detector for later use in the spallation cut. Only those events with less than 1000 p.e. are sent to the solar neutrino reduction. All events that were marked by the data acquisition system as incomplete or were collected during the ATM board self-calibration cycle are removed from the data sample. Also removed at this point are events containing only a periodic trigger, or veto stop/start triggers.

6.1.1 First Reduction

The first reduction is performed immediately after the data are collected to reduce the size of the intermediate reduction files written to disk. More details regarding the cuts in the first reduction can be obtained from Reference [31]. The number of events remaining after each step of the reduction is summarized in Table 6.1. This reduction comprises a set of cuts with the following descriptions:

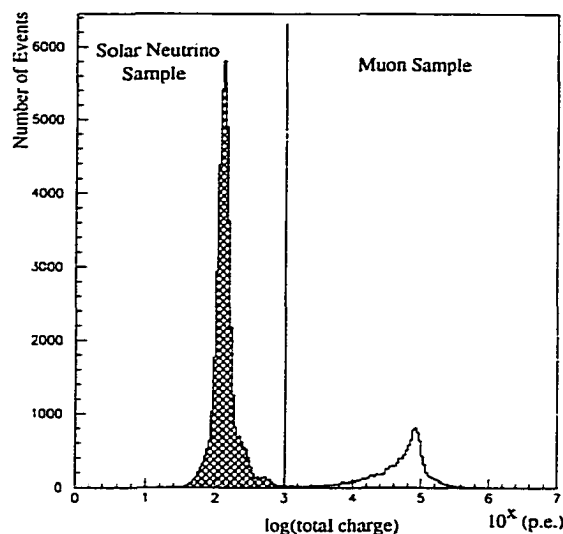


Figure 6.1: Distribution of the total charge for each event collected during a typical run at SK. Events with 1000 p.e or less are considered for the solar neutrino analysis and reduction. Events with total charge greater than 1000 p.e. are treated as cosmic ray muons.

- 200 cm fiducial volume cut. This cut removes events with a reconstructed vertex position outside the 22.5 kton fiducial volume, which starts 200 cm inward of the ID walls. Additionally, those events for which the event reconstruction algorithm failed to find a vertex position are also discarded.
- 50 μ sec time difference cut. This cut removes events which follow too closely in time to the previous event in SK. The distribution of time differences is shown in Figure 6.2. This cut removes decay electron events and events caused by electronic “ringing” of the DAQ electronics. These “ringing” events typically follow very large events.

- OD triggered events. Events with a trigger generated by the OD DAQ electronic, or with more than 20 tubes in time with the ID event are removed. This prevents contamination of the data sample from entering events.
- Poor fit cut. If the goodness of fit value returned with the reconstructed vertex position is less than 0.4, the event is cut. Events from many backgrounds will return poor goodness of fit values and are thus removed.
- First electronic noise cut. Events that are generated by electronic noise have a large fraction of hit PMTs with a relatively low amount of charge in each hit PMT. If the fraction of hit tubes in an event with fewer than 0.5 p.e. per channel exceeds 40%, the event is removed as an electronic noise event. One identified source of these events is failing fluorescent light bulbs in the electronic huts.
- Second electronic noise cut. Another class of electronic noise events are generated from a single ATM board. If greater than 95% of the PMT hits from an event originate from a single ATM, the event is removed.
- Flasher cut. Events originating from a flashing PMT, that is a PMT that generates an internal electrical arc which causes a flash of light and a cluster of hit tubes in the detector, are removed by the flasher cut. Events originating from a flashing PMT usually contain a single PMT channel with a high charge value, as well as a cluster of hits surrounding this tube. If any hit PMT in an event has more than 50

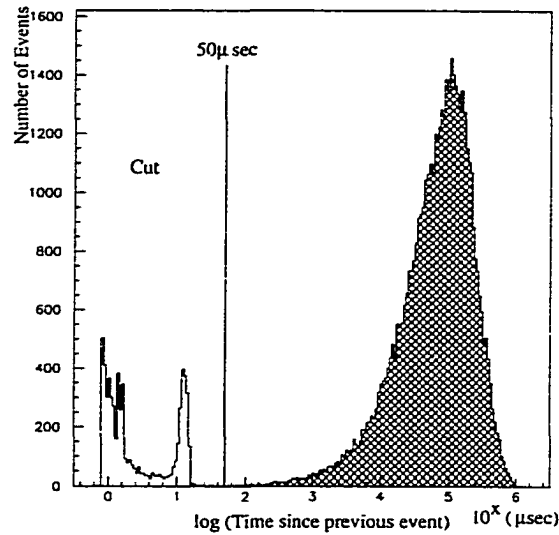


Figure 6.2: Distribution of time differences between events. Events that follow another event within 50 μsec are removed.

photo-electrons of charge, and is accompanied by 5 or more hit nearest neighbors, the event is removed.

6.1.2 Spallation Cut

Spallation products are produced by energetic cosmic ray muons as they pass through the detector. These products are created by:



where X can include an unstable nuclide. Spallation products created include ${}^{12}\text{B}$, ${}^9\text{Li}$, ${}^8\text{B}$, ${}^{15}\text{C}$, among others. A listing of considered spallation products can be found in Reference [27]. The half lives of these nuclides range from a few milliseconds (${}^{13}\text{O}$, 8.6 ms) to a few seconds (${}^{11}\text{Be}$, 13.8 s). The beta decay of these nuclides at some later time could mimic a solar neutrino event. Luckily, these events are correlated in time and space to the parent

cosmic ray muon, and this correlation is used to remove these events from the data sample by a likelihood analysis. These events represent the dominate background for solar neutrinos above ~ 7 MeV.

The likelihood analysis uses three variables to relate events in the solar neutrino event sample to cosmic ray muons to search for spallation events. These include:

- DL The closest distance between the cosmic ray muon fitted track and the vertex of the solar neutrino candidate event. Spallation events are strongly correlated in space to the parent muon track.
- DT The time difference between the parent muon and the solar neutrino candidate event. Most spallation products have relatively short half lives and are therefore strongly correlated in time to the parent muon.
- Q_{res} The residual charge of the muon, defined as:

$$Q_{res} = Q_{muon} - p(t)L \quad (6.2)$$

where Q_{muon} is the total charge deposited by the muon as it passed through the SK detector, L is the path length of the fitted muon track through the detector, and $p(t)$ is the expected amount of collected charge per unit path length. $p(t)$ has a nominal value of 24.1 p.e./cm and includes corrections for variations in water transparency over time (t). A positive Q_{res} value indicates that a muon likely underwent interactions as it passed through the detector, and spallation products are therefore more probable.

The spallation likelihood functions are determined separately for muons with a good track fit and for muons with a failed track fit. For muons with a good track fit, DR, DT and Q_{res} values are used to determine the likelihood value. For muons with failed fits, only DT and Q_{muon} are used to determine the likelihood function. The functional form of the likelihood functions used are available in Reference [41].

For each event in the solar neutrino candidate file, the previous 200 muon events are considered, and the largest likelihood value found is taken for that event. Maximum likelihood distributions for the a subset of the solar neutrino data sample are shown in Figures 6.3 and 6.4 for values originating from a muon with and without a good track fit, respectively. Also shown in these distributions are maximum likelihood distributions for a sample of events given a random vertex in the detector. These random events are used to measure the dead time of the spallation cut for the solar neutrino analysis. The spallation cut shown has a dead time of 21.1%, as measured by the fraction of the random vertex sample that was removed by this cut.

6.1.3 Second Reduction

The second set of reduction cuts is designed to reduce the background at low energies. The rate of background grows exponentially larger as the energy threshold of the detector is lowered. These cuts are designed to remove as much of these background events while keeping as much of the solar neutrino signal as possible.

6.1.3.1 New goodness cut

The new goodness cut (described in Section 4.5.1) is applied to the data sample. If the *goodfrac* value exceeds 20%, then the event is removed as

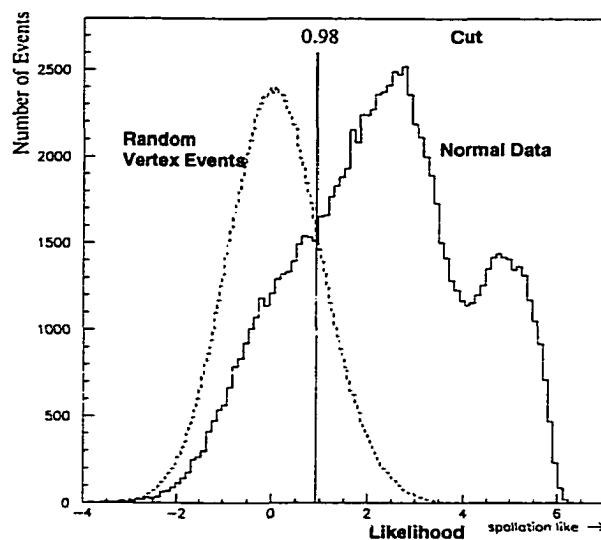


Figure 6.3: Spallation maximum likelihood distributions from muons with fit tracks for a set of the solar neutrino data and for a sample where random event vertices are used. The cut value of 0.98 is used.

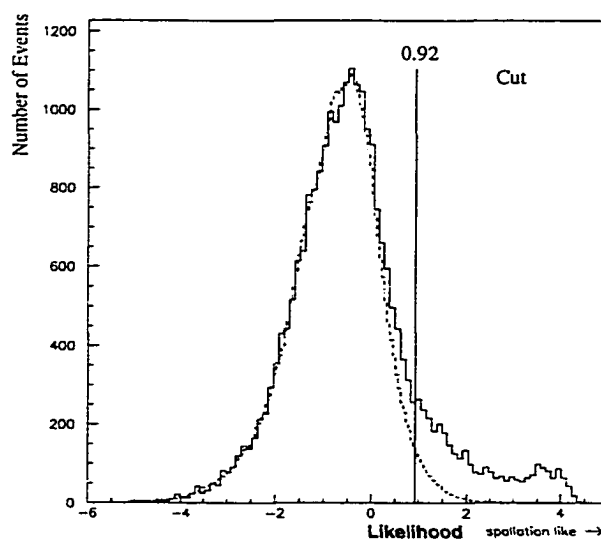


Figure 6.4: Spallation maximum likelihood distributions from muons without a fit track. The cut value of 0.92 is used.

background. This cut is better than 90% efficient at keeping known-good electron events, such as LINAC data or ^8B MC data, while reducing the background level below 7 MeV by $\sim 50\%$.

6.1.3.2 Clusfit Cut

A 200 cm fiducial volume cut based on the clusfit vertex (described in Section 4.5.2) is next applied. If the reconstructed clusfit vertex for an event is no longer in the fiducial volume starting 200 cm inward from the ID walls, then the event is removed as background. This cut is roughly 90% efficient at keeping known-good events including LINAC, Nickel and events from the ^8B MC. This cut reduces the background level below 7 MeV by $\sim 15\text{-}20\%$.

6.1.3.3 Gamma Cut

The gamma cut is another fiducial volume-like cut that targets events that appear to be originating from the wall of the ID. The reconstructed direction is projected backwards from the vertex position until a wall is encountered. This distance, d_{eff} , is used as the gamma cut parameter, and is illustrated in Figure 6.5. For energies 6.5 MeV or greater, any event with a d_{eff} value of 450 cm or smaller is removed from the data sample. For energies between 5.5-6.5 MeV, events with d_{eff} values less than 800 cm are removed.

This cut significantly reduces the remaining background observed near the edges of the detector in the reconstructed vertex distributions and flattens the observed reconstructed direction distributions, as illustrated in Figure 6.6. The 450 cm gamma cut yields a 7.8% dead time, measured by the fraction of ^8B MC events that are removed, while the 800 cm gamma cut has a 14% dead time.

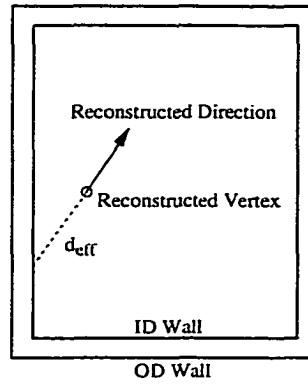


Figure 6.5: Definition of the d_{eff} used in the gamma cut.

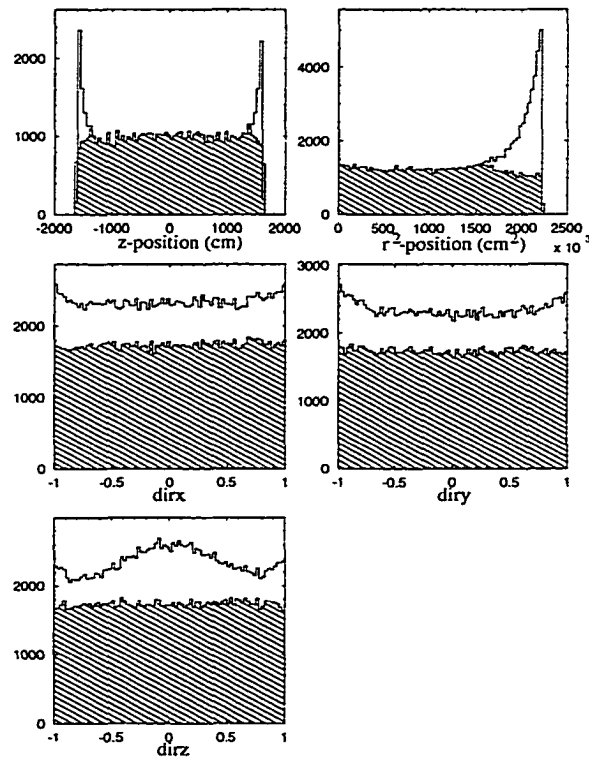


Figure 6.6: Reconstructed vertex and direction distributions of the solar neutrino sample before (plain histograms) and after (hatched histograms) the gamma cut.

Table 6.1: Reduction summary. Values listed are the number of events remaining at each step of the reduction.

Cut Description	Number of Events
Raw data	11.1×10^8
Total Charge < 1000 p.e	8.74×10^8
200 cm fiducial volume cut	2.68×10^8
50 μ sec time difference cut	2.25×10^8
OD trigger/OD hit cut	2.20×10^8
Electronic noise cuts	2.18×10^8
Flasher cut	2.18×10^8
Goodness of fit cut	2.15×10^8
Energy precut ($E > \sim 4.3$ MeV)	3.03×10^7
New goodness cut	1.21×10^7
Clusfit fiducial volume cut	8.68×10^6
Spallation cut	5.91×10^6
Gamma cut	9.72×10^5
Final sample (Energy 5.5-20 MeV)	192377

The reduction is summarized in Table 6.1, showing the number of events remaining after each step in the reduction. This is graphically summarized in Figure 6.7, which illustrates 4 steps in the reduction as a function of energy. At energies greater than 7 MeV, the spallation cut is the most effective cut. At lower energies, where the background rate really starts to grow, the cuts of the second reduction, including the clusfit and gamma cut shown, are the most effective cuts at removing background.

The final sample contains 192,377 events between 5.5 and 20.0 MeV, and the solar neutrino extraction (see Chapter 7) is applied to this sample of events.

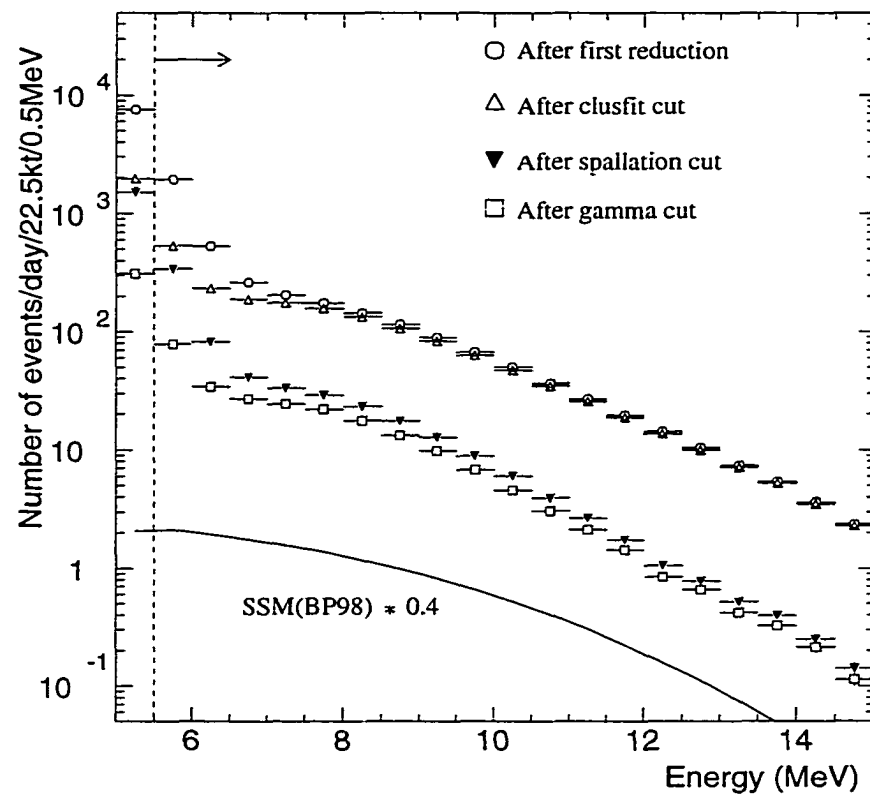


Figure 6.7: The energy distribution of events in the solar neutrino data sample at 4 steps in the reduction.

6.2 Natural ^{16}N Analysis

^{16}N events are sought in the data sample, and the same reduction steps are applied to this event sample as are applied to the solar neutrino data sample. ^{16}N events occur at a rate similar to that of solar neutrinos. The energy distribution of these events shares a large region in energy with the ^8B recoil electron spectrum, and the events are uniformly distributed in the detector volume and in livetime, just as solar neutrinos. The measured rate of ^{16}N events is compared to the calculated expected rate. If these rates agree, this would indicate that the solar neutrino reduction is not a source of signal loss, and can not be considered for the list of explanations for the solar neutrino deficit.

The collected sample of ^{16}N can also be considered for use as an energy calibration source with limited statistics. The use of these events for energy calibration is covered in Reference [42].

6.2.1 Muon Capture on ^{16}O

The creation of ^{16}N occurs naturally as a background to the solar neutrino measurement. A stopped μ^- can be captured by a ^{16}O nucleus in the water of the detector,



A fraction of ^{16}N created will be in the ground state, and beta decays with a 7.13 s half life. The rate of these events is measured by collecting events that occur in the area surrounding the stopping point of a captured muon and subtracting random background events.

6.2.1.1 Predicted Rate

The predicted rate of ^{16}N events is calculated in the inner-most 11.5 kton fiducial volume (500 cm inward of the ID walls) using the measured stopping muon rate from the muboy muon track fitter (see Section 4.4.1). The 11.5 kton volume is used in place of the entire 22.5 kton volume to avoid contamination of the stopping muon rate near the edges of the volume due to misidentification of through-going muons. The expected rate of ^{16}N events is then calculated:

$$N_{ev} = N_{stopmu} \left(\frac{\mu^-}{\mu^+ + \mu^-} \right) f_{capture} f_{gs} \epsilon \quad (6.4)$$

where:

- N_{stopmu} is the rate of stopping muons found in the 11.5 kton volume per day. This rate is measured using the muboy muon fitter that is also used in the search for ^{16}N events and is found to be 2530 ± 60 (*stat.* + *sys.*) per day.
- $\left(\frac{\mu^-}{\mu^+ + \mu^-} \right)$ is the fraction of muon events that are μ^- , taken to be 0.44 ± 0.01 [43]. As this ratio has an energy dependence, the value corresponding to a surface muon energy of ~ 1 TeV is used.
- $f_{capture}$ is the fraction of stopped μ^- that are captured on ^{16}O before decaying. This is determined by the known capture and decay rates:

$$\begin{aligned} f_{capture} &= \frac{\tau_{\mu^-}}{\tau_{cap}} \\ &= \frac{1}{1 + \frac{\tau_{cap}}{\tau_{dk}}} \end{aligned} \quad (6.5)$$

where:

$$\begin{aligned}
 \tau_{\mu^-} &= \text{Lifetime of a } \mu^- \text{ in water} \\
 \frac{1}{\tau_{\mu^-}} &= \frac{1}{\tau_{dk}} + \frac{1}{\tau_{cap}} \\
 \tau_{dk} &= \text{Measured muon decay lifetime in vacuum}[2] \\
 &= 2.19703 \pm 0.00004 \mu\text{sec} \\
 \tau_{cap} &= \text{Measured muon capture time on } ^{16}\text{O}[44] \\
 &= 9.747 \pm 0.006 \mu\text{sec}
 \end{aligned}$$

The capture fraction is calculated to be $18.39\% \pm 0.01\%$.

- f_{gs} is the fraction of captures that result in the formation of ^{16}N in the ground state. Only the 4 lowest energy states of the ^{16}N nucleus will end up in the ground state, where beta decay can occur. The other, higher energy states decay primarily by neutron emission. f_{gs} is taken to be the ratio of the sum of the partial capture rates of the ground state producing levels to the total capture rate. These partial capture cross sections from the ^{16}O ground state to these 4 ^{16}N states are listed in Table 6.2. Using these values and the total capture cross section from above, f_{gs} is determined to be $9.0\% \pm 0.7\%$.
- ϵ is the triggering and reconstruction efficiency for ^{16}N and is determined by MC simulation to be $64.6\% \pm 0.2\%$.

This results in a predicted ^{16}N event rate in the 11.5 kton fiducial volume of 11.9 ± 1.0 events per day.

Table 6.2: Partial capture rates for μ^- capture from the ^{16}O ground state to the beta decay capable states of ^{16}N . These values are taken from References [45, 34].

Transition (Initial \rightarrow Final)	Partial Capture Rate (sec) $^{-1}$
$0^+ \rightarrow 0^-$	1560 ± 108
$0^+ \rightarrow 1^-$	1345 ± 135
$0^+ \rightarrow 2^-$	6300 ± 700
$0^+ \rightarrow 3^-$	<80
Total	9205 ± 725

6.2.1.2 ^{16}N Results

In order to extract these few events per day from the data set, a specialized data search is implemented. The reconstructed stopping muon positions from the muboy muon track fitter are used as the starting point for the search. These fit results are used as an input, along with the input data sample for the solar neutrino analysis, to the ^{16}N search algorithm. This search finds stopping muon events that are not followed by a decay event in $100\mu\text{s}$, as a muon that decays can not be captured on ^{16}O . Once an “undecayed” muon is found, any events in the solar neutrino data sample are saved that occur within a sphere of radius 335 cm centered at the stopping muon point, as well as in a time window of 100 ms to 30 seconds following the stopping muon. The sphere size of 335 cm is used as it is large enough to contain all expected signal events while keeping contributions from random backgrounds as small as possible. No limit is placed on the number of candidate signal events a stopping muon can produce to prevent biasing from the random background in SK. The result of this search is called the signal sample, and contains the ^{16}N events as well as natural background events. To account for this natural

background, a background sample is also obtained by offsetting the times of the “undecayed” muons by 100 seconds into the future and performing the same search again.

The steps of the reduction algorithm are then applied to both the signal and the background samples, excluding the spallation cut. As these events are associated with a cosmic ray muon, the spallation cut has a good chance of removing ^{16}N events. The effects of the natural background are removed by performing a statistical subtraction of the results for the background sample from the signal sample. For the ^{16}N search, slightly more livetime has been incorporated than the livetime of the solar neutrino analysis, with 1,003.8 days of data included in the ^{16}N search. In the inner 11.5 kton fiducial volume, 17,714 signal, with 6,267 background events are found in this livetime period, resulting in a rate of ^{16}N events of 11.4 ± 0.2 events/day. This result agrees well with the predicted rate of 11.9 ± 1.0 events/day and indicates that no loss of signal is evident for events in the same energy range of solar neutrinos.

CHAPTER 7

SOLAR NEUTRINO SIGNAL EXTRACTION

The steps of the reduction chain (see Chapter 6) are applied to the data sample collected at SK, and a final sample of solar neutrino candidate events is produced, with reconstructed recoil electron energies between 5.5-20 MeV. Ideally this sample would contain only solar neutrinos, but in reality a background that grows in event rate as the energy threshold lowers is found. In order to separate the solar neutrinos from the background and perform a measurement of the solar neutrino flux, the correlation of solar neutrino events with the direction to the Sun is used.

This chapter describes the solar neutrino extraction method used in this analysis, and considers the statistical and systematic errors associated with this measurement. The results of this signal extraction method are presented in the Chapter 8.

7.1 Signal Extraction Method

Solar neutrinos interact in SK by neutrino-electron elastic scattering. The electron produced is well-correlated with the incoming neutrino direction (see Figure 5.9). This correlation is used as the primary method to separate signal from background. For each event in the final sample, the time of day is used to calculate the direction a solar neutrino would be traveling by projecting the location of the Sun through the detector. The angle between this projected solar direction and the reconstructed direction of an event in the final sample

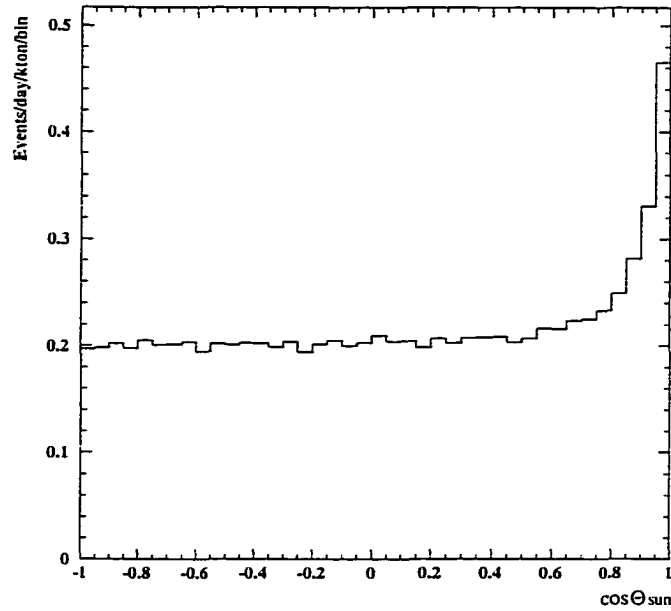


Figure 7.1: The distribution of $\cos\theta_{sun}$ for the final sample of solar neutrino candidates. The peak seen near $\cos\theta_{sun} = 1.0$ is due to solar neutrino events.

is found, θ_{sun} . A histogram of the $\cos\theta_{sun}$ is presented in Figure 7.1 and shows an excess of events at $\cos\theta_{sun} = 1$, corresponding to events originating in the direction of the Sun. A count of the number of excess events is a measure of the flux of solar neutrinos. This analysis employs a signal extraction method based on that of R. Sanford[27].

7.1.1 First Order Extraction

The signal extraction method starts with the assumption that the background for solar neutrinos has a flat distribution in $\cos\theta_{sun}$. It is also assumed that all solar neutrino events are confined to a region with $\cos\theta_{sun} \geq 0.5$. These assumptions are later refined for small deviations from a flat background distribution as well as to correct for solar neutrino events with

$\cos\theta_{sun} < 0.5$. The first order signal is measured by partitioning the $\cos\theta_{sun}$ distribution in 40 bins as shown in Figure 7.2. The following regions and quantities are defined:

- Region R_1 : Bins 1-30 (30 bins total). These bins correspond to events with $\cos\theta_{sun} < 0.5$. This area is taken to represent the background. This region contains a total of N_1 events.
- Region R_2 : Bins 31-40 (10 bins total). These bins correspond to events with $\cos\theta_{sun} \geq 0.5$. This area is taken to represent the solar neutrino signal on top of a flat background. This region contains a total of N_2 events.
- $N_{SIG} \equiv$ Number of signal events in Region R_2 .
- $N_{BKG} \equiv$ Number of background events in Region R_2 .

With the assumption of a flat background, Region R_1 is used to estimate the background contained in the signal (Region R_2) region:

$$N_{bkg} = \frac{N_1}{3}. \quad (7.1)$$

The solar neutrino signal is then calculated by subtracting this background estimation from the number of events in Region R_2 :

$$\begin{aligned} N_{sig} &= N_2 - N_{bkg} \\ &= N_2 - \frac{N_1}{3}. \end{aligned} \quad (7.2)$$

This first order signal is made by simply counting the number of events in the two regions of the $\cos\theta_{sun}$ histogram. This simple definition for solar

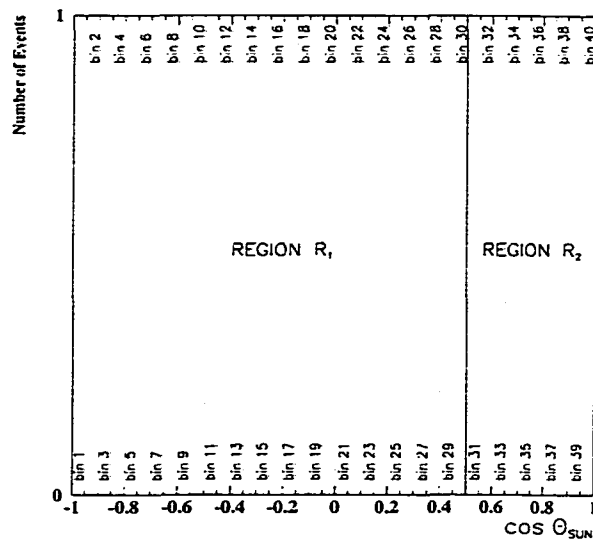


Figure 7.2: Definition of regions and bins used in the $\cos\theta_{sun}$ plot for the signal extraction method.

neutrino events is now refined to correct for non-flat backgrounds and solar neutrino events in Region R₁. These corrections will change the measured signal by $\sim 10\%$ from this simple technique described above.

7.1.2 Non-Flat Background Corrections

The flat background assumption used in the first order signal can be refined to take into account small deviations from a flat distribution in the $\cos\theta_{sun}$ plot for background events. There is no reason to expect a completely flat background in the $\cos\theta_{sun}$ distribution, as the background is a complicated convolution of background event distributions determined by the geometry of the SK detector, the motion of the Sun around the detector, and the asymmetry of the backgrounds in local coordinates. If it is assumed

that background events occur independently of the location of the Sun, and a background event's location in the $\cos\theta_{sun}$ plot is simply determined by the chance location of the Sun at that event's time, then the background events themselves can be used to quantify the non-flat background.

Background events are defined as events that occupy Region R_1 , as well as the fraction of events in Region R_2 that are not solar neutrino events. For each background event, the $\cos\theta_{sun}$ value is determined many times by recalculating the position of the Sun based on randomly chosen event times from other events in the final sample, resulting in a distribution of $\cos\theta_{sun}$ that could have been produced by that single background event. Figure 7.3 shows the resulting background distribution normalized to 1.0 for a single background event, in this case with a true $\cos\theta_{sun} = -0.95$. This process is repeated for each event in the final sample of neutrino candidates, with a background normalization that depends on the region each event occupies. Events in Region R_1 , defined to contain only background, are normalized to 1.0. Events in Region R_2 are normalized to an event's probability of being a background event. This probability is defined to be:

$$Prob(bkg) = \frac{(N_{bkg}/10.0)}{N(i)}, \quad (7.3)$$

where:

$N_{bkg}/10.0$ = Number of flat background events in Region R_2 .

$N(i)$ = Number of events in the i^{th} bin of the original $\cos\theta_{sun}$ distribution.

The time-smeared normalized background contributions from all events in the final sample are summed to create a new background shape estimation.

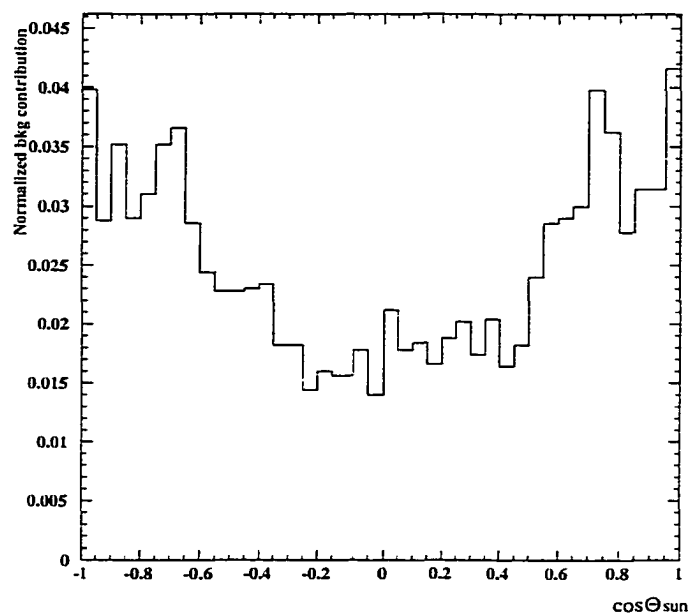


Figure 7.3: An example of the non-flat background determination. A single background event, in this case with a true $\cos \theta_{\text{sun}} = -0.95$, has been smeared in time to produce a distribution of $\cos \theta_{\text{sun}}$ that could have been produced by this event. The distribution has been normalized to 1.0.

This time smearing of events is repeated a second time. Only this time, the newly obtained background shape estimation is used to determine the probability of an event being a background event in Region R_2 :

$$Prob(bkg) = \frac{N_{bkg}(i)}{N(i)} \quad (7.4)$$

where:

$$N_{bkg}(i) = \text{The number of events in the } i^{th} \text{ bin} \\ \text{of the first background shape estimation.}$$

Events in Region R_1 are still normalized to 1.0.

This process is iterated, using the background shape obtained from the previous iteration to determine background probabilities in the current iteration, until the result converges. Convergence is determined by calculating the solar neutrino signal at each iteration:

$$N_{sig} = N_2 - \sum_{Region R_2} N_{bkg}(i) \quad (7.5)$$

where $N_{bkg}(i)$ is the background shape from the current iteration. The signal and background are said to have converged when the difference in N_{sig} between the current and previous iterations is less than 0.1% for two consecutive iteration cycles. Convergence is achieved on average after ~ 6 iterations.

The original $\cos\theta_{sun}$ distribution for the 5.5-20 MeV energy interval for the final sample of solar neutrino candidates is presented with the final time-smearred non-flat background distribution in Figure 7.4. For this sample, a flat background assumption would yield a solar neutrino excess of 13,768 events. The final non-flat background finds an excess of 13,820 events, illustrating that the non-flat background corrections are small.

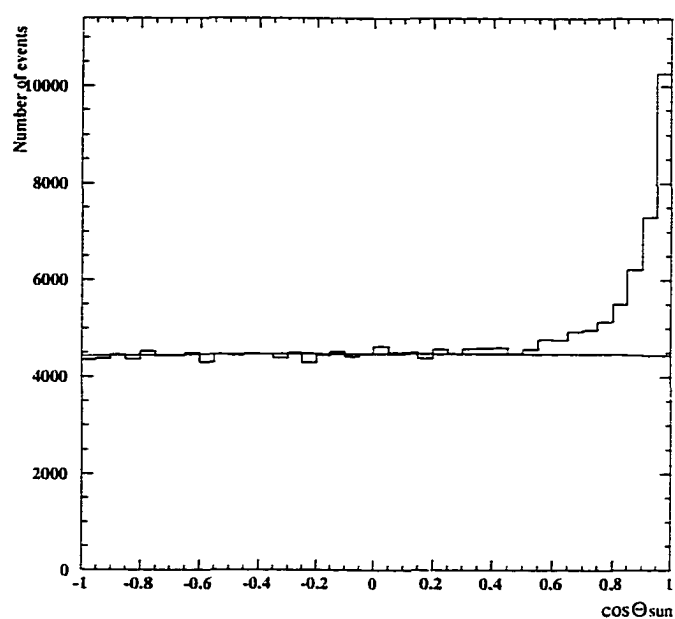


Figure 7.4: The $\cos\theta_{sun}$ distribution for the final sample of solar neutrino candidates with the final converged time-smearred non-flat background overlaid.

7.1.3 Corrections for Angular Cut Efficiency

Both the flat and time-smeared non-flat background signal extraction methods assumed that all solar neutrinos are contained in Region R_2 , with $\cos\theta_{sun} \geq 0.5$. Of course not all solar neutrino events are going to fall into Region R_2 , so the measured number of solar neutrinos must be corrected to obtain the true number of solar neutrino events. If the size of the signal region (Region R_2) was increased, to $\cos\theta_{sun} = 0.0$ for example, this would reduce the size of the angular cut correction, but would also increase the statistical error of the solar neutrino extraction as more events from the final sample would be considered in the signal region. The measured signal must be corrected for solar neutrino events that are reconstructed with $\cos\theta_{sun} < 0.5$, as seen in the $\cos\theta_{sun}$ distribution of ^8B MC events (see Figure 5.9). This correction is obtained from the ^8B neutrino MC sample by calculating the fraction of MC solar neutrino events with a reconstructed value of $\cos\theta_{sun} < 0.5$ and using this efficiency to correct the measured number of events.

The correction for the angular cut efficiency is doubly important for obtaining the correct number of solar neutrino signal events. First, signal events with $\cos\theta_{sun} < 0.5$ are not considered in the signal determination described above, so the true number of solar neutrino events is under-counted. Second, these events with $\cos\theta_{sun} < 0.5$ are counted as background, resulting in an over-counting of the background. To correct for this double miscounting, the signal is corrected by rewriting Eqn 7.2 as:

$$N_{sig} = (N_2 + x) - \frac{(N_1 - x)}{3} \quad (7.6)$$

where:

$$\begin{aligned}
 x &= \text{number of signal events with } \cos\theta_{sun} < 0.5 \\
 &= (1 - \epsilon)N_{sig} \\
 \epsilon &= \text{efficiency of the } \cos\theta_{sun} = 0.5 \text{ angular} \\
 &\quad \text{cut as measured by } ^8\text{B MC solar neutrino events.}
 \end{aligned}$$

Substituting for x and solving for N_{sig} results in:

$$N_{sig} = \frac{N_2 - N_1/3}{(4\epsilon - 1)/3} \quad (7.7)$$

The numerator of equation 7.7 is simply the original definition for the first order signal (Eqn 7.2). Therefore, Eqn 7.7 can be rewritten as:

$$N'_{sig} = \frac{N_{sig}}{\epsilon'} \quad (7.8)$$

where:

$$\begin{aligned}
 N'_{sig} &= \text{Angular cut efficiency corrected number} \\
 &\quad \text{of signal events} \\
 \epsilon' &= \frac{(4\epsilon - 1)}{3}
 \end{aligned}$$

Since the correction for the time-smeared non-flat background is small, this correction for angular cut efficiency can also be applied to the value of N_{sig} from Eqn 7.5. Therefore, the non-flat background corrected signal is corrected for the angular cut efficiency (ϵ'), and the true number of solar neutrino events is obtained. For the 5.5-20 MeV final sample, the 13,820 events are corrected by a measured efficiency of $\epsilon = 92.96\%$ ($\epsilon' = 90.61\%$), and total of 15,252 recoil electron events resulting from solar neutrino interactions are

obtained. This number is used as a measure of the flux of solar neutrinos from the Sun.

7.1.4 Measurement of the Energy Spectrum

Some neutrino oscillation scenarios predict measurable spectral distortions in the measured recoil electron spectrum. To search for these distortions, the recoil electron spectrum is measured and compared to the expectations from MC with no oscillations. The measurement of the spectrum of recoil electrons is done in much the same way as the measurement of the total flux. In the case of the spectrum measurement, the final sample of solar neutrino candidates is divided according to the reconstructed electron energy, and the same signal extraction, including the non-flat background and angular efficiency corrections, is applied to the data in each energy bin. For the time-smeared non-flat background analysis, only events from within a given energy bin are used to calculate the background.

The choice of selecting events with $\cos\theta_{sun} \geq 0.5$ to represent the signal region (Region R₂) is a balance between including more of the actual signal (increasing size of Region R₂) and reducing the statistical error (decreasing the size of Region R₂). The value of $\cos\theta_{sun} = 0.5$ works well for many energy bins, as well as the overall 5.5-20 MeV flux measurement, but for some energy bins, a wider or narrower signal region is desirable. Since the angular resolution of the detector is energy dependent (see Table 3.1), the highest energy and lowest energy bins are respectively narrowed and widened.

In the case of the lowest two energy bins (5.5-6.0 and 6.0-6.5 MeV) the detector angular resolution is poor, and many events have $\cos\theta_{sun} < 0.5$. For

these energy bins, the angular cut is relaxed, allowing more of the true signal to be included in the signal region and keeping the angular cut efficiency high (near 90%). These bins have higher levels of background, and widening the signal region does little to increase the statistical error. For the 5.5-6.0 MeV bin, the angular cut location is set at $\cos\theta_{sun} = 0.3$ and for the 6.0-6.5 MeV bin, the angular cut location is set at $\cos\theta_{sun} = 0.4$.

For the highest energy bins (13.0-13.5, 13.5-14.0, 14.0-20.0 MeV), the case is just the opposite. At these higher electron energies, the angular resolution of the detector is much better, allowing a smaller-sized signal region to be used. The background level in these bins is also much lower than the low energy bins, so any reduction in the size of the signal region is reflected in smaller statistical errors for the signal measurements. For these highest energy bins, 13.0-13.5, 13.5-14.0, 14.0-20.0, the angular cut location in $\cos\theta_{sun}$ is set to 0.55, 0.60, 0.65 respectively.

Changing the location of angular cut requires rewriting the signal extraction equations. First, the first order flat signal (Eqn 7.2) is rewritten:

$$\begin{aligned} N_{sig} &= N_2 - N_{bkg} \\ &= N_2 - \xi N_1 \end{aligned} \tag{7.9}$$

where:

$$\xi = \frac{40 - y}{y}$$

$$y = \text{The bin number of cut bin out of 40 bins.}$$

The change in the division between signal and background regions also affects the calculation of N_{sig} in the correction for the angular efficiency cut

(Eqn 7.7). The value of ϵ' is defined more generally:

$$\epsilon' = \epsilon + \epsilon\xi - \xi \quad (7.10)$$

where:

ϵ = Efficiency for the cut bin value as
measured by ^8B solar neutrino MC simulation.

ξ = As defined for Eqn 7.9

The $\cos\theta_{sun}$ distributions and the time-smeared non-flat background for each energy bin considered are presented in Figure 7.5 and Figure 7.6. The numerical results for each energy bin are summarized in Table 7.1, including the flat signal, cut bin value, non-flat signal, angular cut efficiencies and total extracted signal.

7.1.5 Measurement of Day/Night and Seasonal Fluxes

Some neutrino oscillation scenarios predict measurable flux differences between day time and night time observations, or between different seasons of the year. To search for such variations, the final sample of solar neutrino candidates is divided into subsets and relative flux measurements for each subset are performed. These flux measurements are performed in the same manner as the total flux measurement described in Sections 7.1.1- 7.1.3, with the angular cut at $\cos\theta_{sun} = 0.5$. For the time-smeared non-flat background analysis, only events from within each subset are used to calculate the background.

A day/night flux difference would likely manifest itself as an increase in the measured flux at night, or an enhancement of flux for events that

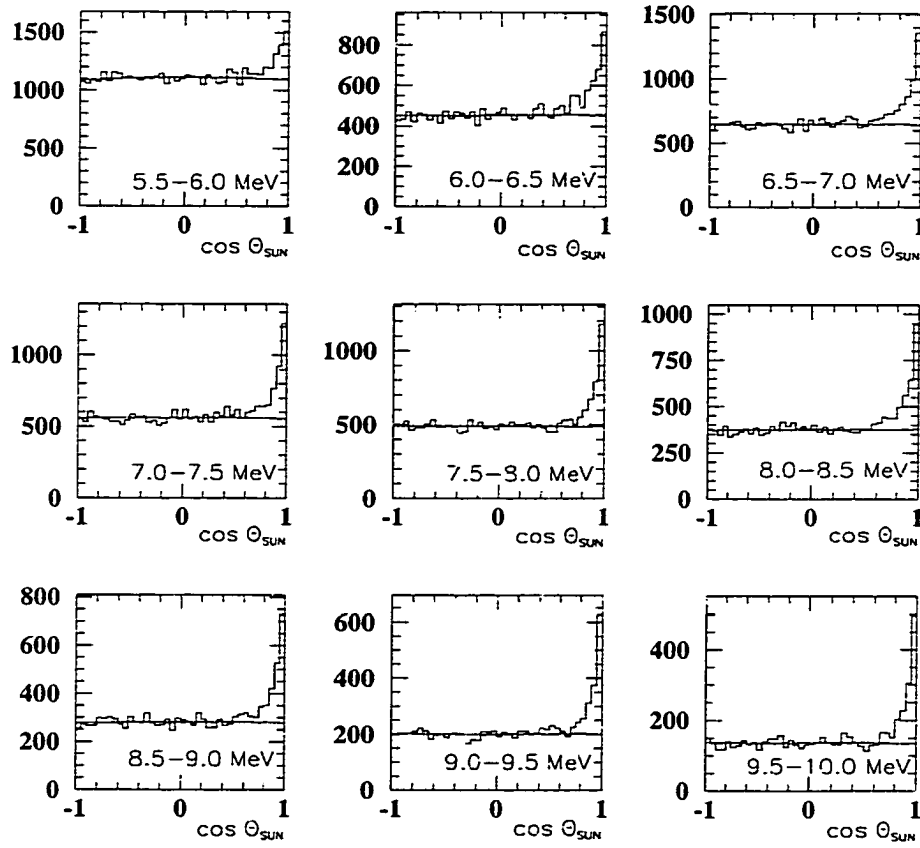


Figure 7.5: The $\cos\theta_{sun}$ distribution along with the time-smeared non-flat background distribution for each energy bin for energies 5.5-6.0 to 9.5-10.0 MeV.

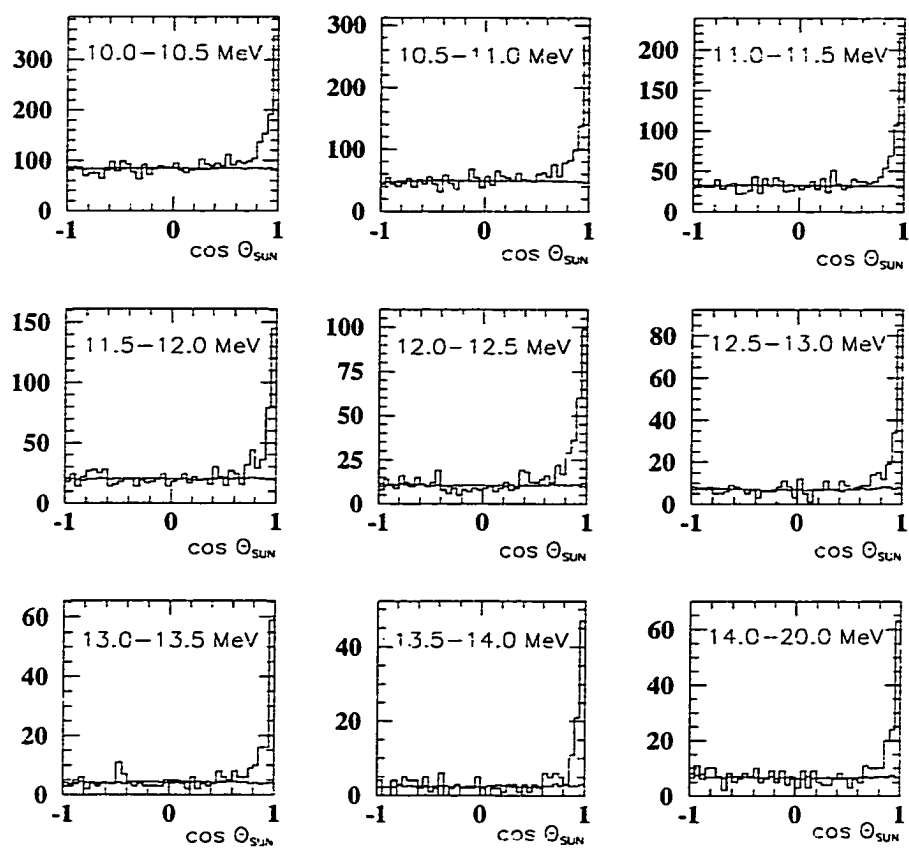


Figure 7.6: The $\cos\theta_{sun}$ distribution along with the time-smearred non-flat background distribution for each energy bin for energies 10.0-10.5 to 14.0-20.0 MeV.

Table 7.1: Summary of spectrum bins. Signals are listed as rates, in events/day. Bins 5.5-6.0 and 6.0-6.5 have been normalized by the 700.3 day livetime of these bins. All other bins have been normalized by the 980.4 day livetime.

Bin Energy (MeV)	Flat Signal	cos(angle) (Cut bin)	Non-flat Signal	ϵ (ϵ')	Extracted Signal
5.5-6.0	1.81	0.3 (26)	1.84	94.54 (91.60)	2.01
6.0-6.5	1.79	0.4 (28)	1.75	93.50 (90.71)	1.93
6.5-7.0	1.85	0.5 (30)	1.85	91.54 (88.72)	2.08
7.0-7.5	1.66	0.5 (30)	1.68	92.43 (89.91)	1.86
7.5-8.0	1.47	0.5 (30)	1.48	93.03 (90.71)	1.63
8.0-8.5	1.44	0.5 (30)	1.44	93.67 (91.56)	1.57
8.5-9.0	1.13	0.5 (30)	1.13	94.16 (92.21)	1.23
9.0-9.5	0.902	0.5 (30)	0.892	94.65 (92.87)	0.960
9.5-10.0	0.738	0.5 (30)	0.743	94.94 (93.25)	0.797
10.0-10.5	0.598	0.5 (30)	0.594	95.13 (93.51)	0.635
10.5-11.0	0.502	0.5 (30)	0.508	95.49 (93.99)	0.541
11.0-11.5	0.356	0.5 (30)	0.361	95.83 (94.44)	0.383
11.5-12.0	0.250	0.5 (30)	0.246	95.90 (94.53)	0.261
12.0-12.5	0.215	0.5 (30)	0.212	96.03 (94.71)	0.224
12.5-13.0	0.143	0.5 (30)	0.138	96.41 (95.21)	0.145
13.0-13.5	0.098	0.55 (31)	0.100	95.79 (94.56)	0.105
13.5-14.0	0.086	0.6 (32)	0.084	95.01 (93.76)	0.089
14.0-20.0	0.105	0.65 (33)	0.102	94.05 (92.79)	0.110

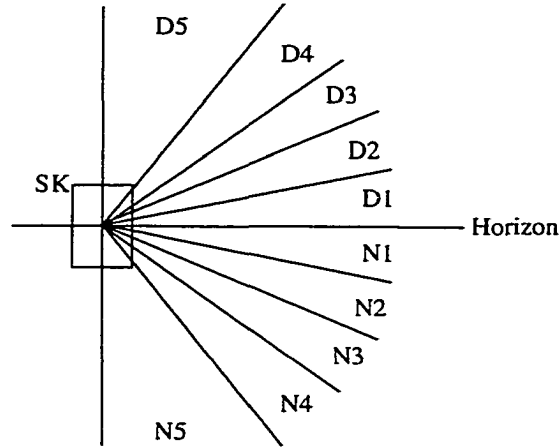


Figure 7.7: Definition of D1-D5 and N1-N5 bins based on the location of the Sun relative to the SK detector. Night is considered any time when the Sun is below the horizon and day is any time when the Sun is above the horizon.

pass through the core of the Earth. To look for these effects, relative flux measurements are performed for the all day-time subset and the all night-time subset separately, based on the location of the Sun relative to the horizon at SK. These day and night flux measurements are used to find a flux asymmetry parameter. The day and night time periods are further divided into 5 flux bins each (10 bins total). The data are divided according to the known zenith angle of the Sun at the time of each event, as shown in Figure 7.7. Table 7.2 presents the definition of each bin, as well as livetime and the average Earth-Sun separation for each subset.

A variation in the flux measured in different seasons of the year, as the Earth-Sun distance changed, could also be a sign of neutrino oscillations. To look for flux variations in different seasons, the data are divided into subsets based on the distance between the Earth and the Sun at the time of each

Table 7.2: Definition of day/night subsets.

Subset	$\cos(ZenithAngle)_{sun}$	Livetime (days)	$\langle \frac{1}{r^2} \rangle$
Day	-1.0 – 0.0	448.02	0.9935
Night	0.0 – 1.0	492.33	1.0012
D1	-1.0 – -0.8	84.01	0.9986
D2	-0.8 – -0.6	90.76	1.0004
D3	-0.6 – -0.4	117.91	1.0045
D4	-0.4 – -0.2	103.20	0.9913
D5	-0.2 – 0.0	92.16	0.9767
N1	0.0 – 0.2	84.95	0.9969
N2	0.2 – 0.4	96.54	0.9949
N3	0.4 – 0.6	132.44	0.9911
N4	0.6 – 0.8	99.26	1.0067
N5	0.8 – 1.0	79.14	1.0235

event in the final sample. 10 subsets are created based on this distance, as shown in Figure 7.8. Two larger bins are also created to obtain a seasonal asymmetry parameter. Table 7.3 contains the definition of each bin used in the seasonal flux measurement, as well as the livetime in each bin, and the livetime weighted average Earth-Sun distance for that bin.

7.1.5.1 Corrections for Eccentricity

The orbit of the Earth around the Sun is not circular, but elliptical. Therefore, a $\sim 3\%$ modulation in the flux of solar neutrinos is expected simply from the eccentricity of the Earth's orbit. To make accurate comparisons between solar neutrino fluxes measured in different seasonal periods as well as comparisons to MC simulations, which are performed at 1 AU, this eccentricity must be corrected for. A correction is also required for day/night flux measurements, since day data (night data) are collected primarily in summer (winter) when the Earth is farthest (nearest) from (to) the Sun. The

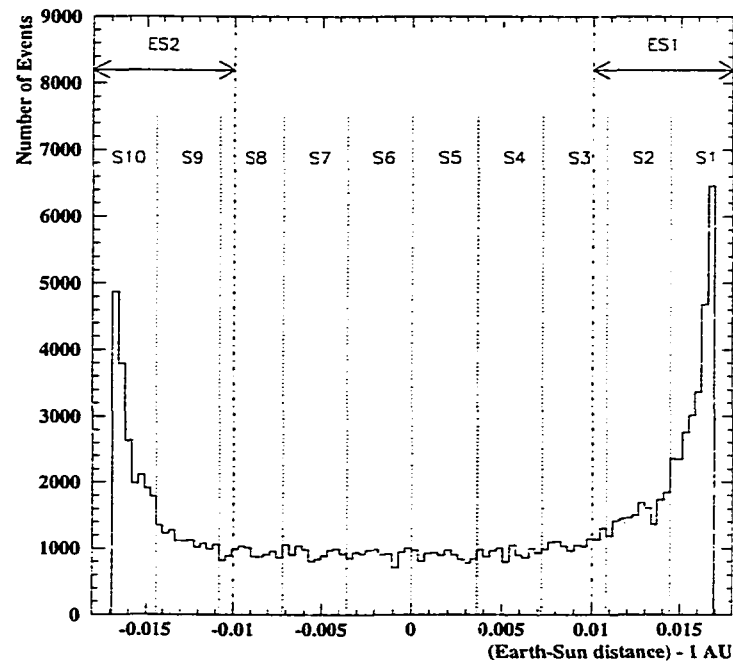


Figure 7.8: Definition of the seasonal bins based on the Earth-Sun distance. The extended bins ES1 and ES2 are used to measure the seasonal flux asymmetry. Also shown is the distribution of the final sample events in Earth-Sun distance (histogram).

Table 7.3: Definition of seasonal subsets.

Subset	ΔR (Earth-Sun dist - 1.0) (AU)	Livetime (days)	$\langle \frac{1}{r^2} \rangle$
S1	0.0180 – 0.0144	192.29	0.9689
S2	0.0144 – 0.0108	116.42	0.9751
S3	0.0108 – 0.0072	84.23	0.9822
S4	0.0072 – 0.0036	70.79	0.9892
S5	0.0036 – 0.0000	66.62	0.9964
S6	0.0000 – -0.0036	70.11	1.0036
S7	-0.0036 – -0.0072	75.06	1.0109
S8	-0.0072 – -0.0108	70.86	1.0183
S9	-0.0108 – -0.0144	87.40	1.0259
S10	-0.0144 – -0.0180	146.58	1.0326
ES1	0.0180 – 0.0100	329.25	0.9718
ES2	-0.0100 – -0.0180	248.89	1.0295

corrections for seasonal and day/night subsets for the eccentricity are listed in Tables 7.2 and 7.3.

7.2 Error Analysis

When making measurements of this kind, errors must be taken into consideration. First, the statistical errors associated with the signal extraction method are considered. Second, the systematic errors for the flux, spectrum, day/night and seasonal measurements are considered.

7.2.1 Statistical Errors

Since the time-smeared non-flat background corrections used in the signal extraction method are small, the statistical errors are determined by the first order signal extraction. The first order signal is simply a count of the number of events in each region (R_1 and R_2), and \sqrt{N} errors are taken. The resulting statistical error for the signal extraction method is:

$$\sigma_{sig} = \sqrt{N_2 + \xi^2 N_1} \quad (7.11)$$

where ξ is defined as in Eqn 7.9. For the case when the cut bin is set to $y = 30$ ($\cos\theta_{sun} = 0.5, \xi = \frac{1}{3}$), this is simply:

$$\sigma_{sig} = \sqrt{N_2 + \frac{N_1}{9}} \quad (7.12)$$

The correction for angular cut efficiencies (ϵ') also increases these statistical errors by:

$$\sigma'_{sig} = \frac{\sigma_{sig}}{\epsilon'}. \quad (7.13)$$

7.2.2 Systematic Errors for Flux and Energy Spectrum

7.2.2.1 Absolute Energy Scale Error

Given the steeply falling nature of the recoil electron spectra (see Figure 5.5), a high level of accuracy in the absolute energy scale of the detector is required to make meaningful flux measurements. Any uncertainty in the knowledge of the energy scale is amplified by the shape of the recoil electron spectra. The LINAC calibration is used to set the absolute energy scale of the detector (as shown in Figure 3.13), as well as determine the uncertainty of the energy scale.

The 1σ total errors of the LINAC energy scale determination are used in determining the systematic error that the absolute energy scale error introduces in the flux and spectrum measurements. The events in the ^8B MC sample are used to evaluate the effects of this uncertainty. Each LINAC calibration energy point is taken to represent the range of energies surrounding that point. The energies of events in the MC sample are separately shifted by the $+1\sigma$ and -1σ amounts based on the LINAC energy scale total error. A shifted energy is determined by:

$$E_{shift} = E(1 + \sigma_{E-scale}^{\pm}(E)) \quad (7.14)$$

where E is the true reconstructed energy and $\sigma_{E-scale}^{\pm}$ is the 1σ error for that reconstructed energy. The measured fluxes from the energy shifted samples are compared to the un-shifted flux and the flux differences are taken to be the systematic errors. This absolute energy scale error contributes a systematic error of $^{+1.0\%}_{-0.7\%}$ to the overall solar neutrino flux measurement.

For the measurement of the energy spectrum, the effects of the energy scale uncertainty are measured in 5 energy bins of 2.0 MeV width, instead of the usual 18 bins. This is done to reduce the effects of bin-to-bin fluctuations dominating the observed flux differences at higher energies where statistics of the ^8B are lower. Again, the energies of events in the MC sample are shifted according to the LINAC $\pm 1\sigma$ total errors and the shifted 5 bin spectra are compared to the un-shifted spectrum. The deviation in the spectrum from the $+1\sigma$ and -1σ shifts are shown in Figure 7.9. The resulting flux differences from $+1\sigma$ and -1σ are averaged, again to help reduce some remaining effects of fluctuations, and the resulting flux differences in each bin are shown in Table 7.4. These points are fit with a linear function and this fitted function is used to determine the $\pm 1\sigma$ absolute energy scale systematic error for all 18 energy spectral bins. This fitted function is:

$$\sigma_{E-scale}^{\pm} = -1.975 + E(0.3590)(\%) \quad (7.15)$$

The systematic error values assigned to each energy bin are listed in Table 7.7.

7.2.2.2 Position and Direction Dependence of Energy Scale

The DTG data are used to measure the position and direction dependence of the energy scale (see Section 3.5). Any position and direction dependence will also introduce errors in the measured flux of solar neutrinos. To evaluate

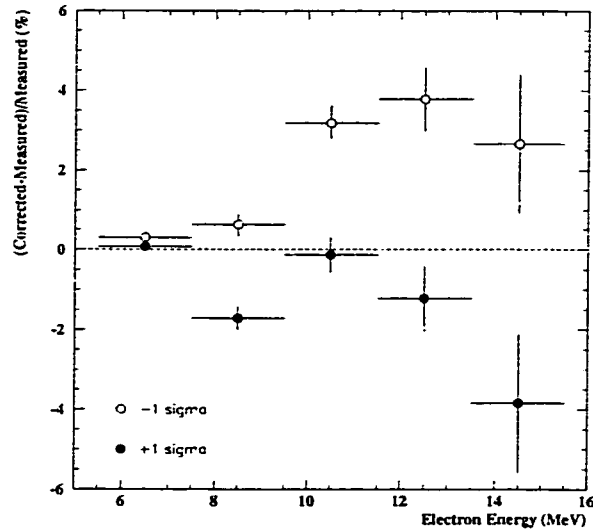


Figure 7.9: The deviation $((\text{Corrected-Measured})/\text{Measured})$ for the energy spectrum for the $+1\sigma$ and -1σ absolute energy scale shifts. The results from $+1\sigma$ and -1σ are then averaged to reduce the effects of bin-to-bin fluctuations.

Table 7.4: Absolute energy scale flux errors for the measurement of the spectrum in 5, 2.0MeV wide bins.

Energy Range (MeV)	Error in measured flux due to energy scale uncertainty (%)
5.5 – 7.5	± 0.2
7.5 – 9.5	± 0.5
9.5 – 11.5	± 1.7
11.5 – 13.5	± 2.5
13.5 – 20.0	± 3.3

these errors, the ^8B MC sample is used. The measured position and direction dependence of the energy scale are independently used to shift the measured energies of MC events:

$$E_{\text{shift}} = E(1 + F_{\text{shift}}), \quad (7.16)$$

where F_{shift} is determined based on the reconstructed vertex or direction for each event. For the value of F_{shift} for the position dependence, the DTG energy scale position dependence shown in Figure 3.24 is used. The value of F_{shift} is obtained by summing the energy scale difference from the reconstructed r and z values to find the total energy scale difference based each event's position. In a similar manner, the reconstructed direction is used to find an F_{shift} value based on the DTG energy scale direction dependence as shown in Figure 3.25.

For the flux measurement, energies of MC events are shifted according to this prescription and the resulting change in the measured flux is taken to be the systematic error. A $\pm 0.2\%$ flux systematic error is found from the energy scale position dependence, and a $\pm 0.1\%$ flux systematic error is found for the energy scale direction dependence.

In the measurement of the recoil electron spectrum, the position and direction dependence of the energy scale has been corrected for in the measured MC spectrum. These corrections are determined using the ^8B MC sample and the results from the DTG in a manner similar to the error evaluation for the flux.

Each event in the MC sample has its energy value shifted based on the DTG energy scale position or direction dependence, and the spectrum, again

plotted in 5, 2.0 MeV bins, is compared to the unshifted spectrum. The deviation in the spectrum $((\text{Corrected-Measured})/\text{Measured})$ for each 2.0 MeV bin is calculated, as shown in Figure 7.10. These deviations as a function of energy are fit with a line, and these fitted linear functions are used to find the correction for each of the 18, 0.5 MeV energy bins in the MC energy spectrum. The fitted functions are also shown in Figure 7.10. Both corrections are applied to the measured MC energy spectrum. The systematic error of this correction, applied to all bins of the energy spectrum, is determined by taking the maximum difference between the measured deviation in the energy spectrum and the linear function at any point. For both direction and position energy scale dependence, this systematic error is $\pm 0.5\%$.

7.2.2.3 Energy Resolution Systematic Error

The energy resolutions measured by the LINAC are 1.5% larger than the corresponding resolutions from the LINAC MC simulation, independent of the electron energy (see Figure 3.15). For a given input electron energy, this will result in a wider reconstructed energy distribution for data than for the MC simulation. When this is combined with the shape of the recoil electron input energy distribution, this difference in energy resolution will lead to differences in the measured flux. In order to evaluate the effect of this difference, energies of the ^8B MC sample were changed according to the following prescription and the flux differences measured:

$$E_{\text{shift}} = E(1 + \Delta_{\text{res}}). \quad (7.17)$$

where:

$$\Delta_{\text{res}} = 0.015 \times \sigma_{\text{data}} G_{\text{ran}}$$

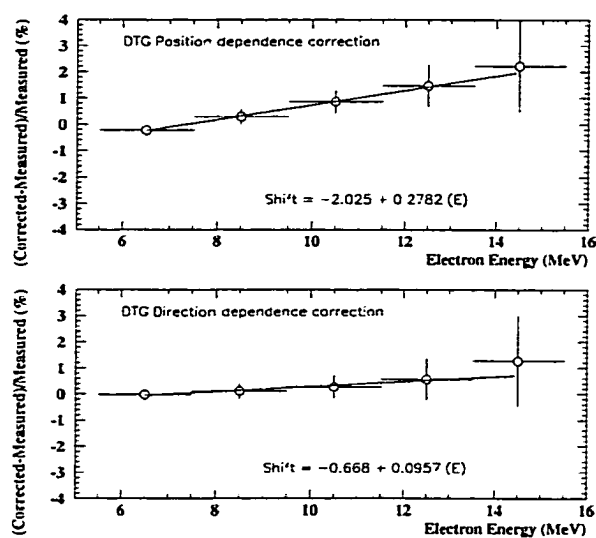


Figure 7.10: Corrections applied to the measured MC spectrum from the position (upper) and direction (lower) dependencies of the energy scale as measured by the DTG. The systematic error for these corrections is taken as the maximum deviation of the measured points from the fit line, in each case $\pm 0.5\%$.

σ_{data} = Energy resolution of data measured by LINAC

G_{ran} = A Gaussian random number with standard deviation of 1.0

The flux from this shifted MC sample was measured and compared to the unshifted flux and the flux difference is taken as the measure of the systematic error in the solar neutrino flux measurement. This energy resolution difference introduces a flux difference of less than 0.1%, so $\pm 0.1\%$ is taken as the systematic error for the flux measurement.

The effects of the energy resolution difference on the measurement of the spectrum is again done in 5, 2.0 MeV wide bins to reduce the bin-to-bin fluctuations. The maximum deviation in any bin, -0.3%, is taken as the systematic error for all bins. Therefore, the systematic error for each spectral bin from the energy resolution difference is $\pm 0.3\%$.

7.2.2.4 Angular Cut systematic

Angular resolution is another quantity in which the LINAC data and MC simulation do not exactly agree, with variations at all energies being less than $\pm 3\%$ (see Figure 3.14). Since the angular cut efficiencies are measured using ^8B MC data, this difference would lead to a systematic difference in these efficiencies and, therefore, in the measured flux. To evaluate the effects of this difference, the $\cos\theta_{sun}$ values for the MC simulation are changed:

$$\cos\theta'_{sun} = \frac{\cos\theta_{sun} + \Delta}{1 + \Delta} \quad (7.18)$$

where Δ is taken to be +3% and -3%. The angular cut efficiencies are recalculated using these new modified MC samples and the flux differences induced by these changes are taken as the systematic error resulting from the angular resolution difference. For the flux measurement, a systematic error

of $^{+0.6\%}_{-0.5\%}$ is found. The systematic errors found for the electron spectrum measurement are listed in Table 7.7.

7.2.2.5 ^8B Spectral Shape Error

The uncertainty in the shape of the ^8B input neutrino energy spectrum will introduce an energy dependent error in the spectrum of solar neutrinos, as well as an error in the measured flux since the measurement is performed above a fixed energy threshold. The shape for the ^8B neutrino spectrum provided[37] includes 3σ errors, and is shown in Figure 5.2. These 3σ errors are divided by 3 to obtain 1σ errors.

To evaluate the effects on the flux and spectrum measurements of this spectrum shape uncertainty, a simple MC study was performed. Recoil electrons energies were generated based on the ^8B spectral shape (as well as the $\pm 1\sigma$ shapes) and these electron energies were artificially smeared by a random amount based on the measured energy resolution of the detector from the LINAC calibration. This was repeated 10 million times for each spectral shape. These electron samples were used to calculate a flux and spectrum. The flux and spectrum differences between the best ^8B spectral shape and the $\pm 1\sigma$ spectral shapes were taken as the systematic error. For the flux measurement, a systematic error of $^{+1.0\%}_{-1.1\%}$ is assigned. The systematic errors for the electron spectrum measurement are summarized in Table 7.7.

7.2.2.6 Other sources of Systematic Error

There are other systematic errors that introduce uncertainties into the measurement of the flux and spectrum. These include:

- uncertainty in the neutrino-electron cross section
- uncertainty in the flasher cut
- vertex shift error
- uncertainty in the spallation dead time
- uncertainty in the livetime
- uncertainty in the noise cuts
- uncertainty in the trigger efficiency
- uncertainty in the non-flat background correction

Uncertainty in the neutrino-electron scattering cross section (see Section 5.1.1) introduces errors in the expected flux and spectrum of solar neutrinos. These uncertainties, affecting both the magnitude and energy dependence of the cross section, are taken directly from Reference [38], and are $\pm 0.5\%$ for both flux and spectrum measurements.

The flasher cut is designed to remove events originating from flashing PMT tubes (see Section 6.1.1), and the efficiency for saving real neutrino events is high. The efficiency for saving events is measured using the nickel-californium calibration data and using the MC simulation of nickel-californium data. Any difference in these efficiencies would directly affect the measured flux. The difference in these efficiencies is taken as the systematic error for the flasher cut and is set to $\pm 0.2\%$, both for the measurement of the flux and spectrum.

The vertex shift systematic error arises from a systematic shift between the reconstructed vertex position of nickel-californium data and MC data near the edge of the fiducial volume. This shift induces differences in the real and simulated fiducial volumes, and therefore in the measurement of the solar neutrino flux and spectrum. For the flux measurement, a systematic fiducial volume difference of +1.5% is found, while the energy dependence of this difference is found to be +0.4%. The positive sign of this error is indicative of the larger fiducial volume found for data when compared to MC.

The dead time from the spallation cut (see Section 6.1.2) is set to be 21.1% and event rates for the MC are corrected for this dead time. The variation of this value, determined by looking at subsets of the data, is then taken as the systematic error in the measurement of the solar neutrino flux. That variation is at most $\pm 0.1\%$, so this value is taken as the systematic error.

The number of solar neutrino events is normalized by the detector livetime to obtain an event rate. The livetime is normally calculated using the summary information from the online data acquisition system. If the day and time information from each event is used instead to measure the livetime, a 0.1% difference is found, so a systematic error in the measurement of the flux is set to $\pm 0.1\%$.

The systematic error due to noise cuts is actually a mixture of errors from three different sources. The noise cuts are a series of cuts in the reduction (see Section 6.1.3) that are designed to reject background events while keeping the

signal events. These cuts include the gamma cut, the clusfit fiducial volume cut, and the new goodness cut. Any difference in the reduction efficiency for these cuts between real data and simulated MC events must be taken as a systematic error.

The gamma cut systematic arises from the previously mentioned vertex shift near the edge of the tank, as the gamma cut is another, somewhat modified, fiducial volume cut. Since the gamma cut rejects events that appear to be originating from a wall of the detector, only a fraction of the events are effected, and the impact of the vertex shift is reduced. An evaluation of the measured vertex shifts combined with the gamma cut is used to measure a systematic error to $\pm 0.2\%$ for the flux measurement and all spectral bins, except for the 5.5-6.5 MeV bin, where it is $\pm 0.5\%$.

The clusfit fiducial volume cut is evaluated by comparing the reduction efficiency of nickel-californium data and MC data. The efficiency difference of $\pm 0.7\%$ is taken as the systematic error for the flux and spectrum measurement.

The new goodness cut is evaluated using events which are tagged as likely spallation events in the reduction. This sample is composed of the beta decay events of spallation products produced by through-going muons, and are distributed uniformly throughout the detector volume and are isotropic in direction. The efficiency difference for spallation data and an MC sample of spallation data when the new goodness cut is applied is then taken as the systematic error. For the flux measurement and energy bins 6.5 MeV and higher, the systematic error is determined to be $\pm 0.6\%$. In the lower energy

bins, it is slightly larger, $^{+2.2\%}_{-0.8\%}$ for the 6.0-6.5 MeV bin and $^{+2.6\%}_{-0.9\%}$ for the 5.5-6.0 MeV bin.

The knowledge of the trigger efficiency as a function of energy is the next systematic error considered. The trigger efficiency is measured as a function of energy and position using a combination of DTG data and nickel-californium data (see Section 3.6) The trigger is also simulated using a software trigger simulation. This simulation is applied to the MC DTG and nickel-californium data. The difference between the measured and simulated trigger efficiencies are taken as systematic errors. For the measurement of the flux, a systematic error of $+0.2\%$ is assigned. For the measurement of the energy spectrum, the two energy bins near threshold have larger uncertainties, and $+0.4\%$ and $+2.1\%$ are assigned to the 6.0-6.5 MeV and 5.5-6.0 MeV energy bins, respectively. The positive sign of this error is indicative of the better trigger efficiency observed for real data events.

The calculation of the time-smeared non-flat background has also been evaluated to test for systematic errors in measurement of the solar neutrino flux. In order to evaluate the size of this systematic error, a background that was truly non-flat in the geometry of the detector was artificially added to the final sample of neutrino events, and the signal extraction was repeated. The size of this added background was made to be the same size as the change in flux due to the non-flat background ($\sim 1\%$). Any change in the measured flux from this extra background is taken as the systematic error for the non-flat background procedure. For the measurement of the flux and spectrum, a maximum flux difference of $\pm 0.3\%$ is found and taken as the systematic error of the non-flat background determination.

Table 7.5: Summary of systematic errors from solar neutrino flux measurement.

Source of Flux Systematic Error	Error (%)
^8B spectral shape	+1.0/-1.1
Neutrino-Electron Cross Section	± 0.5
Angular Cut systematic	+0.6/-0.5
Absolute Energy Scale Error	+1.0/-0.7
Energy Scale Position Dependence	± 0.2
Energy Scale Direction Dependence	± 0.1
Energy Resolution	± 0.1
Non-Flat Background	± 0.3
Flasher Cut	± 0.2
Vertex Difference	± 1.5
Spallation Dead time	± 0.1
Livetime	± 0.1
Noise Cuts	+0.9/-0.6
Trigger Efficiency	+0.2
Total Flux Systematic Error	+2.4 -1.6

7.2.2.7 Total Systematic Error for Flux Measurement

When determining the absolute flux of solar neutrinos originating in the Sun, the systematic errors from different cuts and sources are taken as uncorrelated, and are added in quadrature. For the measurement of the solar neutrino flux, the systematic errors are summarized in Table 7.5.

7.2.2.8 Total Systematic Error for Spectrum Measurement

Since the measurement of the spectrum is only concerned with the shape of the electron spectrum, only the relative error between energy bins is considered, or in the case of errors where the energy dependence is not well understood, the total systematic error is taken as the relative systematic

Table 7.6: Summary of non-energy dependent systematic errors from solar neutrino spectrum measurement.

Source of Energy Spectrum Systematic Error	Error (%)
Neutrino-Electron Cross Section	± 0.5
Energy Scale Position Dependence	± 0.5
Energy Scale Direction Dependence	± 0.5
Energy Resolution	± 0.3
Non-Flat Background	± 0.3
Flasher Cut	± 0.2
Vertex Difference	± 0.5
Spallation Dead time	± 0.1
Livetime	± 0.1
Noise Cuts	+0.9/-0.6 (6.5-20.0)
	+2.4/-0.9 (6.0-6.5)
	+2.7/-1.0 (5.5-6.0)
Trigger Efficiency	+0.4 (6.0-6.5)
	+2.1 (5.5-6.0)
Total Non-energy Dependent Spectrum Systematic Errors	+1.4/-1.3 (6.5-20.0)
	+2.7/-1.4 (6.0-6.5)
	+3.6/-1.5 (5.5-6.0)

error. Systematic errors which are not (or only slightly) energy dependent are summarized in Table 7.6. These errors are then added to the energy dependent errors, which are summarized, along with total errors, in Table 7.7. Again, all errors are combined in quadrature.

7.2.3 Day/Night and Seasonal Systematic Errors

The systematic errors are somewhat simplified when making measurements of relative flux differences between different subsets of the data. Here many of the systematic errors will cancel, since the same effects would be expected in all subsets of data, and the flux difference would remain unaffected.

Table 7.7: Summary of energy dependent systematic errors from solar neutrino spectrum measurement as well as the total systematic errors from each bin, which includes the non-energy dependent portion from Table 7.6.

Energy Bin (MeV)	Angular Cut Error (%)	Absolute Energy Scale Error (%)	^8B Spectrum Shape Error (%)	Total Error (%)
5.5-6.0	+0.2/-1.1	± 0.1	+0.3/-0.2	+3.6/-1.8
6.0-6.5	+0.7/-0.6	± 0.3	+0.4/-0.4	+2.8/-1.5
6.5-7.0	+0.7/-0.7	± 0.5	+0.6/-0.6	+1.7/-1.5
7.0-7.5	+1.7/-0.5	± 0.6	+1.3/-0.8	+2.6/-1.6
7.5-8.0	+0.6/-0.6	± 0.8	+1.2/-0.8	+2.1/-1.7
8.0-8.5	+0.6/-0.5	± 1.0	+0.9/-1.2	+2.0/-2.0
8.5-9.0	+0.5/-0.5	± 1.2	+1.5/-1.4	+2.4/-2.2
9.0-9.5	+0.5/-0.4	± 1.4	+1.6/-1.6	+2.6/-2.4
9.5-10.0	+0.4/-0.4	± 1.5	+2.1/-2.1	+3.0/-2.8
10.0-10.5	+1.1/-0.4	± 1.7	+2.1/-2.2	+3.2/-3.0
10.5-11.0	+0.4/-0.4	± 1.9	+2.4/-3.2	+3.4/-3.9
11.0-11.5	+0.3/-0.3	± 2.1	+3.1/-3.2	+4.0/-4.0
11.5-12.0	+0.3/-0.3	± 2.2	+2.9/-3.5	+3.9/-4.3
12.0-12.5	+0.4/-0.3	± 2.4	+3.9/-4.0	+4.9/-4.9
12.5-13.0	+0.3/-0.4	± 2.6	+4.5/-4.2	+5.4/-5.1
13.0-13.5	+0.3/-0.3	± 2.8	+6.1/-5.3	+6.8/-6.1
13.5-14.0	+0.4/-0.4	± 3.0	+5.4/-7.0	+6.3/-7.7
14.0-20.0	+0.3/-0.4	± 3.1	+6.7/-7.7	+7.6/-8.4

Therefore, only systematic errors that contribute to the measured flux difference between two run periods are considered. These include time and direction dependence of the relative energy scales, errors that affect the livetime calculation, and differences in the non-flat background calculation between different subsets of the data.

7.2.3.1 Relative Energy Scale

To evaluate the relative energy scale between different run periods, for example between day and night, or between data in the S1 and S8 seasonal bins, a calibration source is required that is continually collected along with solar neutrinos. To fulfill this need, the spallation data are used. This sample is composed of the beta decay events of spallation products produced by through-going muons, which are distributed uniformly throughout the detector volume and are isotropic in direction. These spallation events are chosen (see Section 6.1.2) to be events with a high likelihood as being spallation events ($\log(\textit{Likelihood}) > 0.98$) and are located within 300 cm and 0.1 sec of the through-going muon track that gave the high likelihood value. While the composition of this sample is not well understood, there is no reason to expect a time dependence in the composition. Therefore, it is well suited for making relative studies of the energy scale. The energy distribution of this sample is presented in Figure 7.11

The relative energy scale of SK is checked by measuring the mean of the spallation event energy distribution for those events that which have $\cos\theta_{sun} \geq 0.5$, based on the reconstructed direction relative to the location of the Sun at the time of each event. Since the time and direction of each

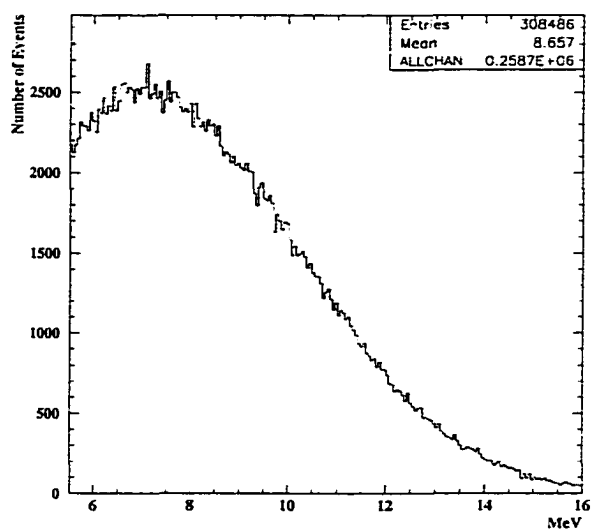


Figure 7.11: Energy distribution of events identified as likely spallation events. The mean of this distribution is used as the measure of the energy of these events

spallation event is assumed to be uncorrelated with energy, every spallation event is used 100 times, each time with a different randomly chosen time of day on the date of that event. This changes the location of the Sun, giving a different value of $\cos\theta_{sun}$. and allows the same spallation event to sample different times of the day and different values of $\cos\theta_{sun}$. This time smearing is only done over a single day, and not over the entire livetime, so that energy scale differences from long term variations in the detector can be detected. For each subset of data, events that fall into a day/night or seasonal bin and have $\cos\theta_{sun} \geq 0.5$ are histogrammed accordingly, and the mean of each subset's histogram is compared to the mean of the entire distribution. This entire procedure is repeated again, this time events with $\cos\theta_{sun} \leq -0.5$, corresponding to events originating from the "anti-Sun" location, are used. The anti-Sun should exhibit similar systematic effects, if any, as the true Sun direction and serves as an additional cross check of the relative energy scale. The measured means of the spallation samples for each subset are shown in Table 7.8.

Since some oversampling is used in generating the energy distributions of spallation events for each subset of data, the statistical error of the mean is not easily known, yet trying to determine the significance of these mean energy measurements requires this knowledge. To determine the statistical error of the mean energies listed in Table 7.8, the same spallation analysis is repeated, this time with the spallation event energies replaced with energies from a known Gaussian energy distribution, with a known mean, that is similar to the energy distribution shown in Figure 7.11. This procedure is

Table 7.8: Measured spallation sample energy distribution means for each subset of data used in the day/night and seasonal flux subsets. These mean values are generated by oversampling the spallation sample (see text), and the errors shown are determined considering this oversampling.

Data Subset	Mean of Sun	Mean of Anti-Sun
All Day	8.660 ± 0.007	8.656 ± 0.007
All Night	8.654 ± 0.007	8.654 ± 0.007
N1	8.663 ± 0.013	8.654 ± 0.013
N2	8.652 ± 0.013	8.649 ± 0.013
N3	8.671 ± 0.013	8.662 ± 0.013
N4	8.643 ± 0.013	8.647 ± 0.013
N5	8.639 ± 0.013	8.642 ± 0.013
S1	8.687 ± 0.013	8.663 ± 0.013
S2	8.654 ± 0.013	8.644 ± 0.013
S3	8.631 ± 0.013	8.628 ± 0.013
S4	8.634 ± 0.013	8.629 ± 0.013
S5	8.658 ± 0.013	8.663 ± 0.013
S6	8.654 ± 0.013	8.644 ± 0.013
S7	8.668 ± 0.013	8.672 ± 0.013
S8	8.666 ± 0.013	8.674 ± 0.013
S9	8.637 ± 0.013	8.639 ± 0.013
S10	8.654 ± 0.013	8.666 ± 0.013
ES1	8.676 ± 0.013	8.656 ± 0.013
ES2	8.649 ± 0.013	8.652 ± 0.013

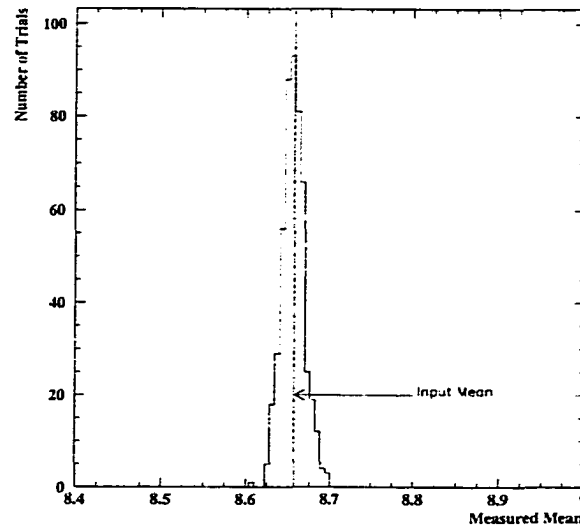


Figure 7.12: Distribution of measured means for a known input mean value. This is used to measure the statistical error of the spallation mean energies used for the relative energy scale check.

repeated several times, and the distribution of measured means is found. The width of the distribution of measured means about the known input mean is then used as the measure of the statistical error of each mean measured using real data. Figure 7.12 presents the distribution of measured means for the N1-N5 data subsets resulting from a known energy distribution with a mean of 8.657.

The systematic error from the relative energy scale differences are evaluated independently for the all day/night, the 5 bins of day/night, and the seasonal flux bins. For each set of flux bins, the maximum deviation found from the mean of the entire sample (8.657) for any subset of data (Sun or anti-Sun) is taken as the systematic difference in relative energy scales for

all subsets. If all measured means for the spallation events are within the statistical error of the measurement for all subsets in a group, then the statistical error of the measurement is taken as the systematic error in the mean energies for all subsets.

To verify the measured mean energy will accurately reflect shifts in the relative energy scales, the true energies of all spallation events were artificially shifted by $\pm 2\%$ and the mean energy found again. Since the mean energy is calculated over a restricted energy range, the $\pm 2\%$ shift in energy only results in a $\pm 1.25\%$ shift in the mean. Therefore, all measured mean shifts are multiplied by a factor of 1.6 ($= \frac{2.0\%}{1.25\%}$) to obtain the energy scale shift from the shift in mean energies.

The relative energy scale systematic differences are determined to be $\pm 0.1\%$ for the difference between the all day/night flux measurements, $\pm 0.3\%$ for the D1-D5 and N1-N5 subset flux measurements, and $\pm 0.5\%$ for the seasonal subset flux measurements. These energy scale differences are then evaluated with the ^8B MC sample to determine the systematic error in the relative flux measurement using the same procedure that was used to determine the systematic error in the flux from the absolute energy scale error. For the all day/night measurement, a $\pm 0.2\%$ relative flux systematic error is assigned. For the D1-D5 and N1-N5 subset measurements, a $\pm 0.5\%$ relative flux systematic error is assigned. For the seasonal subset measurements, a $\pm 0.7\%$ relative flux systematic error is assigned.

7.2.3.2 Other Relative Errors

Systematic errors which affect the calculation of the lifetime of the detector are also applied to these measurements, as these errors could affect

any subset of the data. This contributes a $\pm 0.1\%$ uncertainty for livetime calculation as well as a $\pm 0.1\%$ uncertainty from spallation dead time to the measured relative fluxes in all day/night and seasonal subsets. These are the same errors applied to the flux and spectrum measurement.

The time-smeared non-flat background correction is again evaluated by adding a non-flat component to the background and measuring the change in the flux for each subset. For the day/night and seasonal subsets of data, the non-flat background corrections are slightly larger, since the Sun samples smaller regions of the background in SK detector coordinates, and this leads to a larger systematic error in the relative flux from this correction, $\pm 0.4\%$.

The day/night subsets of data also require a systematic error to take into account a small directional asymmetry in the efficiency of the flasher cut. This introduces a $\pm 0.1\%$ systematic error for the day/night measurements only. The seasonal flux subsets have almost equal exposure of day and night, and are not affected by this asymmetry.

Since the seasonal flux bins do not sample the detector livetime evenly with respect to different trigger conditions present in the final sample (see Section 2.6.3), a $\pm 0.2\%$ systematic error is assigned. This error arises from the flux differences measured under different trigger conditions during the livetime in the data sample. The day/night bins have almost equal exposure in each run period, and are not affected by this efficiency difference.

7.2.3.3 Total Day/Night Systematic Errors

The systematic errors contributing to the measurement of the day/night flux difference are summarized in Table 7.9. Listed are total systematic

Table 7.9: Summary of day/night systematic errors. Listed separately are the systematic errors for the D1-D5 and N1-N5 subsets and the total day/night subsets.

Source of Day/Night Systematic Error	N1-N5/D1-D5 Error (%)	All Day/Night Error (%)
Relative Energy Scale	± 0.5	± 0.2
Spallation Dead time	± 0.1	± 0.1
Livetime	± 0.1	± 0.1
Flasher Cut	± 0.1	± 0.1
Non-Flat Background	± 0.4	± 0.4
Total Systematic Error	± 0.7	± 0.5

Table 7.10: Summary of seasonal systematic errors. These errors apply to the S1-S10 bins, as well as the ES1-ES2 bins.

Source of Seasonal Systematic Error	Error (%)
Relative Energy Scale	± 0.7
Trigger Efficiency	± 0.2
Spallation Dead Time	± 0.1
Livetime	± 0.1
Non-Flat Background	± 0.4
Total Systematic Error	± 0.9

errors for both the D1-D5 and N1-N5 data subset measurements and the total day/night flux difference.

7.2.3.4 Total Seasonal Systematic Errors

The systematic errors contributing to the seasonal flux measurements are summarized in Table 7.10. The total systematic error for each relative flux measurement are also shown. These errors apply to both the S1 to S10 seasonal bins and to the ES1-ES2 extended bins.

CHAPTER 8

RESULTS AND ANALYSIS

8.1 Measurement Results

Now that a signal extraction method and errors have been established (see Chapter 7), the results of the solar neutrino measurements are presented. First, the results of the flux measurement are presented, followed by the measured recoil electron spectrum, and day/night and seasonal flux measurements. Each of these results are presented with the corresponding result from the simulation of the BP98 solar neutrino flux (see Chapter 5).

In order to look for flux-independent evidence of neutrino oscillations, the variation in the day/night and seasonal flux differences and the shape of the recoil energy spectrum are examined using a χ^2 analysis. The measured results are also used to examine the allowed parameter regions (in Δm^2 and $\sin^2 2\theta$) under a neutrino oscillation hypothesis.

8.1.1 Measured Solar Neutrino Flux

The solar neutrino extraction method, including the corrections for a non-flat background and angular cut efficiency, found 15,252 recoil electron events between 5.5-20 MeV resulting from the interaction of solar neutrinos (see Section 7.1.3). To perform a comparison between this result and the result of the solar neutrino MC simulation, the number of extracted events is normalized by the livetime, giving the measured rate of solar neutrino events (events/day). The livetime of the final sample is 980.36 days. This results in

a solar neutrino event rate (5.5-20.0 MeV) in the 22.5 kton fiducial volume of:

$$\text{Rate of Data} = 15.56 \pm 0.31(\text{stat.}) \text{ events/day}$$

The corresponding rate from the MC simulation of the BP98 solar neutrino flux is:

$$\text{Rate of MC} = 33.96 \pm 0.02(\text{stat.}) \text{ events/day}$$

These results yield a ratio of measured to expected data rates, including statistical and systematic errors (from Table 7.5), of:

$$\frac{Data}{SSM_{BP98}} = 0.458 \pm 0.009(\text{stat.})^{+0.011}_{-0.007}(\text{sys.})$$

Since the BP98 MC events were generated with an input neutrino flux of:

$$\Phi_{MC}^{BP98} = 5.152 \times 10^6 / \text{cm}^2 / \text{sec},$$

the ratio of measured to expected event rates is used to calculate the measured flux:

$$\Phi_{Data} = 2.36 \pm 0.05(\text{stat.})^{+0.06}_{-0.04}(\text{sys.}) \times 10^6 / \text{cm}^2 / \text{sec}$$

8.1.2 Recoil Electron Spectrum

For the recoil electron spectrum, the number of events found in each energy bin is also normalized by the livetime. The livetime for the 5.5-6.0 and 6.0-6.5 MeV bins is 700.34 days, as the first ~ 280 days were taken without the SLE trigger. For all bins above 6.5 MeV, the livetime is 980.36 days. These different livetime and trigger periods are also reflected in the generation and analysis of the MC data sample. The resulting event rates (events/day) in each energy bin for data are summarized, along with statistical errors, in

Table 8.1. This table also includes the event rates from the BP98 solar neutrino flux for ^8B and hep neutrinos. The measured recoil electron spectrum is shown in Figure 8.1, also showing the total BP98 MC expectations. The total error shown in this figure are obtained by combining the statistical and systematic errors (from Table 7.7) in quadrature. To look for spectral shape deviations, a sign of neutrino oscillations, the ratio of the measured to expected signal rate in each bin is calculated and shown in Figure 8.2. Again, the total errors shown are obtained by combining the statistical and systematic errors in quadrature. The ratio of the measured to the expected spectra are also separately measured during day time and night time periods. The day and night spectra are shown together in Figure 8.3, and are used in the neutrino oscillation analysis.

8.1.3 Day/Night Flux Measurement

The total number of events found in each day/night subset is again normalized by the livetime of each subset. The livetimes for the day/night subsets are summarized in Table 7.2. The resulting event rates, for data and MC samples are summarized, along with statistical errors, for the day/night subsets in Table 8.2. The systematic errors of this relative flux measurement are summarized in Table 7.9. For all subsets of data, the ratio of the measured to expected event rate is calculated, and these results are shown in Figure 8.4, including the total error.

For the all day subset of data, the measured flux is obtained by calculating the ratio of event rates from data to MC:

Table 8.1: Measured fluxes in events/day for the data and the BP98 MC samples (^8B and hep separately) for each energy bin. The ratio of data to MC is obtained using the sum of ^8B and hep MC samples. Errors listed are statistical only.

Energy Bin (MeV)	Data Rate	^8B MC Rate	hep MC Rate $\times 10^{-3}$	$\frac{\text{Data}}{\text{MC}}$
5.5-6.0	2.01 ± 0.25	4.636 ± 0.010	2.63 ± 0.06	0.434 ± 0.053
6.0-6.5	1.93 ± 0.15	4.256 ± 0.010	2.75 ± 0.06	0.453 ± 0.035
6.5-7.0	2.08 ± 0.12	4.679 ± 0.009	3.05 ± 0.05	0.445 ± 0.025
7.0-7.5	1.86 ± 0.11	4.154 ± 0.008	2.74 ± 0.05	0.448 ± 0.026
7.5-8.0	1.63 ± 0.10	3.662 ± 0.008	2.74 ± 0.05	0.445 ± 0.027
8.0-8.5	1.57 ± 0.089	3.099 ± 0.007	2.49 ± 0.05	0.506 ± 0.029
8.5-9.0	1.23 ± 0.077	2.634 ± 0.006	2.49 ± 0.05	0.465 ± 0.029
9.0-9.5	0.960 ± 0.066	2.184 ± 0.006	2.10 ± 0.04	0.439 ± 0.030
9.5-10.0	0.797 ± 0.055	1.774 ± 0.005	2.18 ± 0.05	0.449 ± 0.031
10.0-10.5	0.635 ± 0.045	1.408 ± 0.005	1.82 ± 0.04	0.450 ± 0.032
10.5-11.0	0.541 ± 0.037	1.086 ± 0.004	1.67 ± 0.04	0.497 ± 0.034
11.0-11.5	0.383 ± 0.030	0.819 ± 0.004	1.50 ± 0.04	0.467 ± 0.037
11.5-12.0	0.261 ± 0.024	0.604 ± 0.003	1.13 ± 0.03	0.430 ± 0.040
12.0-12.5	0.224 ± 0.020	0.432 ± 0.003	1.13 ± 0.03	0.517 ± 0.047
12.5-13.0	0.145 ± 0.016	0.302 ± 0.002	0.93 ± 0.03	0.478 ± 0.054
13.0-13.5	0.105 ± 0.013	0.204 ± 0.002	0.84 ± 0.03	0.514 ± 0.064
13.5-14.0	0.089 ± 0.011	0.132 ± 0.001	0.64 ± 0.02	0.669 ± 0.086
14.0-20.0	0.110 ± 0.014	0.205 ± 0.002	2.55 ± 0.05	0.529 ± 0.067

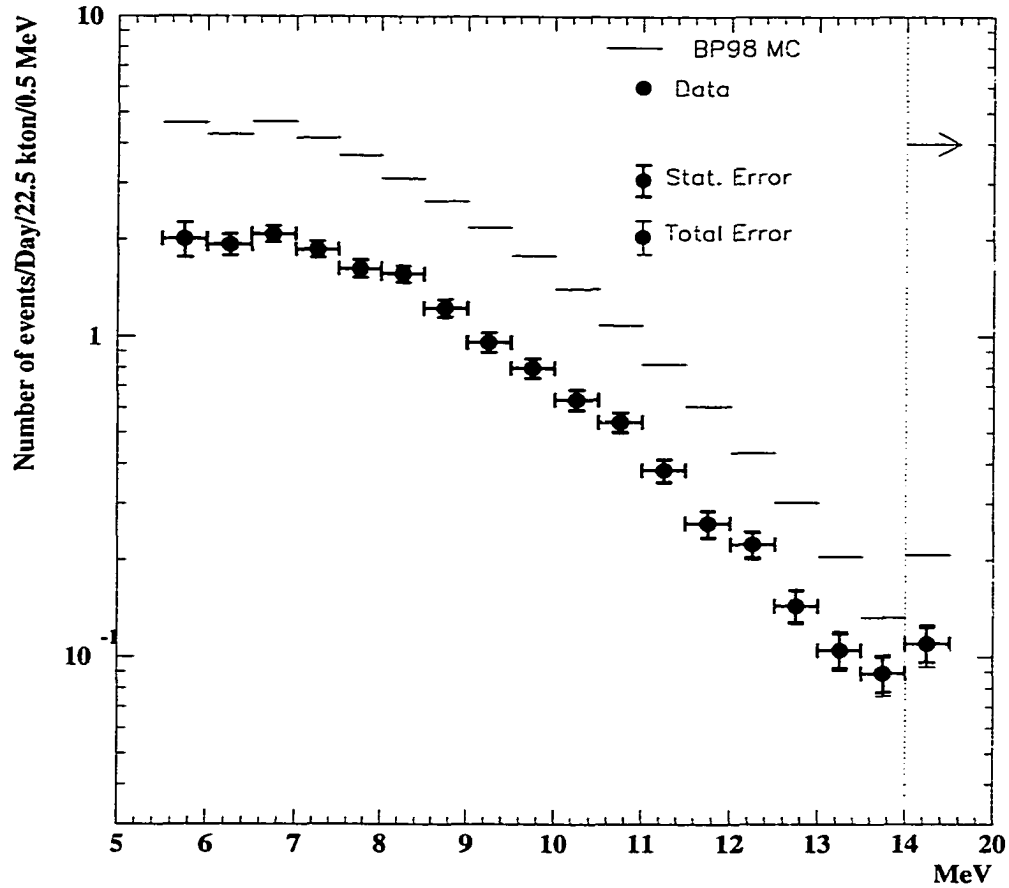


Figure 8.1: The measured solar neutrino recoil electron spectrum. Also presented are the expectations from MC simulation of the BP98 solar neutrino flux. Inner error bars (thick line) represent statistical errors, while the outer error bars (thin line) represent the total errors. Total errors are obtained by combining statistical and systematic errors in quadrature.

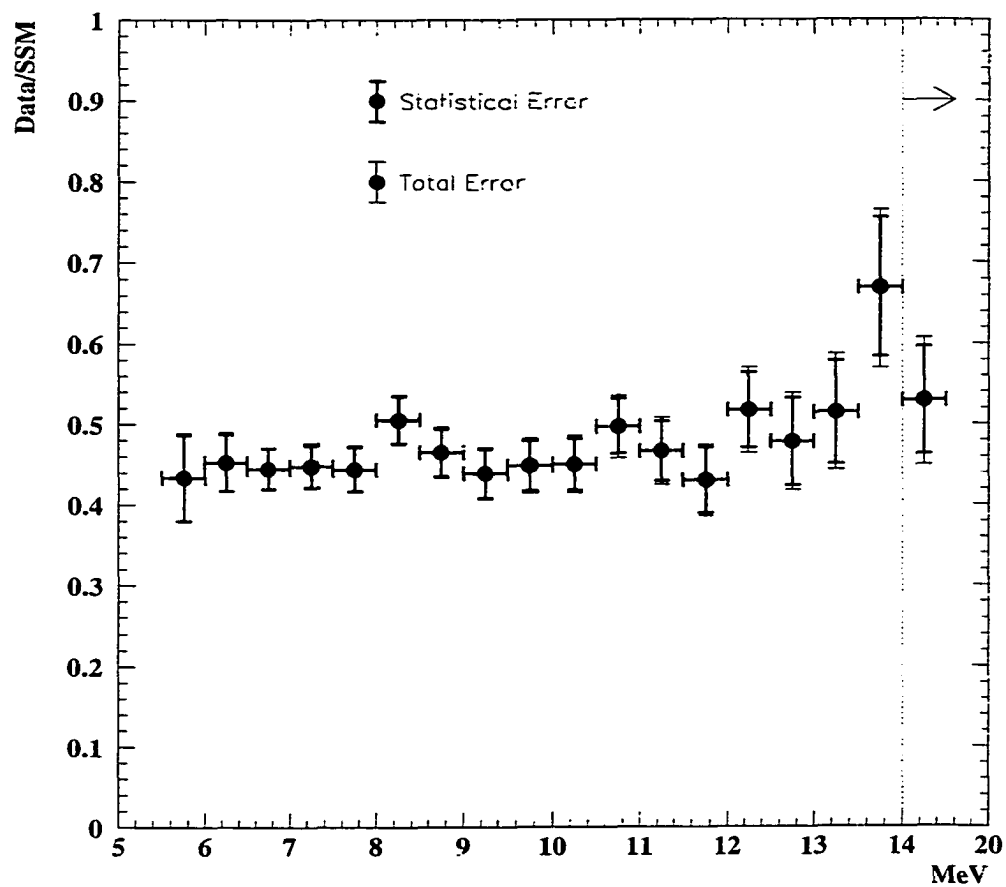


Figure 8.2: The ratio of the measured to the expected recoil electron spectrum. Errors are defined as in Figure 8.1.

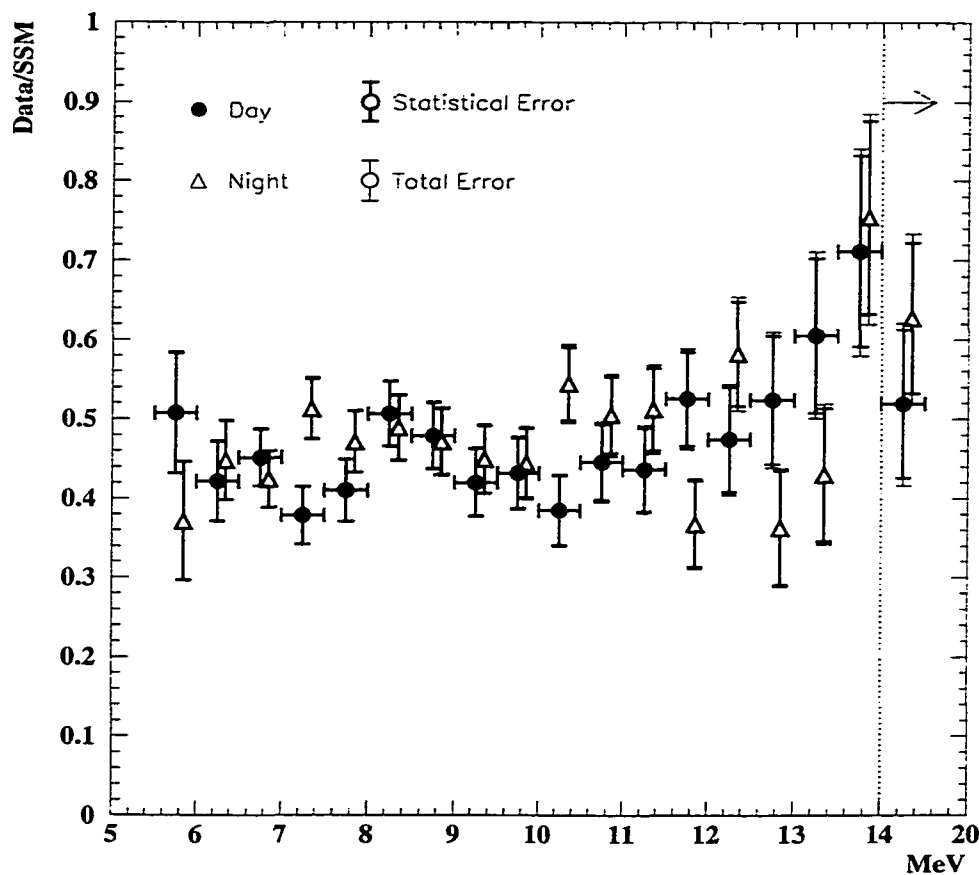


Figure 8.3: The ratio of the measured to the expected recoil electron spectrum as measured during day time and night time periods. Errors are defined as in Figure 8.1.

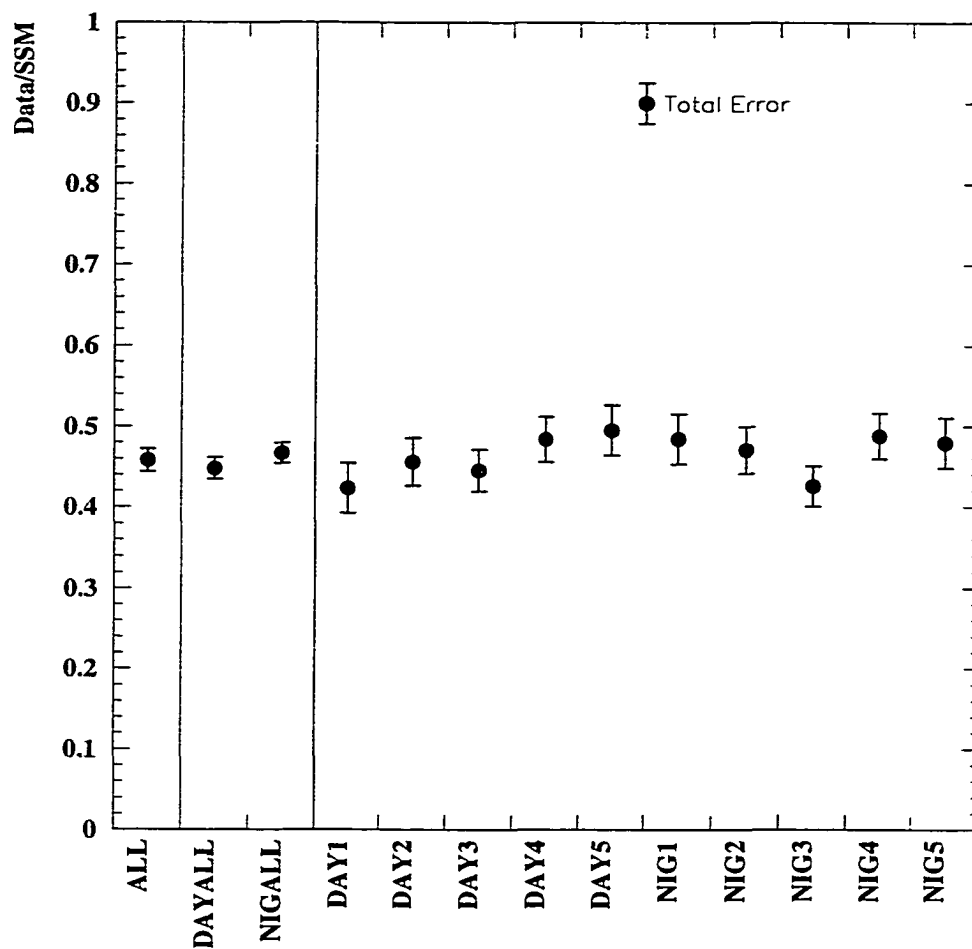


Figure 8.4: Ratio of the measured to expected event rates for all, all day, all night, and the 5 bins of day and night. Total errors presented are obtained by combining the statistical and systematic errors in quadrature. All results include a eccentricity correction to 1 AU.

Table 8.2: Day and night measured fluxes in events/day for the data and the BP98 MC samples. Errors listed for measured rates are statistical only. Subsets are defined in Table 7.2. All results include a eccentricity correction to 1 AU.

Subset	Data Rate	BP98 MC Rate	$\frac{Data}{MC} \pm stat. \pm sys.$
All Day	15.19 ± 0.44	33.89 ± 0.03	$0.448 \pm 0.013 \pm 0.002$
All Night	15.87 ± 0.43	33.99 ± 0.03	$0.467 \pm 0.013 \pm 0.002$
D1	14.24 ± 1.03	33.65 ± 0.08	$0.423 \pm 0.031 \pm 0.003$
D2	15.53 ± 1.00	34.07 ± 0.08	$0.456 \pm 0.029 \pm 0.003$
D3	15.04 ± 0.87	33.78 ± 0.07	$0.445 \pm 0.026 \pm 0.003$
D4	15.47 ± 0.95	34.01 ± 0.07	$0.484 \pm 0.028 \pm 0.003$
D5	16.61 ± 1.04	33.53 ± 0.07	$0.495 \pm 0.031 \pm 0.003$
N1	16.37 ± 1.05	33.79 ± 0.08	$0.484 \pm 0.031 \pm 0.003$
N2	16.01 ± 0.98	34.03 ± 0.07	$0.471 \pm 0.029 \pm 0.003$
N3	14.43 ± 0.84	33.92 ± 0.06	$0.426 \pm 0.025 \pm 0.003$
N4	16.63 ± 0.96	34.07 ± 0.07	$0.488 \pm 0.028 \pm 0.003$
N5	16.07 ± 1.03	33.48 ± 0.08	$0.480 \pm 0.031 \pm 0.003$

$$\begin{aligned} \frac{Data^{Day}}{SSM_{BP98}^{Day}} &= 0.448 \pm 0.013(stat.) \pm 0.003(sys.) \\ \Phi_{Day} &= 2.31 \pm 0.07(stat.) \pm 0.02(sys.) \times 10^6/cm^2/sec \end{aligned}$$

For the all night subset of data, the measured flux is:

$$\begin{aligned} \frac{Data^{Night}}{SSM_{BP98}^{Night}} &= 0.467 \pm 0.013(stat.) \pm 0.003(sys.) \\ \Phi_{Night} &= 2.41 \pm 0.07(stat.) \pm 0.02(sys.) \times 10^6/cm^2/sec \end{aligned}$$

The resulting day/night asymmetry parameter is:

$$\frac{D - N}{0.5(D + N)} = -0.041 \pm 0.039(stat.) \pm 0.007(sys.)$$

In order to search for an enhancement in flux for the N5 subset, the N5 excess parameter is also calculated:

$$\frac{N5}{\langle D1, \dots, D5 \rangle} - 1.0 = 0.041 \pm 0.070(stat.) \pm 0.007(sys.)$$

where $\langle D1, \dots, D5 \rangle$ is the average of all 5 day subsets. No enhancement in the N5, or in the all night measurement, is observed relative to the day measurements.

8.1.4 Seasonal Flux Measurement

The seasonal flux is also compared to the expectations from the MC sample by correcting each subset by the livetime and calculating the rate of events. The livetimes for the seasonal subsets are summarized in Table 7.3. The resulting event rates for data and the BP98 MC are summarized, along with statistical errors, for all seasonal bins in Table 8.3. These results have been corrected for the eccentricity of the Earth's orbit, with all results calculated at 1 AU. The ratio of measured to expected event rates are shown in Figure 8.5.

A seasonal asymmetry parameter is calculated using the larger ES1 and ES2 bins and is found to be:

$$\frac{ES1 - ES2}{0.5(ES1 + ES2)} = -0.042 \pm 0.050(stat.) \pm 0.010(sys.)$$

No seasonal asymmetry is evident in this data sample.

8.2 Discussion

By finding a flux that is only 46% of the expected value, roughly 3.8σ lower than the flux predicted by the BP98 solar model, the Super-Kamiokande detector has confirmed the solar neutrino problem reported by the previous generation of experiments (see Section 1.2). Although the proposed changes to the solar models required to reduce the flux appear as unlikely solutions to

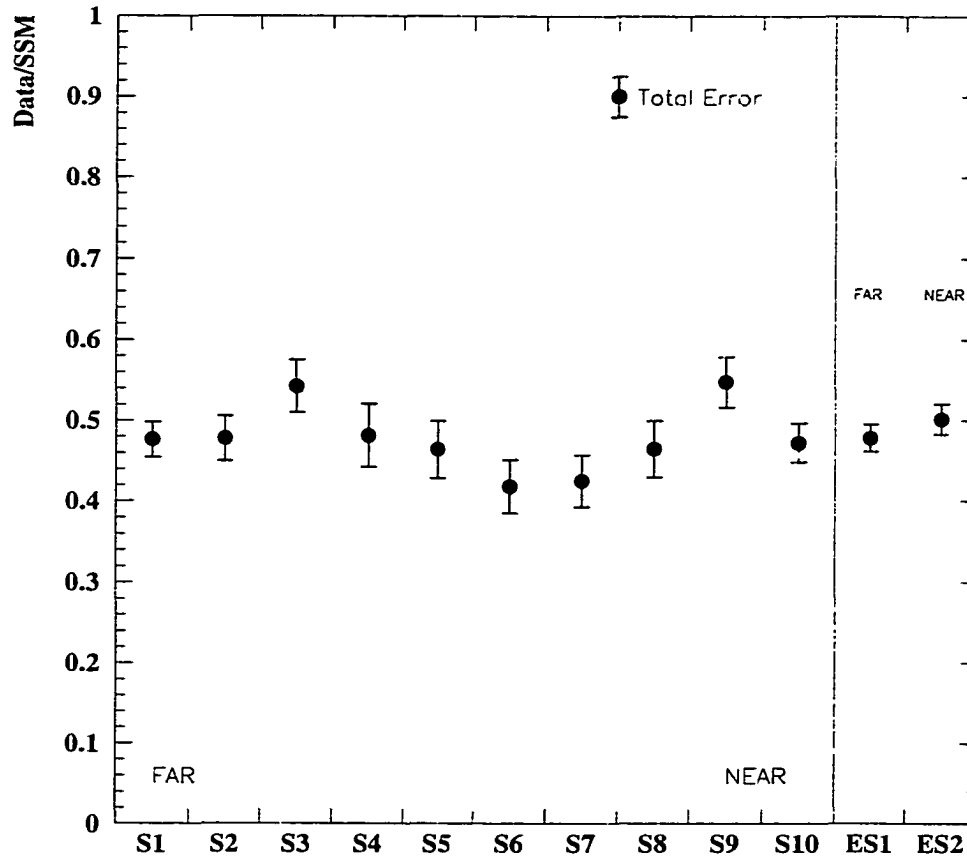


Figure 8.5: Ratio of measured to expected event rates for the seasonal flux subsets. Total errors presented are statistical and systematic errors added in quadrature. All results include a eccentricity correction to 1 AU.

Table 8.3: Seasonal subset measured fluxes in events/day for the data and the BP98 MC samples. Errors listed for measured rates are statistical only. Subsets are defined in Table 7.3. All results include a eccentricity correction to 1 AU.

Subset	Data Rate	BP98 MC Rate	$\frac{Data}{MC} \pm stat. \pm sys.$
S1	15.78 ± 0.70	33.11 ± 0.05	$0.477 \pm 0.021 \pm 0.004$
S2	15.85 ± 0.91	33.18 ± 0.07	$0.478 \pm 0.027 \pm 0.004$
S3	18.03 ± 1.07	33.24 ± 0.08	$0.542 \pm 0.032 \pm 0.005$
S4	16.24 ± 1.31	33.75 ± 0.09	$0.481 \pm 0.039 \pm 0.004$
S5	15.44 ± 1.17	33.28 ± 0.09	$0.464 \pm 0.035 \pm 0.004$
S6	13.95 ± 1.10	33.37 ± 0.09	$0.418 \pm 0.033 \pm 0.004$
S7	14.08 ± 1.06	33.14 ± 0.09	$0.425 \pm 0.032 \pm 0.004$
S8	14.71 ± 1.10	31.65 ± 0.08	$0.465 \pm 0.035 \pm 0.004$
S9	17.43 ± 0.98	31.85 ± 0.07	$0.547 \pm 0.031 \pm 0.005$
S10	15.01 ± 0.75	31.80 ± 0.06	$0.472 \pm 0.024 \pm 0.004$
ES1	15.84 ± 0.54	33.13 ± 0.04	$0.478 \pm 0.016 \pm 0.004$
ES2	15.96 ± 0.58	31.81 ± 0.04	$0.502 \pm 0.018 \pm 0.005$

this problem (see Section 1.3.1), the total flux of neutrinos from the SSM is ignored in the remaining analysis of these results. Therefore, any conclusions drawn from these results will not be strongly tied to the details of a given solar model.

The solar model independent quantities that SK was designed to look for, namely a distortion in the recoil electron spectrum, a day/night or seasonal flux variation, would be strong evidence for neutrino oscillations, if any were found. As an initial search for these effects, the measured results are compared to the simulation of the BP98 solar neutrino simulation, which does not include effects due to neutrino oscillations. This simulation reproduces the detector livetime, including the proper location of the Sun, water transparency and trigger threshold variations as a function of time. Any detector

related variation should be reflected in this simulated data. The relative fluxes measured in day and night, as well in different seasonal subsets of the data are compared to the results from the simulation as a search for flux variations in excess of what is expected from detector related effects. A comparison of the measured and simulation recoil electron spectral shapes is also used to look for any distortion in the measured spectrum. A χ^2 analysis is used to make these comparisons.

8.2.1 Day/Night Flux Variations

To search for evidence of day/night flux variations, the measured fluxes in the day and night subsets are compared to the results in the corresponding periods from the BP98 MC simulation. As no variation is expected during the day time period, the all day subset is taken to represent the day time period. The 5 night subsets are used to examine the night time flux, as some neutrino oscillation scenarios predict a zenith angle dependence to the flux variation. These fluxes are used to form a χ^2 :

$$\chi_{DN}^2 = \sum_{i=1}^6 \frac{(R_i^{Data} - \alpha \times R_i^{MC})^2}{\sigma_i^2 + \sigma_{sys,i}^2} \quad (8.1)$$

where:

R_i^{Data} = Event rates from Data for Day All, N1, N2, N3, N4, N5

R_i^{MC} = Event rates from MC for Day All, N1, N2, N3, N4, N5

α = Free parameter to allow scaling of the modeled flux

σ_i = Statistical error of R_i^{Data}

$\sigma_{sys,i}$ = Relative flux systematic error of each bin

The event rates and statistical errors used in this analysis are summarized in Table 8.2 and systematic errors for the relative day/night flux measurement

are summarized in Table 7.9. The value of α is allowed to vary between 0.0 and 1.0. The minimum χ^2 value is found:

$$\begin{aligned}\chi_{DN,min}^2 &= 4.83 \text{ for 5 degrees of freedom (dof)} \\ \alpha_{min} &= 0.457\end{aligned}$$

This χ^2 value corresponds to a confidence level of 43.7%. This result, combined with the lack of a statistically significant day/night asymmetry or N5 excess (as reported in Section 8.1.3) indicates that no significant day/night flux variation is found.

8.2.2 Seasonal Flux Variations

A search for a seasonal flux variation is performed in a similar manner to the day/night analysis. The measured seasonal flux results in 10 subsets (S1-S10) are compared to the corresponding subsets from the MC simulation. These relative flux measurements are used to form another χ^2 :

$$\chi_{Seas}^2 = \sum_{i=1}^{10} \frac{(R_i^{Data} - \alpha \times R_i^{MC})^2}{\sigma_i^2 + \sigma_{sys,i}^2} \quad (8.2)$$

where:

$$\begin{aligned}R_i^{Data} &= \text{Event rates from Data for the 10 seasonal subsets} \\ R_i^{MC} &= \text{Event rates from MC for the 10 seasonal subsets} \\ \alpha &= \text{Free parameter to allow scaling of the modeled flux} \\ \sigma_i &= \text{Statistical error of } R_i^{Data} \\ \sigma_{sys,i} &= \text{Relative flux systematic error of each bin}\end{aligned}$$

The event rates and statistical errors used in this analysis are summarized in Table 8.3 and systematic errors for the relative seasonal flux measurement

are summarized in Table 7.10. The value of α is allowed to vary between 0.0 and 1.0. The minimum χ^2 value is found:

$$\begin{aligned}\chi_{Seas,min}^2 &= 15.31 \text{ for 9 dof} \\ \alpha_{min} &= 0.478\end{aligned}$$

This χ^2 value corresponds to a confidence level of 8.3%. The disagreement between data and MC, while evident, is not strong enough to provide strong evidence of a seasonal flux variation. The seasonal flux asymmetry parameter (reported in Section 8.1.4) also shows no indication of a seasonal flux asymmetry.

8.2.3 Recoil Energy Spectrum Distortions

A search for distortions in the measured recoil electron spectrum is performed by comparing the measured spectrum to the MC simulation. The event rate in each of the 18 spectrum bins for data and MC are used to form a χ^2 :

$$\chi_{Spec}^2 = \sum_{i=1}^{18} \frac{(R_i^{Data}[1 + (\gamma_i)_{ang}] - \alpha \times R_i^{MC}[1 + (\gamma_i)_{scale} + (\gamma_i)_{shape}])^2}{\sigma_i^2 + \sigma_{sys,i}^2} + \epsilon^2 + \xi^2 + \eta^2 \quad (8.3)$$

where:

- R_i^{Data} = Event rates from Data for the 18 spectrum bins
- R_i^{MC} = Event rates from MC ($^8\text{B} + \text{hep}$) for the 18 spectrum bins
- α = Free parameter to allow scaling of the modeled flux
- σ_i = Statistical error of R_i^{Data}
- $\sigma_{sys,i}$ = Non-energy dependent systematic errors of each bin

$$\begin{aligned}
(\gamma_i)_{ang} &= \epsilon \cdot \Delta_i^{ang} \\
\Delta_i^{ang} &= \text{Energy dependent systematic error from the angular cut} \\
(\gamma_i)_{scale} &= \xi \cdot \Delta_i^{scale} \\
\Delta_i^{scale} &= \text{Energy dependent systematic error from the} \\
&\quad \text{absolute energy scale} \\
(\gamma_i)_{shape} &= \eta \cdot \Delta_i^{shape} \\
\Delta_i^{shape} &= \text{Energy dependent systematic error from the } ^8\text{B spectral shape} \\
\epsilon, \xi, \eta &= \text{Free parameters allowing effects of the energy dependent} \\
&\quad \text{systematic errors to change}
\end{aligned}$$

The event rates and statistical errors used in this analysis are summarized in Table 8.1 and systematic errors for the relative seasonal flux measurement are summarized in Table 7.7 and Table 7.6. The value of α is allowed to vary between 0.0 and 1.0. The values of ϵ, ξ, η are allowed to vary between +3.0 and -3.0. The minimum χ^2 value is found:

$$\begin{aligned}
\chi_{Spec,min}^2 &= 13.27 \text{ for 17 dof} \\
\alpha_{min} &= 0.450 \\
\epsilon_{min} &= 0.00, \xi_{min} = 0.50, \eta_{min} = 0.75
\end{aligned}$$

This χ^2 value corresponds to a confidence level of 71.8%. If ϵ, ξ , and η are required to be 0.0, the χ^2 value is 14.46 (17 dof), with a 63.4% confidence level.

Since the hep neutrino flux has such large uncertainties (as discussed in Section 1.1), the hep contribution to the recoil electron spectrum should

be treated as an independent free parameter. This is done by making the following substitution to Eqn. 8.3:

$$\alpha \times R_i^{MC} \rightarrow \alpha \times R_i^{^8B} + \beta \times R_i^{HEP} \quad (8.4)$$

where:

$R_i^{^8B}$ = Event rates from 8B -only MC for the 18 spectrum bins

R_i^{HEP} = Event rates from hep-only MC for the 18 spectrum bins

α = Free parameter to allow scaling of the modeled 8B flux

β = Free parameter to allow scaling of the modeled hep flux

Both $R_i^{^8B}$ and R_i^{HEP} are listed in Table 8.1. The value of α is varied between 0.0 and 1.0, while β is varied between 0.0 and 25.0. The minimum χ^2 value is found:

$$\chi_{Spec,min}^2 = 11.22 \text{ for 16 dof}$$

$$\alpha_{min} = 0.450$$

$$\beta_{min} = 9.125$$

$$\epsilon_{min} = 0.05, \xi_{min} = 0.15, \eta_{min} = 0.05$$

This corresponds to a confidence level of 79.6%. This results indicates good agreement between the measured recoil electron spectrum and the BP98 MC simulation spectrum. The spectral shape predicted by these minimum values values of $\alpha, \beta, \epsilon, \xi$, and η is shown in Figure 8.6 and is compared to the measured spectral shape of Figure 8.2. The slight increase in the high energy bins is well fit by a hep neutrino flux that is roughly 9 times the SSM

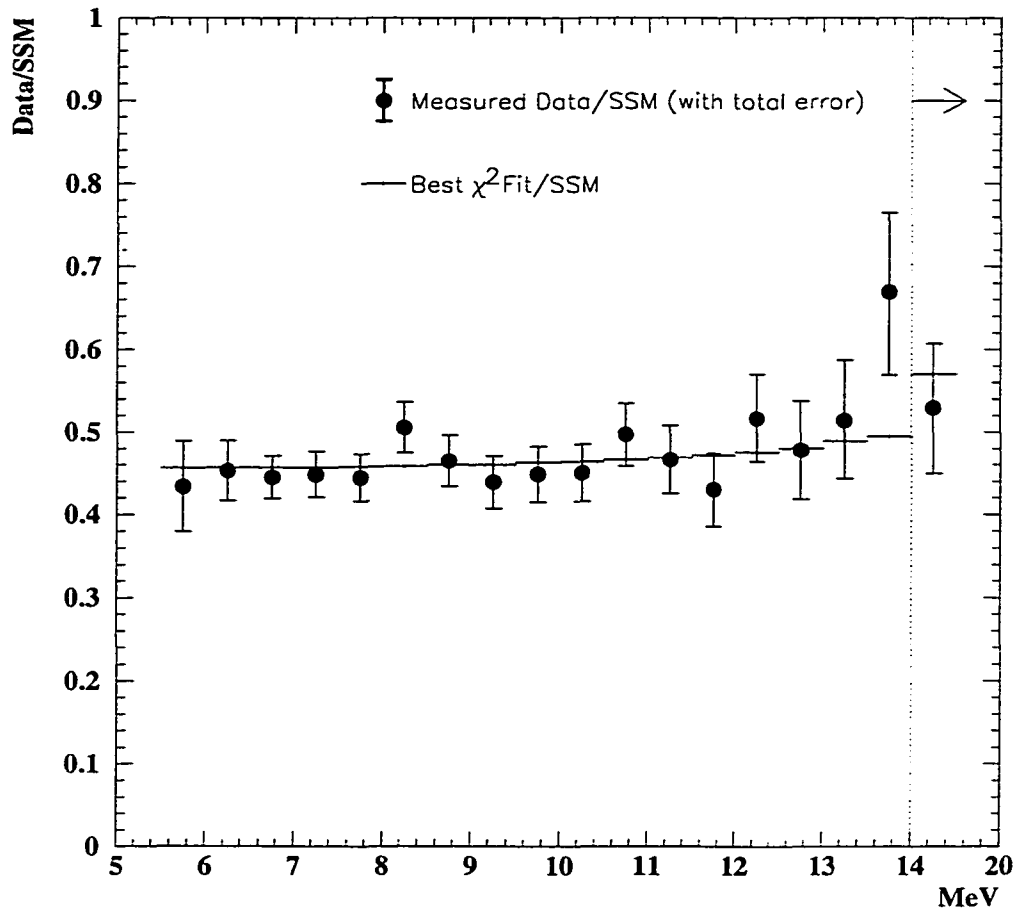


Figure 8.6: The ratio of measured spectral shape for data (Data/SSM) and the spectral shape resulting from the best fit χ^2 .

value and no strong indication of a distortion in the solar neutrino spectrum resulting from neutrino oscillations is seen.

8.3 Neutrino Oscillation Analysis

As the recoil electron spectrum, day/night flux variation, and seasonal flux variation all appear to agree with the results from the simulation of an unoscillated neutrino flux, these measured results can be used to exclude portions of the neutrino oscillation parameter space that predict variations in

these measured quantities beyond what is observed. To perform this analysis, a calculation of the neutrino flux arriving at the SK detector is performed assuming a neutrino oscillation scenario that includes MSW matter effects. This incident neutrino flux is converted to a flux and spectrum of scattered electrons using a special MC simulation. A χ^2 analysis is then used to rule out portions of the parameter space that do not agree with the observed day/night recoil electron spectra.

8.3.1 Neutrino Flux Calculation

In order to study neutrino oscillations, the effects of oscillations on the neutrino flux incident on the SK detector must be evaluated. This incident flux can include electron type neutrinos, as well as non-electron type neutrinos (muon or tau type). These non-electron neutrinos (called muon neutrinos here) need to be included in the analysis, as they can interact in the SK detector by the neutral current interaction (see Section 5.1.1), and would be an additional source of scattered electrons. Sterile neutrinos are not considered here.

The incident neutrino fluxes are calculated in two regions of the parameter space of Δm^2 and $\sin^2 2\theta$. The first region considered is the MSW region, where MSW matter oscillations are expected to play an important role. In the MSW region, the Δm^2 parameter is considered in the range of values:

$$\log(\Delta m^2) = -3.0 \text{ to } -8.0 \text{ (in 51 logarithmic bins)}$$

The $\sin^2 2\theta$ parameter is divided into 40 bins, depending on the value considered:

$$\sin^2 2\theta = 1.0 \text{ to } 0.1 \text{ (in 10 linear bins)}$$

$$\log(\sin^2 2\theta) = -1.1 \text{ to } -4.0 \text{ (in 30 logarithmic bins)}$$

The linear division of bins is chosen to provide more even coverage of the parameter space in the region near maximal mixing.

The second region, known as the just-so region, covers the region where the Earth-Sun separation and the neutrino oscillation lengths are nearly equal. In this region, the range of Δm^2 parameters considered includes:

$$\log(\Delta m^2) = -9.0 \text{ to } -11.0 \text{ (in 21 logarithmic bins)}$$

and as vacuum oscillations are only important near maximal mixing, the $\sin^2 2\theta$ parameter region considered is:

$$\sin^2 2\theta = 1.0 \text{ to } 0.1 \text{ (in 10 linear bins)}$$

The values of Δm^2 and $\sin^2 2\theta$ at the center of each bin are used in the calculation of the incident neutrino fluxes.

The incident neutrino fluxes are evaluated using the BP98 solar model (as described in Section 1.1) as the solar neutrino production model. This model assumes a spherically symmetric Sun, and provides the radial electron density distribution of the Sun, as shown in Figure 1.3, that are needed for the evaluation of MSW matter oscillations. The solar model also provides the radial distributions of neutrino production points for each type of neutrino. These are used as the source locations in this calculation and are shown in Figure 1.4.

In order to evaluate the neutrino fluxes reaching the SK detector, the Sun is divided into small zones based on the radius (dR) and zenith angle ($d\theta$) of each zone. Each zone is treated as a point source of neutrinos, where the flux of neutrinos in a zone is based on the type of neutrinos produced at that energy and the radial distributions of neutrino production points. This calculation

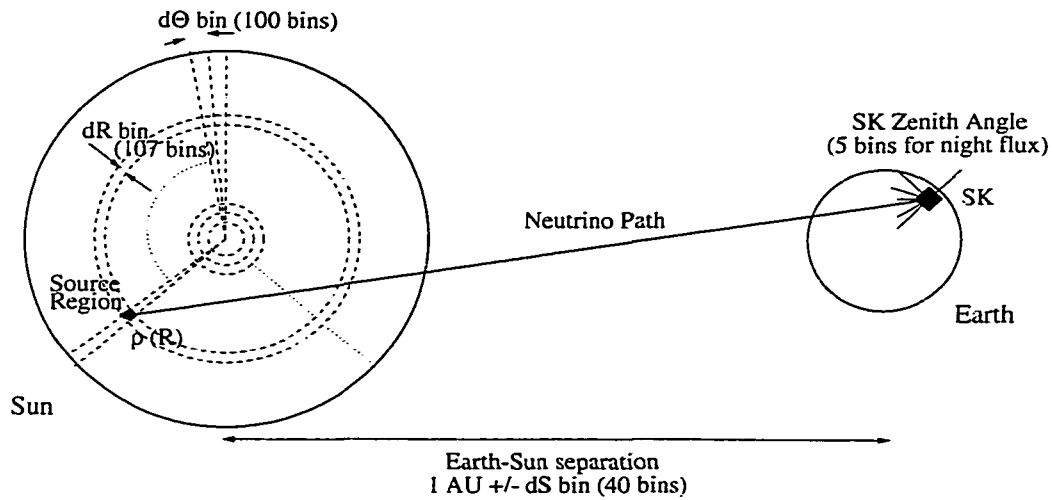


Figure 8.7: An overview of the neutrino oscillation simulation. The Sun is divided into small zones in radius (dR) and zenith angle ($d\theta$). Each zone is treated as a point source of electron neutrinos, and the path to the SK detector is simulated through the Sun, and, if necessary, through the Earth. In this way, the fluxes of electron and muon neutrinos are evaluated at the SK detector.

considers all neutrinos with energies between 3.0 and 20.0 MeV (including ^8B and hep neutrinos) in 0.1 MeV energy bins. The flux of neutrinos from each zone in the Sun and in each energy bin is then propagated along the path connecting the zone and the SK detector, as illustrated in Figure 8.7. Each energy bin is treated independently, as the effects of neutrino oscillation depend on the neutrino energy. All neutrinos produced in the Sun and input into the oscillation calculation begin as electron type neutrinos. The fluxes of neutrinos from all zones in the Sun are added together once they reach the SK detector.

The path from each small source bin in the Sun to the Earth is evaluated, taking note of the density regions traversed while exiting the Sun.

The propagation of the neutrino wavefunction is done by numerically solving Eqn. 1.17 in a stepwise manner. The size of each step is varied, depending on the local density, and the value of the resonant density ($N_{e,res}$, see Eqn. 1.21). When the local density is far from a resonance, the steps taken are large ($\sim 5\%$ of a solar radius). As the location in the Sun begins to approach a resonance, the step sizes are reduced to just a small fraction of the oscillation length (L_m , see Eqn. 1.23). Once through the resonance, the step size is again increased until the surface of the Sun is reached. Neutrinos created on the far side of the Sun could traverse two resonance regions on the path to Sun's surface.

Once the neutrinos have reached the Sun's surface, the wavefunctions are then propagated through vacuum to the location of the Earth. As the position of the Earth changes depending on the time of year, the full range of the Earth-Sun separation is divided into 40 bins and the neutrino flux is calculated in each bin. This treatment ensures that any seasonal variation in the oscillated neutrino flux is preserved. In a similar manner, the zenith angle at which the solar neutrinos arrive at SK is also divided into 20 bins to preserve any day/night flux differences present in the oscillated flux. For those SK zenith angle bins that have neutrino trajectories passing through the Earth (in the night flux bins), the wavefunction is propagated through the Earth in a similar manner as the Sun, properly treating any resonant density regions encountered. The electron density of the Earth is obtained from Reference [46]. A single calculation of the trajectory through the Sun in each energy bin is used to fill all Earth-Sun separation and SK zenith angle

bins. Once at the SK detector, the flux of electron and muon neutrinos are evaluated from the wavefunction amplitudes. In this manner, a “map” of electron and muon neutrino fluxes is generated covering each possible value of the Earth-Sun separation and SK zenith angle. This flux map is generated for every set of Δm^2 and $\sin^2 2\theta$ considered.

The livetime exposure of each bin in the Earth-Sun separation and SK zenith angle map is determined from the known run conditions present in the final sample of solar neutrino candidates. This ensures that the oscillated neutrino and real data samples share the same livetime exposures. This livetime map is used with the neutrino flux map to weight the incident fluxes in each bin and obtain the total number of each type of neutrino per cm^2 incident on the SK detector during the livetime period. These fluxes are next evaluated by MC simulation to obtain the flux and spectrum of recoil electrons.

8.3.2 Simulated Detector Response

The oscillated neutrino fluxes must be converted into rates and spectra of scattered electrons in order to be compared with the data measured in the SK detector. Ideally this would be done by performing individual MC detector simulations for each point in the neutrino oscillation parameter space considered, but this would be too computationally difficult. Instead, this calculation is split into two parts, treating the generation and detector simulation of scattered electrons separately.

First, the oscillated flux and spectrum of each type of neutrino is used to generate a sample of scattered electrons, following the procedure described

in Section 5.1. Electron type neutrinos interact by the neutral and charge current interaction cross sections, while muon type neutrinos are limited to the neutral current only cross sections. The total flux and spectrum of scattered electrons to be input into the detector simulation is obtained by summing these two pieces.

Second, the MC detector simulation of these scattered electrons is treated using a “fast” electron simulation instead of a full MC detector simulation. The “fast” simulation is prepared by generating ~ 4 million electrons covering the energy range of 3-20 MeV and performing a full MC detector simulation for each one. These electrons are given a random input energy in the selected range, and a random position in the SK detector. This sample is reconstructed in the same manner as the full simulation of the BP98 flux described in Section 5.2. The events of this sample are divided into 170 bins of 0.1 MeV width based on the input electron energy. For each input energy bin, the fraction of events that are successfully reconstructed inside the fiducial volume is determined, as well as the resulting reconstructed electron spectrum. In this manner, a conversion map from input electron energy to reconstructed energy is obtained. This “fast” simulation is then used to generate the reconstructed flux and spectrum of recoil electrons by weighting these results based on the spectrum of the oscillated input scattered electrons. In essence, this “fast” simulation uses a single set of MC simulation data to simulate the flux and spectrum of scattered electrons at each set of oscillation parameters.

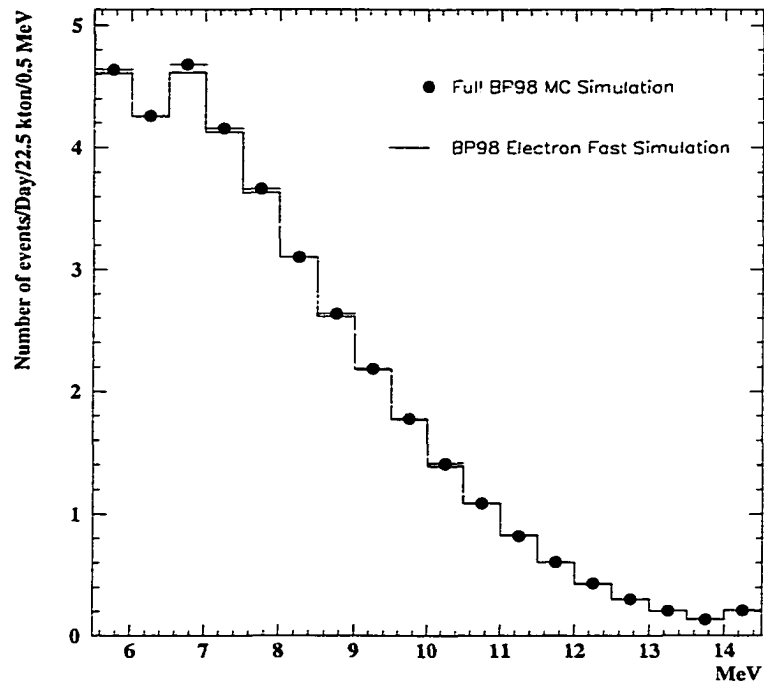


Figure 8.8: Comparison of the recoil electron spectrum from the full simulation of the BP98 flux and the fast electron simulation of the BP98 flux with no oscillations. The fast electron simulation is used to evaluate the flux and spectrum of recoil electrons for the oscillation analysis.

A check of the results from this “fast” electron simulation is performed by inputting the unoscillated BP98 flux and spectrum of neutrinos and comparing the results to the full MC detector simulation described in Chapter 5. The agreement between the reconstructed recoil electron spectra shown in Figure 8.8 is quite good. The total measured flux obtained in both simulations differ by less than 1%. Using this simulation technique, all oscillated neutrino fluxes are converted to reconstructed fluxes and spectra of recoil electrons. The flux variation between different SK zenith angle and seasonal subsets is also calculated.

8.3.3 Excluded Regions

To test neutrino oscillation hypotheses, the predicted flux variations and spectral shape at each set of neutrino oscillation parameters is compared to the measured value using a χ^2 analysis. This χ^2 analysis compares the day and night oscillated recoil electron spectra to the measured results from real data (shown in Figure 8.3) to rule out portions of the neutrino oscillation parameter space that are inconsistent with measured data. Seasonal variations are not included in this analysis as the current SK data sample lacks the statistical power needed for clear observations of predicted effects.

The χ^2 used has 34 dof and is defined by:

$$\chi^2 = \sum_{\text{Day.Night}} \sum_{i=1}^{18} \frac{(R_i^{\text{Data}} - \alpha \times R_i^{\text{MC}} [1 + (\gamma_i)_{\text{scale}} + (\gamma_i)_{\text{shape}} + \beta \kappa(i)])^2}{\sigma_i^2 + \sigma_{\text{sys},i}^2} + \xi^2 + \eta^2 \quad (8.5)$$

where:

R_i^{Data} = Event rates from data for the day and night spectrum bins

R_i^{MC} = Event rates from oscillated MC for the day
and night spectrum bins

α = Free parameter to allow scaling of the modeled flux

σ_i = Statistical error of R_i^{Data}

$\sigma_{\text{sys},i}$ = Non-energy dependent systematic errors of each bin

$(\gamma_i)_{\text{scale}}$ = $\xi \cdot \Delta_i^{\text{scale}}$

Δ_i^{scale} = Energy dependent systematic error from the
absolute energy scale

$(\gamma_i)_{\text{shape}}$ = $\eta \cdot \Delta_i^{\text{shape}}$

Δ_i^{shape} = Energy dependent systematic error from the ^8B spectral shape

ξ, η = Free parameters allowing effects of the energy dependent systematic errors to change

$\kappa(i)$ = Fraction of events in each energy bin from hep neutrinos

β = Free parameter to allow scaling of hep flux relative to ^8B

The minimum χ^2 value at each set of oscillation parameters is obtained by allowing the values of α, β, ξ , and η to vary over the following ranges:

$$\alpha : 0.0 - 3.0$$

$$\beta : 0.0 - 60.0$$

$$\xi : -3.0 - +3.0$$

$$\eta : -3.0 - +3.0$$

and taking the minimum χ^2 value found to represent that point. No variation of the ϵ parameter (from the angular cut systematic error) is performed here as was done in Section 8.2.3. This is done to increase computational speed, but as these errors show little energy dependence (see Table 7.7), the difference is small. Instead, this error is added to the non-energy dependent portion of the systematic error.

The χ^2 values obtained are first used to perform a hypothesis test to exclude portions of the Δm^2 and $\sin^2 2\theta$ parameter space. Points with $\chi^2 > 56.06/34$ dof are excluded at the 99% confidence level. Similarly, a $\chi^2 > 48.60/34$ dof results in a 95% exclusion and a $\chi^2 > 44.90/34$ dof results in a 90% exclusion. The resulting 99%, 95% and 90% exclusion regions from this

hypothesis test are shown in Figures 8.9 and 8.10 for the MSW region and the just-so region, respectively.

A second look at exclusion regions is made by considering the distance from the χ^2 minimum. In this analysis, the global χ^2 minimum has a value of 39.41/34 dof, at a 24.1% confidence level. This minimum is located at a $(\Delta m^2, \sin^2 2\theta)$ of $(3.16 \times 10^{-7}, 0.30)$. Exclusion regions are made based on the value of $\Delta\chi^2 = \chi^2 - \chi_{\min}^2$ [2]. Any point with $\Delta\chi^2 > 9.21$ is excluded at the 99% level. Similarly, a $\Delta\chi^2 > 6.18$ results in 95% exclusion. The resulting 99% and 95% exclusion regions based on the distance from the χ^2 minimum are shown in Figures 8.11 and 8.12 for the MSW and just-so regions, respectively. Both methods generate similar exclusion regions, with the distance from the minimum method providing slightly more exclusion.

There are two areas in the MSW region that are strongly excluded. The recoil electron spectra predicted for these regions show strong effects resulting from neutrino oscillations that are not seen in the measured data. The long, horizontal region near a Δm^2 of 10^{-4} is strongly excluded as the oscillation parameters in this region predict large suppression of higher energy neutrinos. This results in a more steeply falling recoil electron spectrum than is predicted in absence of oscillations. Points in the large oval-shaped excluded region centered near a Δm^2 of 10^{-6} and near maximal mixing are strongly excluded due to a lack of an observed day/night flux difference. Points in this region predict large amount of electron neutrino flux regeneration in the Earth, and consequently a distinct night-time recoil electron flux excess. The diagonal exclusion region connecting these two regions does show some

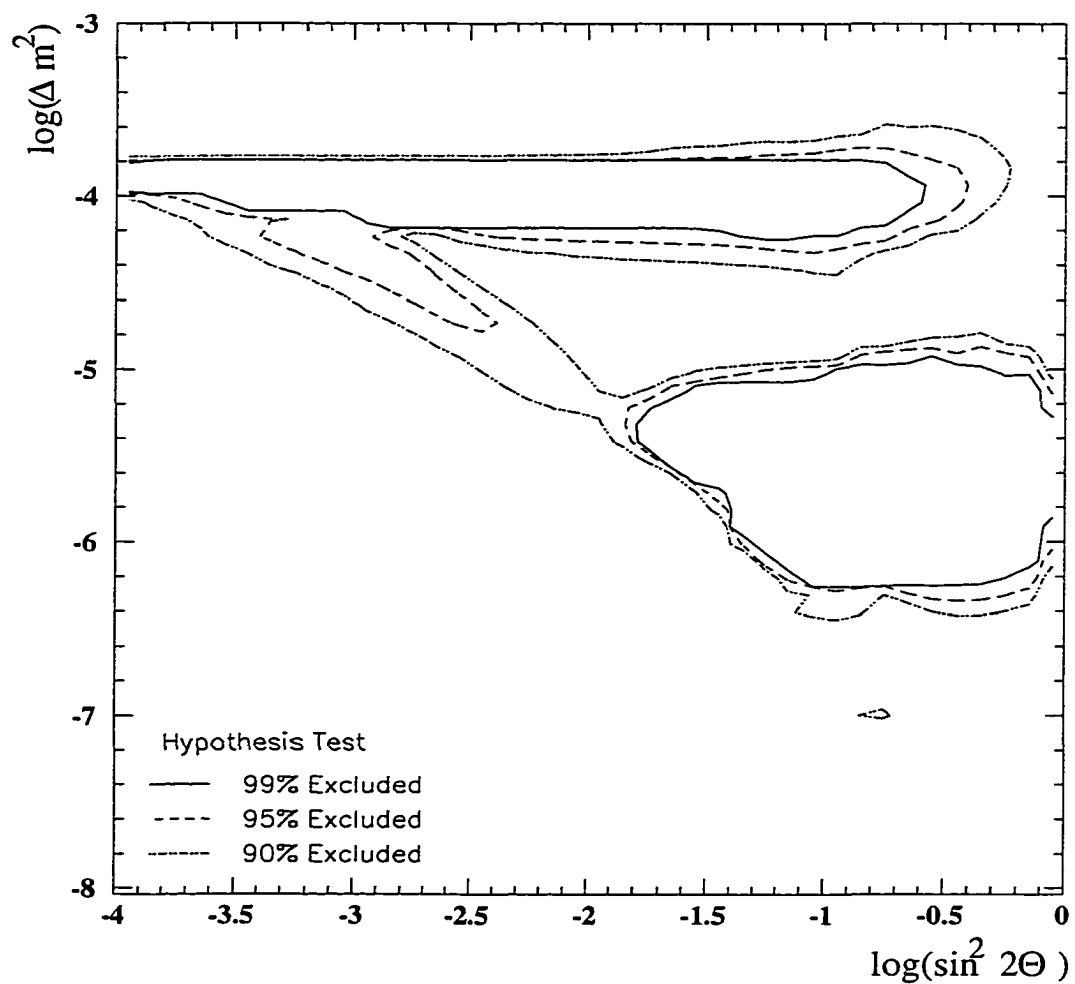


Figure 8.9: 99%, 95%, and 90% excluded regions from a hypothesis test performed on a χ^2 analysis of the measured day and night spectra in the MSW region.

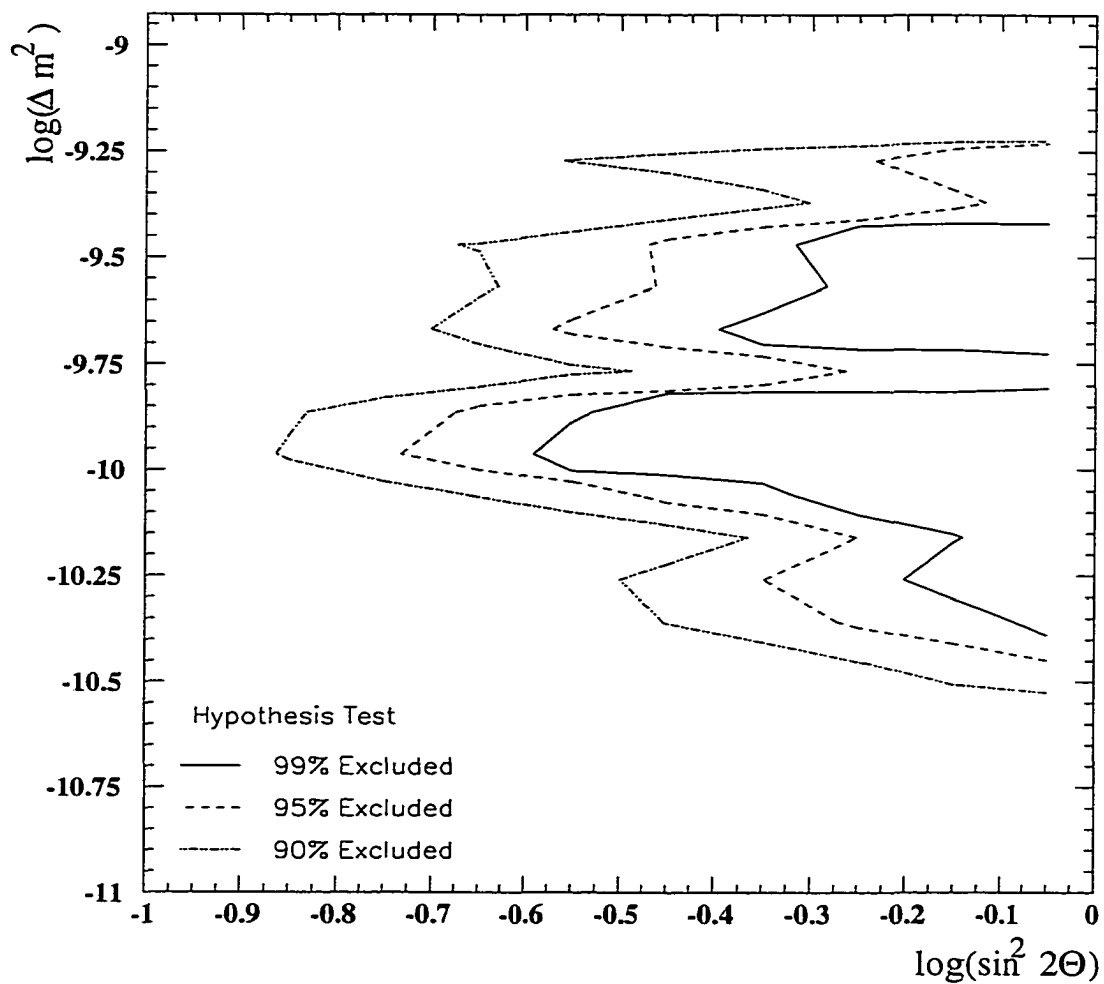


Figure 8.10: 99%, 95%, and 90% excluded regions from a hypothesis test performed on a χ^2 analysis of the measured day and night spectra in the just-so region.

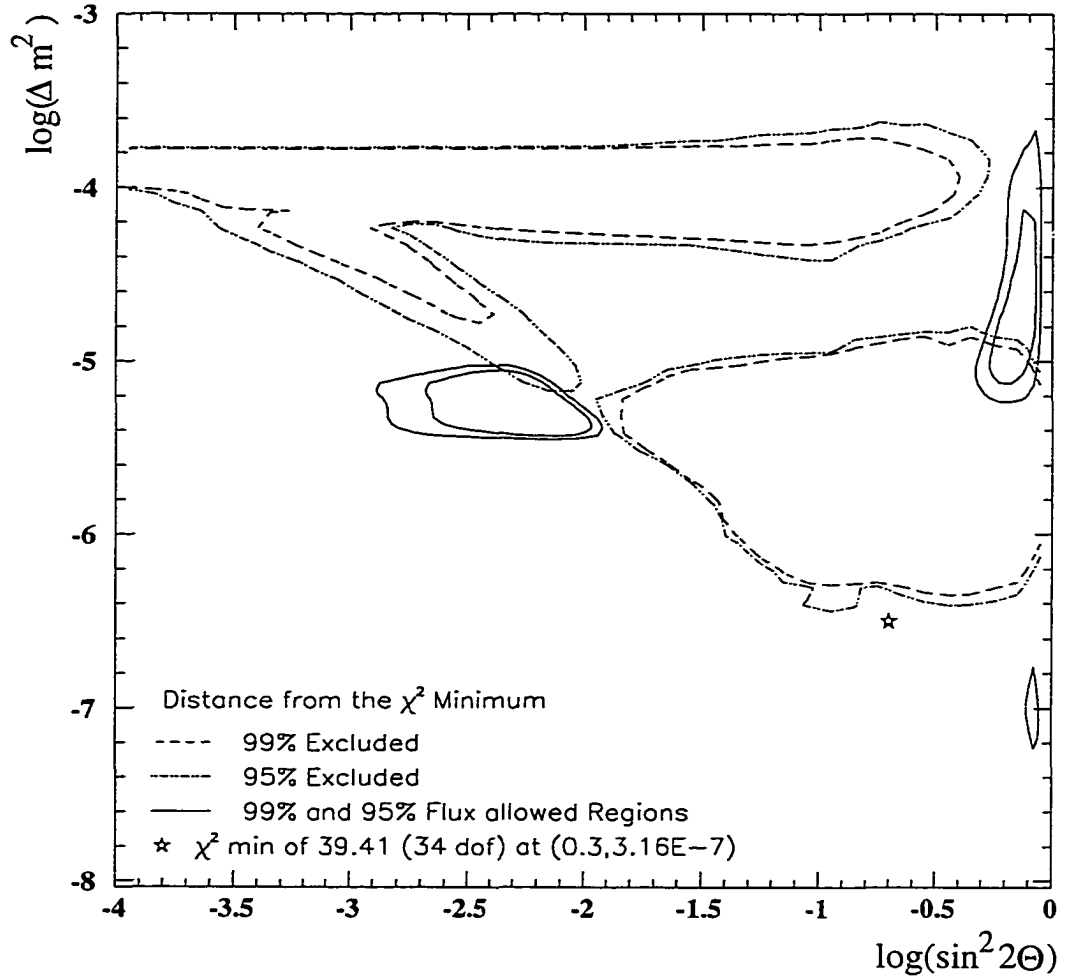


Figure 8.11: MSW 99% and 95% excluded regions based on the distance from the χ^2 minimum. The χ^2 minimum is shown in the figure. Also shown are the 99% and 95% allowed regions from an analysis of the measured fluxes in all experiments, as discussed in Section 1.3.2.3.

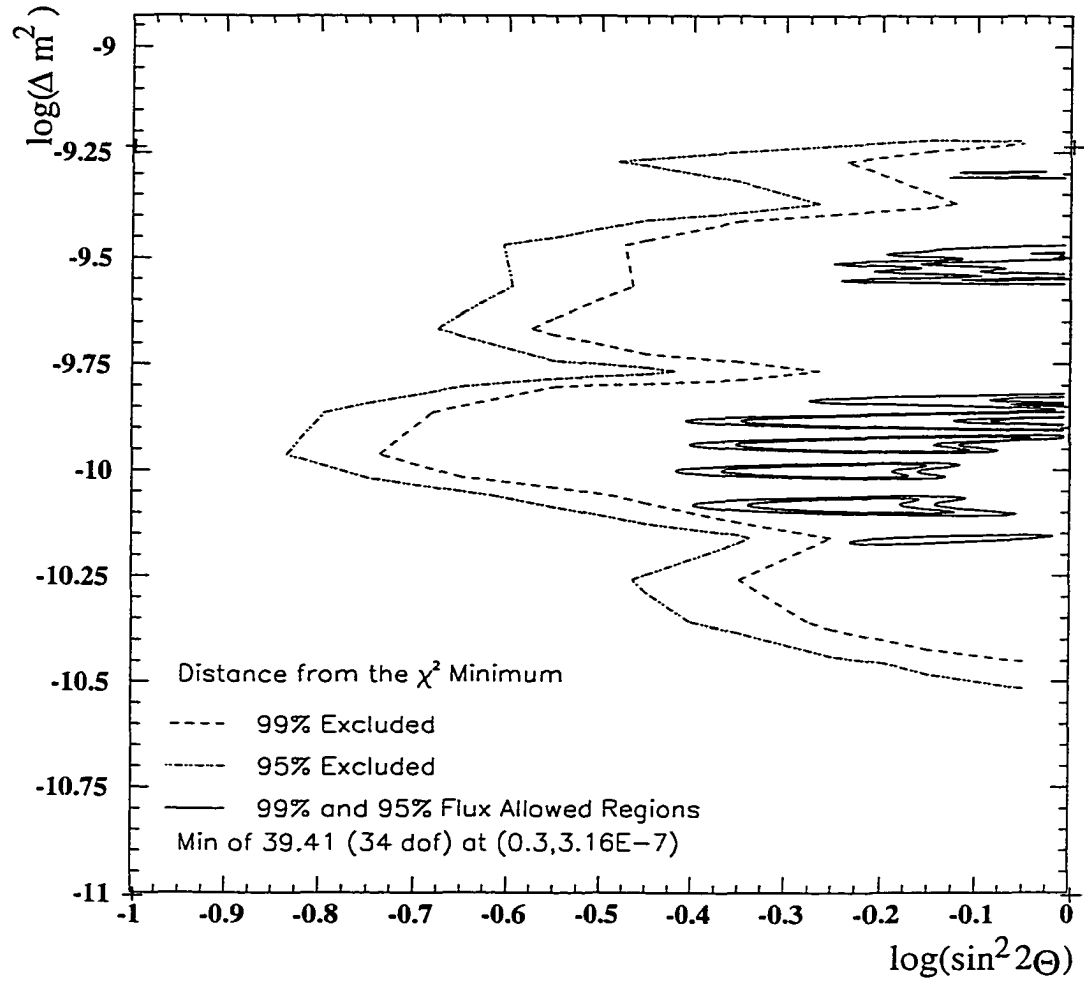


Figure 8.12: Just-So 99% and 95% excluded regions based on the distance from the χ^2 minimum. The χ^2 minimum is shown in Figure 8.11. Also shown are the 99% and 95% allowed regions from an analysis of the measured fluxes in all experiments, as discussed in Section 1.3.2.3.

exclusion, but is more difficult to fully exclude. Points in this region predict a preferential suppression of low energy neutrinos, resulting in a recoil electron spectrum that is less steeply falling than expected. The exclusion is less pronounced in this region given the slight upward slope of the measured spectra (as seen in Figure 8.3), and the physics of recoil electron production. Higher energy neutrinos have a larger interaction cross section (as shown in Figure 5.1), and can produce low energy scattered electrons (see Figure 5.4), increasing the difficulty of observing a deficit of low energy neutrinos. On the other hand, when the high energy neutrinos are missing, a strong effect is seen in the recoil electron spectrum. If the measured spectral shape remains unchanged with additional data, the smaller statistical errors of future measurements will be able to rule out this diagonal strip.

The exclusion regions found in the just-so region are generated by spectral distortions arising from the energy dependence of the oscillation length (L_{osc} , see Eqn 1.15). The rough appearance of these regions arises from this dependence, as a small change in the modeled Δm^2 value will result in different energy dependence for the incident neutrino flux. These excluded regions are also restricted to areas of maximal mixing in $\sin^2 2\theta$.

Figures 8.11 and 8.12 also contain the 99% and 95% allowed regions based on the analysis of the measured flux from the Cl, Ga and water experiments, as presented in Section 1.3.2.3. In the MSW region, the excluded regions have reduced the size of the Large Mixing Angle (LMA) solution. A small amount of reduction is also seen at the edge of the Small Mixing Angle (SMA) solution, but both the LMA and SMA still contain regions that are

not excluded by this measurement. In the Just-So region, the allowed regions from the measured fluxes are completely excluded by this analysis.

8.4 Summary

The rate and spectrum of recoil electrons resulting from neutrino-electron elastic scattering has been used to study the neutrinos produced in the nuclear fusion reactions that power the Sun. In the first 980.4 days of operation, the Super-Kamiokande detector has observed an electron scattering rate above 5.5 MeV in electron energy of

$$15.56 \pm 0.31(stat.) \text{ events/day/22.5 kton.}$$

This represents a factor of $0.458 \pm 0.009(stat.)^{+0.011}_{-0.007}(sys.)$ of the rate expected from the BP98 solar model. The spectrum of these recoil electron events has also been measured and is presented as the ratio of the measured to the expected spectra in Figure 8.2. A χ^2 analysis of this measured spectrum does not show any indication of a distortion in shape arising from the effects of neutrino oscillations. Additionally, the measured scattering rate does not show any indication of day/night or seasonal variations, which, if found, would have been strong indications of neutrino oscillations. The recoil electron spectra measured during the day and night time periods are compared using a χ^2 analysis to the spectra predicted by neutrino oscillations to exclude portions of the neutrino oscillation parameter space that are inconsistent with these measured results, as shown in Figures 8.9 and 8.10.

REFERENCES

- [1] Y. Fukuda, et al., *Phys. Rev. Lett* **81** (1998) 1562.
- [2] C. Caso et al., *The European Physical Journal C* **3** (1998) 1.
- [3] J.N. Bahcall, M.H. Pinsonneault, *Reviews of Modern Physics* **67** (1995) 781.
- [4] J.N. Bahcall, *Neutrino Astrophysics*. Cambridge University Press, 1989.
- [5] J.N. Bahcall, *Astrophysics Journal* **467** (1996) 475.
- [6] G.G. Raffelt, *Stars as Laboratories for Fundamental Physics* University of Chicago Press, 1996.
- [7] E.G. Adelberger, et al., *Reviews of Modern Physics* **70** (1998) 1265.
- [8] J.N. Bahcall, P.I. Krastev, *Phys. Lett.* **436** (1998) 243.
- [9] R. Davis, D.S. Harmer, K.C. Hoffman, *Phys. Rev. Lett* **20** (1968) 1205.
- [10] B.T. Cleveland *Ap. J* **496** (1998) 505.
- [11] J.N. Bahcall, S. Basu, M.H. Pinsonneault, *Phys. Lett. B* **433** (1998) 1.
- [12] K.S. Hirata et al., *Phys. Rev. D* **44** (1991) 2241.
- [13] Y. Fukuda et al., *Phys. Rev. Lett.* **77** (1996) 1683.
- [14] J.N. Abdurashitov et al., *Phys. Rev. C* **60** (1999) 055801.
- [15] J.N. Abdurashitov et al., *Phys. Rev. Lett.* **77** (1996) 4708.
- [16] P. Anselmann et al., *Phys. Lett. B* **285** (1992) 376.
- [17] P. Anselmann et al., *Phys. Lett. B* **447** (1999) 127.
- [18] P. Anselmann et al., *Phys. Lett. B* **342** (1995) 440.
- [19] N. Hata and P. Langacker, *Phys. Rev. D* **50** (1994) 632.
- [20] N. Hata and P. Langacker, *Phys. Rev. D* **56** (1997) 6107.
- [21] L. Wolfenstein, *Phys. Rev. D* **17** (1978) 2369.
- [22] S. P. Mikheyev, A. S. Smirnov, *Sov. J. Nucl. Phys.* **42** (1985) 913.

- [23] A. Suzuki, M. Mori , et al., *Nucl. Inst. Meth. A* **329** (1993) 299.
- [24] R. Claus, et al., *Nucl. Inst. Meth. A* **261** (1987) 540.
- [25] Jeffery S. George, *Experimental Study of the Atmospheric ν_μ/ν_e Ratio in the Multi-GeV Energy Range*. PhD Thesis, University of Washington, 1998.
- [26] Mark. D. Messier, *Evidence for Neutrino Mass from Observations of Atmospheric Neutrinos at Super-Kamiokade*. PhD Thesis, Boston University, 1999.
- [27] Robert E. Sanford, *Spectrum of Solar Neutrinos above 6.5 MeV*. PhD Thesis, Louisiana State University, 1999.
- [28] Zoa Conner, *A Study of Solar Neutrinos Using the Super-Kamiokande Detector*. PhD Thesis, University of Maryland, 1997.
- [29] M. Nakahata et al., *Nuclear Instruments and Methods A* **421** (1999) 113.
- [30] J.A. De Juren, et al., *Phys. Rev.* **127** (1962) 1229.
- [31] Yusuke Koshio, *Study of Solar Neutrinos at Super-Kamiokande*. PhD Thesis, University of Tokyo, 1998.
- [32] GEANT Detector Description and Simulation Tool, *Cern Program Library W5013* (1994).
- [33] D.H. Wilkinson in *Nuclear Physics with heavy ions and mesons*, R. Balian et al., eds., (North Holland Publishing Co., 1978) 935.
- [34] M. Morita, *Beta Decay and Muon Capture* (W.A. Benjamin, Reading, MA, 1973) 32.
- [35] R. B. Firestone, *Table Of Isotopes, Vol. 1* (John Wiley and Sons, New York, 1996) 20.
- [36] Takayuki Yamaguchi, *Observation of 8B Solar Neutrinos from 300-Day Data at Super-Kamiokade*. PhD Thesis, University of Osaka, 1998.
- [37] J.N. Bahcall et al., *Phys. Rev. C* **54** (1996) 411.
- [38] J.N. Bahcall, M. Kamionkowski, A. Sirlin, *Phys. Rev. D* **51** (1995) 6146.
- [39] J.N. Bahcall, Private communication, 1998.
- [40] A. Suzuki, et al., *Nuclear Instruments and Methods A* **329** (1993) 299.

- [41] Hirokazu Ishino, *Measurement of the Solar Neutrino Spectrum at Super-Kamiokande*, PhD Thesis, University of Tokyo, 1999.
- [42] E. Blaufuss, et al., To be published in *Nuclear Instruments and Methods A*, hep-ex/0005014.
- [43] S. Matsuno et al., *Phys. Rev. D* **29** (1984) 1.
- [44] T. Suzuki, D.F. Measday, and J.P. Roalsvig, *Phys Rev. C* **35** (1987) 2212.
- [45] P. Guichon et al., *Phys Rev. C* **19** (1979) 987.
- [46] A.M. Dziewonski and D.L. Anderson, *Phys. Earth Planet. Inter.* **25** (1981) 297.

VITA

Erik Blaufuss was born in Harbor City, California, in 1971. He graduated from Esperanza High School in Anaheim, California, in 1989. He received his bachelor of science degree in physics from the University of California, Irvine, in 1995. He received the degree of Doctor of Philosophy in physics from Louisiana State University in December, 2000. After graduate school, he accepted a post-doctoral position at the University of Maryland, in College Park.

DOCTORAL EXAMINATION AND DISSERTATION REPORT

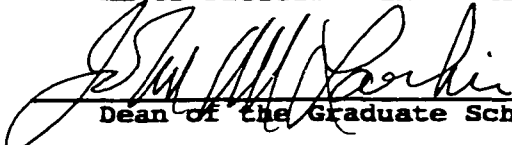
Candidate: Erik Blaufuss

Major Field: Physics

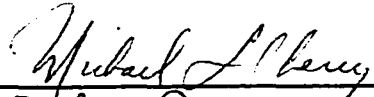

Title of Dissertation: Study of the Energy Spectrum of Solar Neutrinos Above 5.5 MeV

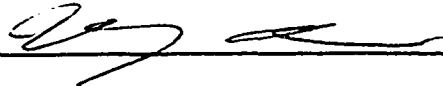
Approved:


Major Professor and Chairman


Dean of the Graduate School

EXAMINING COMMITTEE:


William Moe

Date of Examination:

August 21, 2000